A coupled propulsion and thermal management system for hybrid electric aircraft design

A case study

R. Larkens

Technische Universiteit Delft

TU Delft Delft University of Technology

Challenge the future

A COUPLED PROPULSION AND THERMAL MANAGEMENT SYSTEM FOR HYBRID ELECTRIC AIRCRAFT DESIGN

A CASE STUDY

by

R. Larkens

in partial fulfillment of the requirements for the degree of

Master of Science

in Aerospace Engineering

at the Delft University of Technology,

to be defended publicly on Wednesday October 14, 2020 at 14:30 PM.

Supervisor:	Dr.ir. R. Vos,	TU Delft
Thesis committee:	Prof.dr.ing. G. Eitelberg,	TU Delft
	Ir. B.T.C. Zandbergen,	TU Delft

Cover image of the ATR72-600 is taken from https://www.aeronef.net/.
An electronic version of this thesis is available at http://repository.tudelft.nl/.

TU Delft Delft University of Technology

ACKNOWLEDGEMENTS

This thesis is the final work of my master Flight Performance and Propulsion at the TU Delft. After a mentally tough period, driven by unexpected personal and family issues, I am really happy and proud to conclude this period with my graduation.

First of all I would like to thank the TU Delft for giving me the opportunity to develop myself as a critical thinker over the years. More specifically for my thesis period, I would like to thank my supervisor Roelof Vos for his support, optimistic thinking, and trust during the process. I appreciate his willingness to enhance collaboration with the industry to share knowledge. This resulted in an interesting field trip to Fokker Elmo, guided by Kees Nuyten and in the visit to the Pacedays conference with a visit to the Pace building in Berlin. These opportunities highly improved my awareness of the challenges involved in the design of future hybrid electric aircraft.

I also would like to express my thanks to the Pace support team, especially to Barbara Bilo, Carlos Castro, and Mathias Emeneth for helping me out during the difficult learning process of the software. The many coffee breaks with Mihai Popescu also contributed to an accelerated understanding of the software along with some good laughs. Another thanks goes to Federica Ascione for the enjoyable discussions and good suggestions on the topic of cooling components. I would also like to thank Jacopo Zamboni for helping me to set a focus point during the initial phase of my thesis.

I would like to thank my family (Harm Jan Larkens, Florine Delie Kumanajare, and Gustav Larkens) for their unlimited support, especially in the last few months. The many phone calls due to limited visits helped me greatly to clarify and prioritise the most important things in life. My friends and housemates were also of vital support. They helped me to gain a more balanced body-mind connection by doing sports together, meditation sessions, and by just talking. They cheered me up when I was down, which is heartening to feel.

The person I would like to thank the most is my girlfriend Bernice den Haan. She gave me her confidence and trust to share my mental struggles on a daily basis. Without the many walks together and her talent for truly listening, I would not have been the person I am now.

R. Larkens
Delft, October 14, 2020

SUMMARY

Air transport is facing an important challenge when it comes to the reduction of its environmental footprint. Hybrid electric aircraft offer a potential solution to reduce in-flight emissions. The essence of hybrid electric aircraft is to combine multiple energy sources and energy conversion systems, in order to improve the overall energy efficiency and synergies, which could result in reduced emissions. Conventional design methods for aircraft are based on a single energy source and gas turbines, at which power production and propulsion are combined. However, hybrid electric aircraft allow for multiple energy sources and a decoupling of the propulsive device from the power producing device. These two fundamental differences open a new design space for future aircraft. As conventional design methods are not able to cope with the extended design space of hybrid electric aircraft, the necessity arises for novel conceptual design methods. In the context of hybrid electric aircraft, the energy sources are considered to be a combination of electrochemical batteries and conventional jet fuel in this thesis.

One of the effects of increased electrification is the generation of heat, due to inefficiencies. As hybrid electric aircraft further increase the electric power demand, even more heat will be generated. It is expected that the emitted heat will affect the weight, drag, and performance of hybrid electric aircraft, due to additional systems to control and dissipate excessive heat. As high-power systems require cooling to prevent performance degradation and battery thermal runaways, an adequate thermal management system is needed to control the thermal behaviour of hybrid electric powertrain components. For this reason, a coupled design approach between the hybrid electric powertrain and the thermal management system should be applied. Moreover, the sizing of thermal management system components is based on the thermal behaviour of these powertrain components. Therefore, modelling of the thermal effects is needed to acquire improved insights in the performance characteristics of hybrid electric aircraft during the conceptual design phase.

The objective of this thesis is to identify the impact of including a thermal management system on the power, weight, and volume usage for a parallel-hybrid electric ATR72-600 regional aircraft reference design case, that excluded the sizing of a cooling system.

A sizing methodology was developed for this case study. The sizing includes only the electric part of the powertrain with a coupled thermal management system. The latter is a combination of a closed-loop liquid cooling system and an air cycle system to pre-cool ambient air. The combination of all components that are sized are described by the term "system". Furthermore, the same battery is used to power both the powertrain and the thermal management system.

The validation of the defined system is performed at individual system component level, as no similar adequate reference data could be found in literature for this thermally-controlled electric propulsion system. The validation of the battery, electric motor, heat exchanger, and air cycle system is emphasised by comparing their performance behaviour to reference data.

The system is used to assess its impact with near-term and mid-term component technology levels, at which it is sized for hot day conditions. Flight missions characteristics are taken from the reference design case and used as input to capture the main sizing characteristics.

The results indicate a low feasibility potential if near-term technology levels are used. A higher feasibility is obtained with mid-term technology levels. The battery is identified to be the most critical component in terms of power, weight, and volume usage, which are driven by three interacting mechanisms. These are the electric propulsion power, the required cooling power, and the thermal capacity as a function of the battery weight. Concluding, the significant impact of a thermal management system can not be neglected in conceptual design studies for hybrid electric regional aircraft.

Contents

List of Figures

List of Tables

NOMENCLATURE

LIST OF LATIN SYMBOLS

A	=	Area	[m^2]
C	=	Heat capacity rate	[W/K]
C_D	=	Drag coefficient	[-]
c_p	=	Specific heat capacity	[J/kg/K]
D	=	Diameter	[m]
E	=	Energy	[J]
H	=	Degree of hybridisation	[-]
h	=	Heat transfer coefficient	[W/(m^2K)]
I	=	Current	[A]
J	=	Current density	[A/mm^2]
k	=	Correction factor	[-]
L	=	Length	[m]
M	=	Mach	[-]
m	=	Weight	[kg]
N	=	Number	[-]
P	=	Power	[W]
p	=	Pressure	[Pa]
Q	=	Thermal energy / torque / flow / capacity	[J] / [Nm] / [m^3/s] / [Ah]
R	=	Resistance	[Ω]
s	=	Entropy	[J/K]
T	=	Temperature	[K]
t	=	Time	[s]
U	=	Overall heat transfer coefficient	[W/m^2/K]
V	=	Voltage	[V]
v	=	Volume	[m^3]

LIST OF GREEK SYMBOLS

γ	=	Heat capacity ratio of air	[-]
Δ	=	Difference	[-]
ϵ	=	Specific energy	[Wh/kg]
ε	=	Effectiveness	[%]
η	=	Efficiency	[%]
ρ	=	Density	[kg/m^3]
$\hat{\rho}$	=	Energy density	[Wh/l]
ω	=	Rotational speed	[rad/s]
$\hat{v}$	=	Power density	[kW/m^3]

List of subscripts

bat	=	Battery
bus	=	Electric Bus
c	=	Critical
CB	=	Electric Cable
CP	=	Cold Plate
EM	=	Electric Motor
EMC	=	Electric Motor Controller
HP	=	Hydraulic Pump
GB	=	Gearbox
PC	=	Power Converter
PCO	=	Pneumatic Compressor
PF	=	Pneumatic Fan

LIST OF ACRONYMS

ACM	=	Air Cycle Machine
ACS	=	Air Cycle System
BLI	=	Boundary Layer Ingestion
BLDC	=	Brushless Direct Current
BPB	=	Battery Pack Burden
CSP	=	Combined Specific Power
DA	=	Design Assumption
DEP	=	Distributed Electric Propulsion
DOD	=	Depth Of Discharge
DOH	=	Degree Of Hybridisation
ECS	=	Environmental Control System
EMF	=	Electromotive Force
FTMS	=	Fuel Thermal Management System
HCR	=	Heat Capture Ratio
HEA	=	Hybrid Electric Aircraft
HEX	=	Heat Exchanger
HEP	=	Hybrid Electric Powertrain
HTS	=	High Temperature Superconducting
IR	=	Internal Resistance
ISA	=	International Standard Atmosphere
LR	=	Linear Resistance
LD	=	Linear Density
MEA	=	More Electric Aircraft
MTOW	=	Maximum take-off weight
NTU	=	Number of Transfer Units
OEW	=	Operating Empty Weight
PPU	=	Propulsive Power Unit
rpm	=	Rotations Per Minute
SP	=	Specific Power
SOC	=	State Of Charge
TMS	=	Thermal Management System
TTBW	=	Transonic Truss-Braced Wing
VCS	=	Vapour Cycle System
VDC	=	Voltage Direct Current
YEIS	=	Year Entry Into Service
ZFW	=	Zero Fuel Weight

1

INTRODUCTION

This chapter first presents the urge for new aircraft designs in Section 1.1. It explains the need for in-flight emission reduction of aircraft and the challenges related to the introduction of hybrid electric aircraft as a potential solution. Second, Section 1.2 provides the research objective and the used approach. Thereafter, the research scope and related research questions are stated in Section 1.3 and Section 1.4 respectively. Lastly, the outline of this report is briefly discussed in Section 1.5.

1.1. PROBLEM DEFINITION

On average, global air traffic is predicted to grow annually at a rate between 4 % - 5 %, resulting in a doubling approximately every 15 years [1, 2]. Around 2 % of the current global CO_2 emissions due to human activity originate from aviation [3]. Other aircraft operational emissions related to climate change include: nitrogen oxides (NO_x), sulphur oxides (SO_x), water vapor (H_2O), and contrails [4].

The European Commission (EC) and Advisory Council for Aviation Research and Innovation in Europe (ACARE) have set ambitious goals to reduce air traffic emissions for the year 2050. Flightpath 2050, established by the EC, is Europe's vision on future air transport. The objectives are: 75 % reduction in CO_2 emissions per passenger kilometre, 90 % NO_x emission reduction, and 65 % less perceived noise of flying aircraft relative to new aircraft from the year 2000 [1]. A Strategic Research and Innovation Agenda (SRIA) has been established by ACARE as a response to Flightpath 2050 [5]. SRIA is a stepwise approach to reach the emission goals set by the EC. Examples of similar objectives are set by the National Aeronautics and Space Administration (NASA) and the International Civil Aviation Organization (ICAO). These objectives are documented in the Environmentally Responsible Aviation (ERA) project and the Carbon Offsetting and Reduction Scheme for International Aviation (CORSIA) respectively [3, 6]. The recognised urge to realise major reductions in future air traffic emissions calls for innovative new aircraft and propulsion designs.

Hybrid Electric Aircraft (HEA) offer a potential solution to reduce in-flight emissions [7]. The essence of HEA is to combine multiple energy sources and energy conversion systems. This allows to improve the overall energy efficiency and system synergies, which could result in reduced in-flight emissions. However, higher degrees of electrification imply higher electric losses which generate heat. Therefore, adequate system heat control becomes essential to keep safe and optimal operating conditions [8, 9]. It has already been shown that excessive heat rejection capabilities, are critical for the flight performance of future high-power electric aircraft, nor can the significant increase in system weight and drag be underestimated [8, 10, 11].

The current feasibility boundary to apply hybridisation is identified to be for the regional aircraft segment [12–14]. First, this is because the typical flight lengths are relatively shorter compared to medium-haul flights, suppressing the additional energy storage weight and volume. Second, a market growth for regional aircraft is predicted while operational costs could be reduced if hybrid electric technologies are used [9, 15, 16]. Third, regional aircraft account for 14 % of the global aviation CO_2 emissions [15]. This further puts the focus on regional aircraft as an opportunity to significantly reduce in-flight emissions. For these reasons, several hybrid electric aircraft studies have been conducted based on a typical regional aircraft [12, 13, 15–19].

The type of Hybrid Electric Powertrain (HEP) architecture distinguishes different types of HEA. The most common HEPs are the series and the parallel architectures. It has been shown that a series architecture has a larger weight than a parallel architecture [13, 20]. Furthermore, the parallel HEP architecture is likely to become feasible first in future regional HEA, as it less sensitive to electric component developments and features a lower integrated design complexity to allow for retrofitting of conventional aircraft [19, 20].

1.2. RESEARCH OBJECTIVE AND APPROACH

The objective of this study is to identify the impact of including a Thermal Management System (TMS) on the power, weight, and volume usage for a parallel-hybrid electric regional aircraft, in order to facilitate conceptual design space exploration studies for future HEA. Even though the design of HEPs already increases the conceptual design phase complexity, the impact of a TMS has to be taken into account as it influences the viability of future HEA. To satisfy the research objective, several steps are taken.

First, a literature study is conducted to review the current technology state of parallel-hybrid electric architecture components and projected future developments. Next to this, a TMS approach has been chosen that is able to dissipate high heat losses while being not too complex for a conceptual design study. In case a component has to be modelled with more detail, to predict essential component behaviour, an adequate parametric model is obtained. Furthermore, a system sizing methodology is developed, in order to assess the system impact while being able to identifying sizing characteristics.

Second, the HEP and the TMS components are connected and placed inside a simplified representation of a typical regional aircraft. This allows to see the volumetric impact of these components and identify the most critical ones.

Third, the individual components are individually validated to see if they perform in a predictable way, in accordance to reference data. As no comparable system could be found in literature with adequate reference data, only component validation is conducted. Once validated, two component technology level scenarios are imposed to see the impact on the power usage, weight and volume. Sizing characteristics and critical components are identified for a typical regional aircraft flight mission at different atmospheric conditions. Finally, conclusions and recommendations are drawn from the found results.

The chosen simulation environment is the software package PaceLab SysArc [1]. This software enables the conceptual design and analysis of aircraft system architectures including a volumetric 3D representation of components inside the aircraft. It feature, a large internal component library to build complex HEPs. Furthermore, the standard components can be tailored and new ones can be constructed as well. Components are connected by an automatic routing algorithm. The shortest routes along permissible pathways are computed and visualised in the 3D view of the aircraft. Moreover, custom defined flight missions can be imposed.

1.3. RESEARCH SCOPE

This research is a case study limited to a single type of reference aircraft, the regional turbo-prop ATR72-600. The parallel HEP architecture is used, at which the sizing process excludes the sizing of the gas turbine to simplify the analysis. This implies that a reference case study with a similar aircraft, HEP, and without the integration of a TMS has to be used. Therefore, the focus of this study is narrowed down to the sizing impact of the TMS on the electric part of the parallel HEP and the TMS itself. Suitable reference case study results have been found in the study by Zamboni [20]. These are taken as input in this case study to estimate the impact on power, weight, and volume if the reference parallel HEP case study is supplemented with a coupled TMS.

For the TMS, a closed-loop liquid cooling system in combination with an Air Cycle System (ACS) is modelled, to enable HEP operation even at high ambient temperatures. The TMS is designed to be driven by electric power from the battery pack. This prevents the use of bleed air and allows to capture sizing characteristics that will probably be encountered during the design of fully electric aircraft as well.

[1] Pacelab SysArc is a commercial preliminary aircraft design software package used for system architecture and energy management analyses. The standard version 7.1 is customised and used for this study.

The results are based on hypothetical near-term (around the year 2025) and mid-term (around the year 2030-2040) component technology level scenarios [21, 22]. A long-term component technology level projection comprises too high uncertainties and is therefore only qualitatively discussed.

1.4. RESEARCH QUESTIONS

Given the presented research objective and scope, the following related research questions are defined:

- What are the figures of merit in terms power, weight, and volume to account for a liquid cooled TMS with a coupled ACS for the two technology level scenarios?
- What is the required maximum cooling power and at which flight segment does it occur?
- What is the effect of different maximum battery pack temperatures at take-off on the attainable electric power usage from the battery pack?
- What is the effect of a higher battery cell specific heat capacity on the battery sizing?
- How is the battery pack power usage affected by different atmospheric temperature profiles?
- Which components are the most critical in terms of power usage, volume, and weight?
- What are potential practical installation issues on board the aircraft for a thermally-controlled electric propulsion system?
- What is the impact on the feasibility of a regional parallel HEP aircraft for a near-term and a mid-term technology level scenarios?

1.5. DOCUMENT OUTLINE

This document continues in Chapter 2, with background information on the topic of HEA characteristics with the focus on the parallel-hybrid electric powertrain in Section 2.1. A qualitative assessment and comparison of thermal management system cooling strategies is presented in Section 2.2. The potential of superconducting technology and related design challenges are discussed in Section 2.4. This chapter closes in Section 2.5, with a comparison of battery cell technologies that could potentially be used for future hybrid electric aircraft.

The used methodology is explained in Chapter 3, including a flowchart that describes the sizing process in Section 3.1. The validation of the individual system components is discussed in Chapter 4. The results are presented in Chapter 5. First, the sizing characteristics used are given in Section 5.1. Second, the trade study results are discussed in Section 5.2. The weight and volume impact are examined in Section 5.3, including a visual impression of a sized system inside the aircraft. Finally, the conclusions of this thesis and the recommendations for future research are given in Chapter 6.

2

BACKGROUND INFORMATION

This chapter begins in Section 2.1 with general characteristics of HEA, at which the parallel-hybrid electric aircraft is highlighted. A qualitative assessment of three different thermal management system cooling strategies is presented in Section 2.2. Electric power transmission characteristics are given Section 2.3. The opportunities and challenges of superconducting technology are discussed in Section 2.4. The last section compares different battery cell technologies in Section 2.5.

2.1. ADVANTAGES AND CHALLENGES OF HYBRID ELECTRIC AIRCRAFT

The implementation of HEPs in aircraft applications is expected to give several advantages and disadvantages, compared to conventional aircraft propulsive systems. The potential of reducing in-flight emissions to lower the environmental footprint is one of the main advantages [7]. Due to the implementation of a second energy source, dependency on fossil fuel will be less. It allows to scale-down turbomachinery, which will result in reduced atmospheric heat release by less combustion along with reduced noise. Moreover, the replacement of hydraulic and pneumatic systems by electrical systems offer: higher efficiencies, improved reaction time, and lower maintenance costs [7, 23]. It also paves the way for integration of High Temperature Superconducting (HTS) technology, for electric transmission cables, and electric machines. HTS machines can enable the mitigation of heat related electric power transmission losses, to further improve system efficiencies [24]. HEPs offer the possibility to decouple the propulsive device from the power producing device. This allows independent optimisation of the propulsive and the power producing device. It also enables more design flexibility with an extended design space. The possibility to rethink conventional aircraft design allows for enhanced aero-propulsive synergy, i.e. improved aircraft performance due to propulsion-airframe interaction effects. Distributed propulsion over the wing is one promising example. Furthermore, it allows for reduced wing area or increased effective bypass ratios, by distributing propulsive units over the airframe to enhance aircraft performance [25]. Positioning of propulsive units at critical airframe positions can reduce drag. Wing tip vortex drag can for example be reduced by adding propellers that rotate in the opposite swirl direction.

Advances in battery performance are of paramount importance, as it will determine future HEA feasibility. The current energy densities of batteries are not sufficient enough to enable large commercial HEA to fly. However, smaller general aviation aircraft are already able to fly all-electric as the impact of the battery weight is less pronounced compared to larger HEA. Technology advances are needed as larger aircraft are the main contributors to in-flight greenhouse emissions [26]. Another important factor is the development of electric machines, to improve overall system efficiencies. A possible way to further increase system efficiencies is offered by HTS technology. However, the added complexity of HTS technology integration, which requires a cooling system to reach super conducting temperatures, offers vast challenges and is not likely to become available within 20 to 30 years from now [7, 21]. Without HTS technology available on the short term, heat generation in conventional transmission cables and electric machines is a major concern. An implemented Thermal Management System (TMS) should therefore control the heat dissipation to ensure safety and reliability with the use of more electric systems on board [8].

2.1.1. DEGREE OF HYBRIDISATION

Several definitions are used to define the degree of hybridisation for powertrains. A common way is to use two Degree Of Hybridisation (DOH) parameters: H_P and H_E, established by Lorenz et al. [27] and clarified by Isikveren et al. [28]. The power hybridisation parameter H_P defines the ratio of the maximum installed electric motor power (P_{EM}, i.e., the supplied power from energy source corrected for energy conversion efficiency) over the total installed power (P_{total}), see Equation 2.1. The energy hybridisation parameter (H_E) defines the ratio of the total utilised electric battery energy (E_{bat}), over the total utilised energy E_{total} for all phases of aircraft operation, given in Equation 2.2.

$$H_P = \frac{P_{EM}}{P_{total}} \tag{2.1}$$

$$H_E = \frac{E_{bat}}{E_{total}} \tag{2.2}$$

The two hybridisation parameters (H_P and H_E) are able to categorise all powertrain architectures with batteries as the secondary energy source. A visual representation of the DOH space is presented in Figure 2.1.

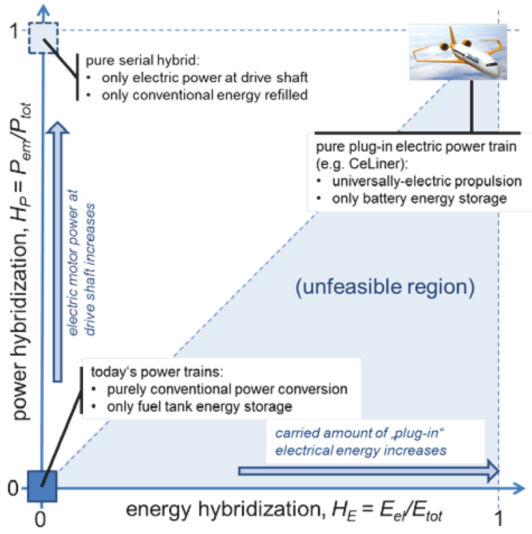

Figure 2.1: Classification of HEPs by using the H_P and H_E parameters [27].

As can be seen in Figure 2.1, the parameters H_P and H_E can have values from 0 up to and including 1. The origin, at which $H_P = 0$ and $H_E = 0$, represents a powertrain with zero installed electric motor power and zero stored electric battery energy. Conventional aircraft propulsive systems, purely based on internal combustion engines, are therefore allocated to the origin in Figure 2.1. The upper-left corner ($H_P = 1$ and $H_E = 0$) depicts powertrains that have only electric motor power installed while running purely on conventional fuel. The upper-right corner ($H_P = 1$ and $H_E = 1$) represents all-electric powertrains. Only electric energy stored in batteries is used to generate purely electric motor power. The lower-right corner ($H_P = 0$ and $H_E = 1$) illustrates powertrains with zero installed electric motor power but having only battery stored energy. As is indicated in Figure 2.1, all powertrain configurations inside this blue region are indicated unfeasible. It is illogical to carry more electric energy than can be used for electric motor power, not considering critical condition reserves.

The diagonal from ($H_P = 0$ and $H_E = 0$) to ($H_P = 1$ and $H_E = 1$) in Figure 2.1 represents the feasibility line. Powertrain configurations left to this feasibility line are thus feasible designs. Although a linear relation is sketched, it is indicated that the slope will vary based on the flight mission and the powertrain architecture [27]. Altitude effects are for example non-negligible. In the study by Isikveren et al. [29], an analytical relationship between H_P and H_E has been established.

2.1.2. HEP ARCHITECTURES

Three HEP categories can be distinguished: all-electric, hybrid electric, and turboelectric. In this report only the parallel HEP is discussed, which is based on batteries for the secondary energy storage. An overview of

the other HEPs can be found in [20, 26].

A common advantage of HEPs is the separation of energy and thrust generation which allows for high design flexibility. However, the major drawback when batteries are used is that the current battery specific energy [Wh/kg] only allows small general aviation and commuter aircraft to be commercially viable [1] [26, 30]. The specific energy of batteries required for larger aircraft should be much higher than nowadays is available, which is currently in the order of 200 [Wh/kg] to 250 [Wh/kg] for Lithium-ion (Li-ion) battery cells [31]. A specific energy of at least 500 Wh/kg to 750 Wh/kg has to become available to make HEA competitive with conventional aircraft designs [20, 26, 32]. When comparing Li-ion batteries with Jet-A fuel, a large deficit is present. The specific energy and energy density of Jet-A fuel is 11,950 Wh/kg and 9799 Wh/l respectively [33]. Assuming a specific energy of 200 Wh/kg for Li-ion batteries, roughly 60 times less energy can be stored for a given mass compared to Jet-A fuel [34]. It points out that huge battery improvements are needed.
In order to ensure that each HEP component is able to handle the demanded power, an upstream sizing approach should be applied. It takes the reversed power flow direction, i.e from the propulsion unit to the energy source. Efficiencies, near or at the propulsion unit are more valuable in this approach than the ones near the energy source [8]. This is because upstream components are sized based on the efficiencies of downstream components. If downstream components have higher efficiencies, then upstream components can be downsized as as well for the same efficiency. This approach is e.g. applied in the study by Zamboni et al. [17].

2.1.3. PARALLEL-HYBRID ARCHITECTURE

A parallel-hybrid architecture is defined by $0 < H_P < 1$ and $0 < H_E < 1$. The power to the propulsive unit is normally supplied simultaneously with electric motor power and gas turbine power. It is possible to change the power share over the power systems and even temporarily providing power from only one energy source [35]. In Figure 2.2a, it can be seen that the generated electric motor power and gas turbine power are combined at a mechanical node. The coupling of power systems can be done in two ways. The first option is to consider one common shaft at which the electric motor shaft is connected to the compressor shaft of the gas turbine. The second option is a connection of the electric motor shaft and the gas turbine (free power turbine) output shaft with a gear system, see Figure 2.2b. The transfer of electric power between components is often called the electric bus. The key components of a parallel hybrid architecture are: batteries, electric power transmission components, electric motors, a gas turbine with integrated mechanical node, and propulsive units.

In a parallel hybrid architecture, the two power systems can operate independently in certain conditions, allowing for a variable power share between the two power systems [35]. However, a critical minimum power share for the gas turbine is required to avoid detrimental off-design conditions, which requires additional transmissions and thus limiting the overall efficiency [36]. Next to this, clutches can be used for temporarily decoupling of one of the shaft power inputs, improving redundancy while increasing the architectural and operational complexity [36, 37]. Recharging of the batteries could be done by using mechanical power from the gas turbine output shaft or by wind milling using the propulsive device (e.g. fan or propeller). This is based on an assumed generative function of the electric motor and the possibility of de-coupled power systems [37].

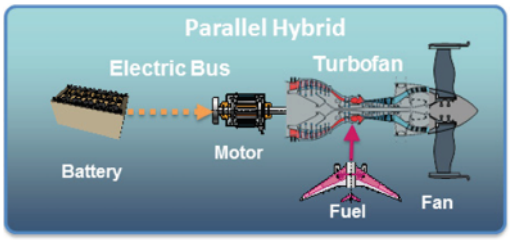

(a) Parallel hybrid powertrain architecture [26].

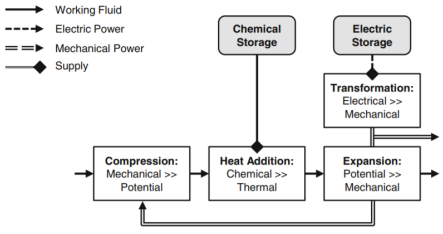

(b) Parallel hybrid power flows [35].

Figure 2.2: Schematics of parallel hybrid architectures.

[1] Rolls-Royce. Commuter Aircraft. URL: https://www.rolls-royce.com/innovation/propulsion/commuter-aircraft.aspx. Accessed on: 09/09/2020

PARALLEL-HYBRID CONCEPTS

With new design possibilities offered by the electrification of aircraft, several conceptual designs and studies have been published. Three parallel HEA designs are shown in Figure 2.3. Some important design characteristics are summarised in Table 2.1. It should be noted that the presented designs do not take into account the impact of a TMS.

(a) Boeing/NASA TTBW [2]. **(b)** Nasa Pegasus [16] **(c)** TU Delft study [20]

Figure 2.3: Impressions of parallel HEA designs and studies.

Table 2.1: Conceptual designs and studies of parallel HEA.

Name	Design YEIS	Seats	Design range [km]	MTOW [kg]	ϵ_{bat} [Wh/kg]	$P_{EM,\,max}$ [MW]	Characteristics
Boeing/NASA TTBW [2] [38, 39]	2035	154	1666	60,600	750	1.3	Transonic truss braced wing
NASA Pegasus [16, 40]	2030	48	741	24,059	500	1.34	DEP with tail cone BLI propulsion
TU Delft study [20]	2035	70	1712	25,614	750	1.33	Conventional two propeller configuration

BOEING/NASA TTBW

The TTBW of Boeing and NASA is based on a parallel HEP for the Year Entry Into Service (YEIS) 2035. It is the result of the so-called SUGAR program to innovate aircraft concepts with the aim to mitigate emissions and noise while improving aircraft performance. The upper mounted wing is supported by a truss on each side. The two trusses support the high aspect ratio wing, while generating lift. The wing can be folded upwards at both sides to comply with airport standards. The latest version of the TTBW design was published in 2019 [38, 39].

NASA PEGASUS

The NASA Pegasus is based on the regional ATR-42-500 aircraft and uses a parallel HEP. It is designed for the YEIS 2030. Compared to the baseline ATR-42-500, the Pegasus has five instead of two propellers. Four propellers are distributed over the wing to allow Distributed Electric Propulsion (DEP). The two outboard parallel-hybrid electric propulsors are located at the wing tips to reduce induced drag. The two inboard all-electric propulsors are only used when additional thrust is required (low and slow conditions). When not required e.g. during cruise, the two inboard are powered off and folded backwards to decrease windmilling effects. The fifth all-electric propulsor is located at the tail cone, to make use of Boundary Layer Ingestion (BLI) propulsion effects. The NASA Pegasus was published in 2017 [16].

TU DELFT STUDY

A parallel-hybrid case study conducted by the TU Delft is based on the ATR72-600 regional aircraft. It is designed with component technology levels to allow for a YEIS from 2035. A conventional aircraft shape is used to allow for a retrofitting of the reference aircraft, at the expense of aero-propulsive advantage possibilities. This study was conducted in 2018 [20].

[2] Boeing. Transonic Truss-Braced Wing. URL: http://www.boeing.com/features/2019/01/spreading-our-wings-01-19.page. Accessed on: 09/09/2020

2.2. QUALITATIVE ASSESSMENT OF THERMAL MANAGEMENT SYSTEMS

A TMS is basically responsible for three fundamental tasks: heat acquisition at the heat source, heat transportation to a dedicated heat sink, and heat rejection away from the aircraft [41]. For each of these tasks, several options can be considered. Therefore, proficient sizing tools should be used to assess the case specific TMS impact on the entire aircraft system [8].

It is expected that the increase in emitted heat of high-power electronics in HEP components, due to the system inefficiencies, could substantially impact the weight, drag and therefore the performance of future hybrid-electric and all-electric aircraft. Produced heat needs to be safely transferred away from the source, without large weight and volume penalties. The drag is affected due to the use of ram air Heat Exchangers (HEX), which is a common way to transfer excessive heat away from the aircraft. Partially re-using waste heat by other subsystems (e.g. for anti-icing, cabin heating, cooking in galleys or pre-heating of fuel) could improve the overall efficiency and implies a possibility to reduce bleed air off-takes. Therefore, a TMS should be integrated to regulate heat flows and the temperature of high-power electronics. A conclusion that can be drawn from this is that besides the design of the propulsive power management, a coupled thermal management is identified to be another essential system for the design of HEA and should therefore not be underestimated [8, 42–45].

The complexity, weight, volume, and energy demand of a thermally-controlled electric propulsion system all depend on the type of cooling applied, e.g. forced air cooling or liquid cooling. Nevertheless, in case the cooling system requires electric power to cool HEP components, additional power has to be extracted from an energy source. In the situation of a parallel HEP, this additional power originates either from the battery or from the fuel tank. If battery power is used, more heat losses will occur at the battery due to a higher discharge rate [46]. Therefore, more cooling power is required which raises again the battery discharge rate. If non-battery power is used, increased fuel energy conversion is required to acquire electric power. The latter increases the fuel consumption, which has a negative effect on the mitigation of in-flight emissions. These two examples qualitatively show the iterative sizing interaction for coupled propulsion and TMS components.

The impact of a TMS on the feasibility of HEA is assessed in the study conducted by Rheaume et al. [43]. They focused on the design of a liquid cooled TMS for a commercial parallel HEA, with a peak heat power load of 490 kW. This study estimated a fuel consumption increase of 3.4 % of the total mission fuel burn, due to the TMS weight, power, and drag. Only the take-off, climb, and cruise segments are taken into account. If hybridisation is applied at the descent and approach segments, the additional fuel consumption will increase even further. Furthermore, a projected fuel saving of 4 % to 7 % is calculated without the implementation of a TMS. By including the TMS, an effective fuel saving between 0.6 % to 3.6 % could be obtained. The coolants used are oil for higher temperatures and propylene-glycol mixture for lower temperatures.

From literature, three general active cooling strategies can be distinguished based on the cooling medium: air cooling, liquid cooling, and liquid-vapour cooling [44, 47–49]. These three strategies are further assessed and are compared in Section 2.2.4.

2.2.1. AIR COOLING

Air cooling is the most traditional way of cooling and is widely used in commercial applications [50]. When comparing passive air cooling (natural convection) and active air cooling (forced convection), the heat transfer coefficient (h) is normally much higher for active cooling [50, 51]. Passive air cooling is therefore less suitable for application with high heat losses. Newton's law of cooling is often used to estimate the heat transfer rate for convection cooling, by assuming a constant heat transfer coefficient, presented in Equation 2.3.

$$\frac{Q}{dt} = -h \cdot A \cdot (T_1 - T_2) \tag{2.3}$$

The heat transfer rate $\left(\frac{Q}{dt}\right)$ gives the amount of thermal energy per second [J/s] and depends on the heat transfer coefficient, the heat transfer area (A), the object's surface temperature T_1, and the free stream temperature T_2. In reality, the heat transfer coefficient is not constant as it increases with a thinner boundary-layer and with increase in turbulence . Therefore, numerical relations that are only valid for certain conditions are often used. These relations depend on non-dimensional numbers such as the Prandtl number, the Rayleigh

number, and the Reynolds number [52].
As the heat transfer rate is proportional to the temperature difference between surface temperature and the free stream air temperature, a lower air temperature results in a higher heat transfer rate. In case the free stream temperature is not low enough to meet a given heat transfer rate, pre-cooling of the air is required to still satisfy the heat transfer rate demand.

A common way of pre-cooling air is based on the reversed Brayton cycle. The working principle is presented based on an open ideal cycle in Figure 2.4. Three main components are identified from Figure 2.4a: a coupled compressor and turbine called the Air Cycle Machine (ACM) and a heat exchanger. In this report, these combined components are called the Air Cycle System. Furthermore, three fundamental steps have to be taken in order to cool down incoming warm air, see the Temperature Entropy (T-s) diagram in Figure 2.4b. First, the warm air is compressed to raise the pressure and temperature (1-2). Second, heat is extracted at the heat exchanger to lower the temperature at a constant pressure (2-3). Third, the temperature is further reduced as is expands trough the turbine (3-4). In this way, the air temperature can be reduced. It should be noted that non-isentropic and non-isobaric processes occur in real operating systems.

The Environmental Control System (ECS) in aircraft is often based on the reversed Brayton cycle principle and therefore commercially matured [53, 54]. Due to the use of air as the cooling medium, a low system weight, high operating reliability, and reduced maintenance result [55, 56]. Studies found that are based on the ACS principle for aircraft application use thermal heat loads up to 35 kW [55, 57–59]. Moreover, the reversed Brayton cycle allows to accomplish cryogenic temperatures, which consequently results in a more complex cooling system [55, 60]. Cryogenic superconducting technology is further discussed in Section 2.4.

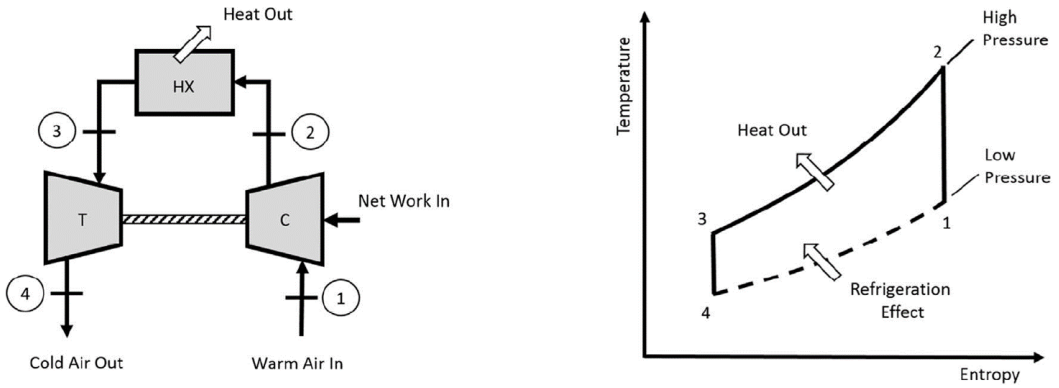

(a) Components of an ACS.

(b) T-s diagram of ideal ACS.

Figure 2.4: Working principle of an ideal ACS [49].

2.2.2. LIQUID COOLING

Liquid cooling is together with air cooling the most applied in electric vehicles [61]. It is based on a liquid coolant, e.g. water or a water/glycol mixture. The latter is often used as coolant to prevent freezing effects at the cost of reduced thermal performance and increased hydraulic resistance [62, 63]. To grasp the difference with air cooling, the specific heat coefficient [J/kg/K] of water is approximately four times larger than for air [64]. This means that liquid cooling allows for higher heat capture capabilities while being more compact [65]. Moreover, a lower power consumption is identified for a fixed heat load [61]. Next to this, heat transportation can be accomplished over a large distance [66]. On the contrary, the risk of coolant leakage and increased complexity lowers the reliability. The related increase in maintenance and costs should also be considered.

Two types of liquid cooling can be distinguished to capture heat at a heat source, namely direct and indirect cooling [50]. Direct liquid cooling is based on direct contact between the component surface and the coolant. Indirect liquid cooling is based on heat removal by a coolant flowing through tubes, for example by using a cold plate design. If the same coolant is used, the thermal resistance is likely to be larger for indirect liquid cooling due to additional material in between the component and the coolant. On the one hand, direct cooling allows improved cooling capabilities and therefore enhanced component performance [67]. On the other

hand, the more complex design, manufacturing, and maintenance raise the costs again.

Traditionally, fuel is used as a heat sink at components to remove heat, after which it is burned in the aircraft engine. This pre-heated fuel raises the efficiency of the engine while not using ram air to dissipate the heat [44, 68]. Furthermore, as it allows fuel to be multipurpose, the use of a dedicated supplemental coolant could be prevented [22]. The use of a Fuel Thermal Management System (FTMS) is applied in several studies for HEA and More Electric Aircraft (MEA) [22, 44, 68, 69].

The study conducted by Annapragada et al. [42] investigated a HEA battery heat acquisition system with a peak load of 126 kW. A closed-loop indirect liquid cooling approach is applied as it allows for improved heat capture performance, lower pressure drops, and an acceptable weight penalty compared to active air cooling.

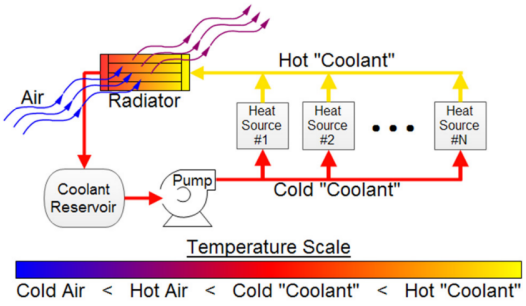

Figure 2.5: Schematic of the thermal management system in the ECO-150 with a liquid-to-air, ram air heat exchanger [70].

The design of the turboelectric ESAero/Wright ECO-150 in another example where a liquid cooled TMS is taken into account [70]. A schematic of the TMS used is shown in Figure 2.5. It is estimated that the electric components will produce a total of 1491 kW of heat power during the top of climb segment. The total engine power is sized on 12.6 MW based on the top of climb segment. Therefore, the maximum heat power loss equals 11.8 % of the total installed engine power. The overall weight of the TMS is approximated at 20 % of the weight of the electric components that it cools. The main TMS components considered in this study are: the coolant, ducts, coolant pump, reservoir and the radiator.

2.2.3. VAPOUR CYCLE SYSTEM COOLING

Compared to air cooling and liquid cooling that use a single phase coolant, Vapour Cycle System (VCS) cooling includes a two phase coolant. The VCS can be applied in aircraft for the use in the electrical ECS, to eliminate the use of bleed air off-takes [44]. Due to phase change processes, higher heat transfer rates are generally achievable compared to a ACS [71]. The power required for a VCS is typically five times lower compared to a comparable closed-loop ACS [72]. On the contrary, the weight of a VCS is normally higher due to a more complex design [49]. Moreover, the limited application of VCSs in aircraft is due to reliability and maintenance concerns [73].

In the turboelectric aircraft study by Kim et al. [44], a VCS is assessed in comparison with a FTMS for heat loads in the range from 2 MW to 10 MW. It was concluded the VCS requires significantly more power than the FTMS due due to high power usage of the compressor and the constant pressure changes in the system.

The VCS is based on the reversed Rankine cycle [49]. The fundamental components of a VCS are shown in Figure 2.6a and include the compressor, condenser, expansion valve and the evaporator. The working principle is visually explained in Figure 2.6b, using a T-s diagram for an ideal closed-loop reversed Rankine cycle [74]. First, compression is accomplished by the compressor to create high temperature vapour (1-2). Second, the vapour temperature is lowered, after which condensation takes place (heat output) through the condenser at a constant pressure (2-3). Third, a throttling process takes place with high friction effects and negligible heat transfer. It lowers the pressure and temperature at which the specific enthalpy is unchanged (3-4). Fourth, isobaric evaporation takes place through the evaporator as heat is absorbed (4-1). It should again be noted that losses occur in reality that alter the ideal processes as presented in Figure 2.6b.

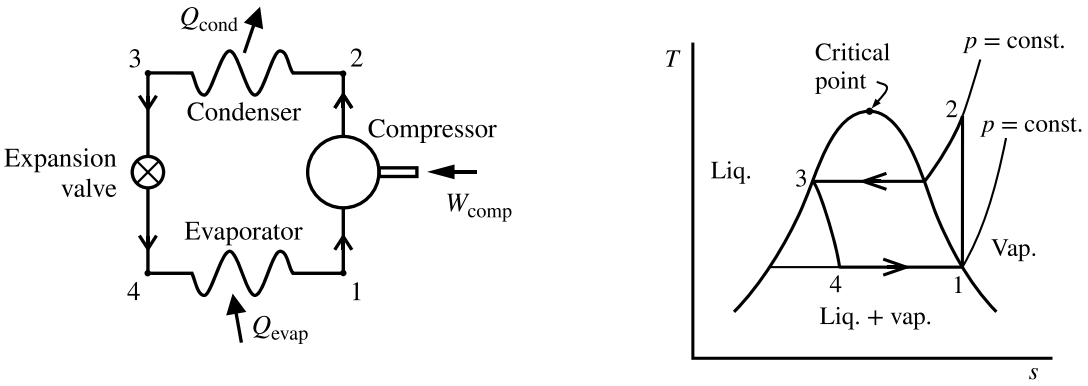

(a) Components of a VCS.

(b) T-s diagram of an ideal reversed Rankine cycle.

Figure 2.6: Working principle of an ideal reversed Rankine cycle [74].

2.2.4. COMPARISON OF COOLING STRATEGIES

It has been noticed that the choice for a certain cooling approach is rather complicated [8]. With the development from MEA to all-electric aircraft, a case specific cooling approach should be considered to comply with changing aircraft design constraints, in order to minimise its weight, volume, and power consumption. Nevertheless, the discussed cooling approach characteristics are summarised in Table 2.2. Active air cooling is found to be more suitable for lower thermal load, while liquid cooling and VCS allow for higher thermal loads. Heat transport over large distances can be accomplished by liquid cooling with the hazard of leakage. In terms of efficiency, VCS cooling should be considered. A combination of multiple cooling strategies offers more cooling flexibility while it increases design complexity [41]. Other important issues to take into account are the level of redundancy, implying the use of multiple cooling systems, and the technology readiness level.

Table 2.2: Qualitative comparison of cooling strategies.

Cooling strategy	Advantages	Disadvantages
Active air cooling	• Low weight • No liquid coolant leakage hazard • Less complex maintenance • Commercially matured • Low cost • High reliability	• Low heat load performance • Less compact • Low efficiency
Liquid cooling	• High heat load performance • Commercially matured • Long distance heat transport • Compact • Medium reliability	• Coolant leakage hazard • Increased maintenance complexity • More complex design • Higher costs • Additional coolant weight
VCS cooling	• High heat load performance • High efficiency	• Less commercially matured • Coolant leakage hazard • More complex control and maintenance • High costs • High weight

2.3. ELECTRIC ENERGY TRANSMISSION

Induced heat power loss of non-superconducting electric components is proportional to the resistance of the conductor and the electric current squared [3]. These losses are also called Ohmic losses or Joule heating [75].

Due to a voltage difference between the high potential conducting core of a power cable and the low potential air around it, electric current has the tendency to flow into the air. If this happens, partial electric discharge

[3] Britannica. Joule's law. URL: https://www.britannica.com/science/Joules-law. Accessed on: 10/09/2020

results [76]. Partial discharge only occurs above a certain critical voltage. The minimum voltage at which the insulation layer becomes electrically conductive is called the breakdown voltage. Important factors that lower the breakdown voltage are a thinner insulation layer, higher permittivity of the insulation layer, lower pressures, and higher temperatures [77, 78]. Paschen's law is used to describe the electric breakdown voltage. It dictates that below 327 V no electric discharge will take place independent of the air pressure [79].This resulted in a safety restriction of using at most 270 V in commercial aircraft electrical cables. In order to reduce Ohmic losses at high electric power demands, the need is present to go beyond the 270 V. Therefore, system voltages in the range of 700 V to 4000 V for future aircraft are investigated [4] [80, 81]. NASA predicted that insulation materials will improve in terms of thermal conductivity with a factor of 10, decrease in thickness by 50 %, and increase in power density with 25 % for the year 2030 relative to the year 2015 [80].

2.4. SUPERCONDUCTING TECHNOLOGY

Superconducting materials offer the possibility to transport electric power with near zero resistance (> 99 % efficiency), while having an increased current density [75]. This opens the door to significantly mitigate Ohmic losses. A notional comparison between a conventional conductor and a superconductor is given in Figure 2.7a. It shows the minimum resistance of a superconductor below its critical temperature T_c.

Superconductivity is based on the existence of electron pairs (Cooper pairs) in the lattice of the conductor. Compared to conventional conductors, where only single electrons are transporting electric charge, Cooper pairs are more stable than single electrons. This results in less resistance below the critical temperature, due to reduced electron-phonon interactions [5]. This phenomenon allows for reduction in cable weight and volume, which translates to higher power densities. Furthermore, the application of superconductors in e.g. electric motors and generators allows for higher magnetic fields than conventional designs, making higher efficiencies possible [75].

To sketch the impact of superconducting materials, a comparison in terms of Ohmic losses between a conventional copper conductor and a superconductor is presented in Figure 2.7b. The voltage is fixed at 270 V. Two effects can be noticed for the copper conductor: first the exponential growth of heat losses with increased power and second, the increased heat losses for a given power setting if the temperature is raised. Hardly any difference can be seen for the Yttrium Barium Copper Oxide (YBCO) HTS (High Temperature Superconducting) conductor. This example implies the necessity for high power applications to split electric power over multiple paths to reduce Ohmic losses, given conventional power transmission.

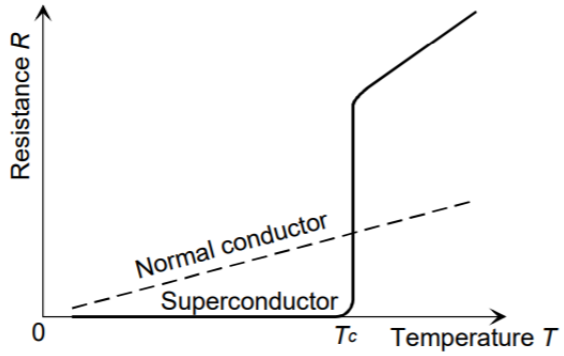

(a) Illustrative comparison between a conventional conductor and a superconductor, in terms of resistance as a function of temperature [82].

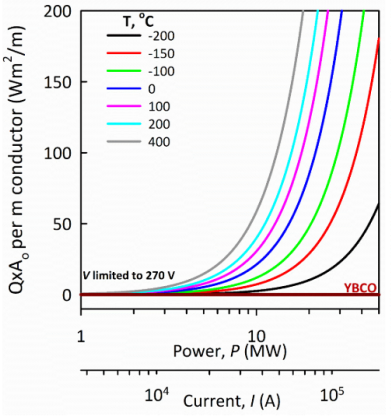

(b) Ohmic losses times cross-section for a copper conductor and the superconductor YBCO at 270 V [75].

Figure 2.7: Comparison between a conventional conductor and a superconductor.

[4] Airbus. E-fan X. URL: https://www.airbus.com/innovation/zero-emission/electric-flight/e-fan-x.html. Accessed on: 10/09/2020

[5] University of Bristol. Superconductivity. URL: http://www.chm.bris.ac.uk/webprojects2000/igrant/bcstheory.html#bcscurrent. Accessed on: 10/09/2020

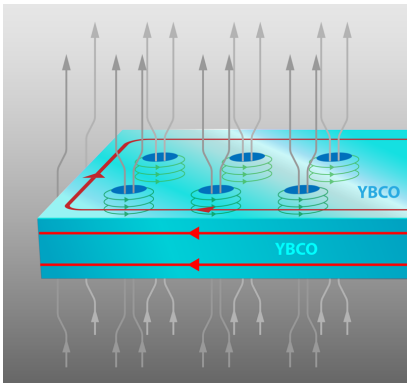

(a) Sketch of the mixed state, emphasising the penetration of magnetic vortices/flux lines with grey:magnetic field lines, red: superconducting currents, blue and green: non-superconducting vortex tunnels with superconducting currents flowing around [6].

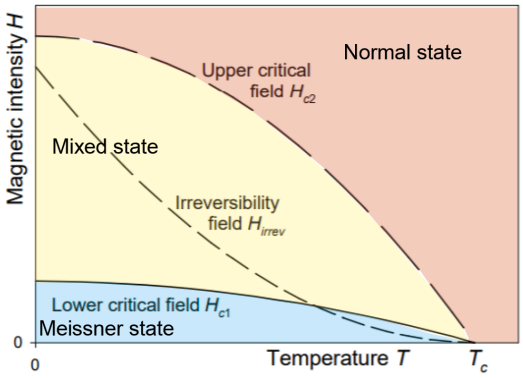

(b) Magnetic phase diagram for type-II superconducting materials [82].

Figure 2.8: Mixed state and a typical magnetic phase diagram for type-II superconductors.

Superconductors can be classified as either type-I or type-II. Type-I superconductors are characterised by an instantaneous reduction of resistance at the critical temperature, as sketched in Figure 2.7a. Moreover, they fully repel an external magnetic field, thus no penetration of magnetic field lines through the material occurs (Meissner state). Type-II superconductors on the other hand have a gradual transition to its fully superconducting state. A mixed state is present between the normal material state and the fully superconducting state. Superconducting properties become more pronounced when the temperature drops from T_c [82].

A typical magnetic phase diagram for a type-II superconductor is given in Figure 2.8b. The lower critical magnetic field strength boundary H_{c1} is the threshold below which type-I and type-II superconductors are only fully superconducting. Furthermore, magnetic field lines are able to penetrate through the material in the mixed state. When the external magnetic field strength is higher than H_{c1}, magnetic vortices will be formed [6], shown in Figure 2.8a [82]. These vortices are basically non-superconducting tunnels, for this reason it is called the mixed state. When the magnetic field strength boundary H_{c2} is exceeded, no Cooper pairs are present anymore, which results in a fully non-superconducting material behaviour [83]. The H_{irrev} boundary or irreversibility line separates the phase diagram into zero resistivity (below) and finite resistivity (above). Above the H_{irrev} boundary, resistivity is usually higher than the resistivity of a conventional conductor and therefore undesirable [82]. The mechanism responsible for the difference in resistivity is based on whether the magnetic vortices, also called flux lines or fluxoids, are stationary (pinned) or moving (depinned). Below the irreversibility line, magnetic flux lines are pinned, allowing transport supercurrent to flow along them while having zero electric resistance. On the contrary, the movement of depinned flux lines, caused by Lorentz forces as a result of the current to be transported and the external magnetic field, changes the magnetic field constantly. According to Faraday's Law, an induced electric field is formed, which is non-superconducting, causing finite resistivity. This dissipative motion of flux lines is called flux flow. It is the flux flow that obstructs a smooth supercurrent to flow and causes increased electric resistance.

Next to the critical temperature and the critical magnetic field strengths, the third constraint for superconductivity that can be defined is the critical current density J_c [A/mm^2]. It is defined as the maximum current per cross sectional area, at which Cooper pairs and thus the superconducting state can be sustained for superconducting materials [75]. The temperature, magnetic field strength, and mechanical properties including thermal shrinkage all influence the critical current density [82, 84]. In other words, type-II superconductors can only perform properly below the irreversibility line H_{irrev}, at temperatures lower than T_c, while having a transport current density lower than J_c. The challenge is to extend the operating boundaries further. With the ability to allow magnetic field lines to partially penetrate, type-II superconductors can withstand higher magnetic field strengths compared to type-I superconductors. This is one of the main reasons why the development of HTS materials is mainly concentrated around type-II superconductors, as they are more suitable for real-world applications [82].

[6] American Physical Society. Superconductor vortex states. URL: https://physics.aps.org/articles/v10/129. Accessed on: 10/09/2020

To obtain HTS temperatures, typically ranging from 27 °C to 77 °C, a cooling system is required [85]. Such a cryocooler can be designed as an open-loop or a closed-loop system. An open-loop system is less complex than a closed-loop system as no circulation of the coolant is required. This comes with the necessity of refilling the coolant storage tank on a regular basis. In case an aircraft uses high pressure liquid hydrogen as an energy source, it could also be used as a cooling medium to allow cryogenic cooling below 30 K [81]. This is a similar approach as for a conventional FTMS . A closed-loop system on the other hand should be used in case batteries are used. It allows for constant cooling, as long as it can be powered. The constant cooling ability after initial filling comes with higher system costs, weight, volume, design complexity, and increased maintenance.

Furthermore, it is important to know that more complex power cable designs are inevitable compared to conventional power cables [86, 87]. The start-up and shut-down time of cryocoolers should also not be underestimated as it can significantly impact aircraft ground operation time at airports [85, 88]. Moreover, safety, reliability, and airworthiness concerns are three other major issues [81]. Therefore, it is expected that superconducting technologies will not be matured for aircraft application within the next 20 to 30 years [21]. Nevertheless, aircraft cryocoolers are being explored, which are mainly based on the revere Brayton cycle [89–91].

2.5. BATTERY CHARACTERISTICS

A rechargeable battery, also called a secondary battery, converts chemical energy into electrical energy and vice versa. A primary battery can only be discharged once. Batteries used for the application in electric vehicles can be decomposed into several packaging levels, presented in Figure 2.9. With a top-down approach, the most integrated level is the battery system, which includes a control and a thermal management system to enhance performance. A battery system consists of multiple battery packs, connected in series and/or in parallel to get the desired electric output. The same holds for the battery modules, which are the building blocks for the battery pack. Modules consist of cells which again consist of one or multiple mono-cells [92]. The level of packaging of batteries should therefore be specified in order to provide a clear description of the related performance parameters. It indicates how much material, i.e. weight is included into the performance parameters.

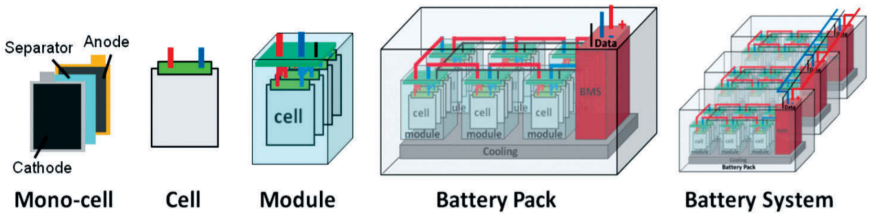

Figure 2.9: Packaging levels for electric vehicle battery systems [92].

Terminology is used to describe, classify, and compare different battery types. Common performance parameters used for rechargeable batteries are the following [50, 93, 94]:

- **Specific energy** [Wh/kg]: describes the endurance of a battery by the stored electrical energy per unit mass. It can be influenced by e.g. the temperature, discharge rate, and specific power. Specific energy is also known as the gravimetric energy density.
- **Energy density** [Wh/m3] or [Wh/l]: gives the stored electrical energy per unit volume of a battery. It gives insight in how much volume is required for a given energy need. It is also called volumetric energy density.
- **Specific power** [W/kg]: is the power that can be extracted from a battery (or inserted) per unit mass. When high power is required, batteries with a higher specific power are favourable.
- **Charge capacity** [Ah]: of a battery is the load current it can deliver over time. In the field of battery technology, ampère hour or amp hour [Ah] are mostly used as it is a more practical description instead of the official SI unit Coulomb to describe charge (1 Coulomb is equal to 1 ampere-second [As]). It is also

referred to as capacity or charge. For example, 20 Ah or $C = 20$ A describe that 20 A can be discharged for 1 hour. It also implies that 10 A can be discharged for 2 hours or 40 A for half an hour. In reality this relation is mostly not linear due to unfavourable side reactions. In general, if the discharge rate is higher than the given nominal discharge rate, a shorter run-time can be expected compared to the linearly scaled nominal run-time. It results in a lower charge capacity. If the discharge rate is lower than nominal discharge rate, a longer run-time can be expected. Therefore, an increased charge capacity results.

- **Stored energy** [Wh]: is the energy stored in the battery given in Wh instead of the Joules (SI Unit) due to practical battery application reasons. It is the product of battery voltage times the charge capacity, and therefore influenced by unfavourable side reactions during fast discharging.
- **Nominal cell voltage** [V]: is the assigned rated voltage of a cell by the manufacturer.
- **State of Charge** [%]: is the ratio between the remaining charge capacity and the nominal charge capacity. It gives insights in how much time the battery can still last at a given point in time for a given discharge rate. State of Charge is abbreviated as SOC. A SOC of 100 % means fully charged, while a SOC of 0 % means fully discharged. A lower SOC limit exists, below which the cells in the battery can be permanently damaged. This lower SOC limit is generally around 20 % - 30 % for Lithium-ion (Li-ion) batteries, determined with the nominal discharge current. The corresponding cell voltage at which a battery cell is considered fully discharged, is called the cut-off voltage. It can be described as a fixed fraction of the full cell voltage [81]. A voltage below the cut-off voltage is therefore not allowed.
- **Depth of Discharge** [%]: is abbreviated as DOD and is the rate of discharged capacity relative to the nominal charge capacity given by:

$$\text{DOD} = 100\,\% - \text{SOC} \tag{2.4}$$

2.5.1. THEORETICAL ELECTROCHEMICAL ENERGY POTENTIAL

The theoretical stored electrochemical energy within a battery cell is dictated by: the number of transferred electrons during reaction that is based on moles of reactant (n), the Faraday constant (F) which is the magnitude of electric charge per mole of electrons, and the cell voltage potential (E^0_{cell}) [7] [95]. Under standard conditions, the Gibbs free energy of the cell reaction is given in Equation (2.5) and it is also called the Nernst equation. The cell voltage potential is given in Equation (2.6) [96].

$$\text{Theoretical cell energy} = -n \cdot F \cdot E^0_{\text{cell}} \tag{2.5}$$

$$E^0_{\text{cell}} = E^0_{\text{cathode}} - E^0_{\text{anode}} \tag{2.6}$$

When the cell energy is divided by the sum of the mole mass or mole volume of the two reactants, the specific energy and specific density can be calculated respectively. The theoretical specific capacity per unit mass in [Ah/kg] (i.e. specific charge capacity) is given in Equation (2.7), with M as the mole weight of the electrode materials [95].

$$\text{Specific capacity} = \frac{n \cdot F}{3.6M} \tag{2.7}$$

In case $n > 1$, the reaction is called a multi-electron redox reaction due to the transportation of multiple electrons per atom. For example, when Zinc is oxidised, then $n = 2$.

$$\text{Zn} \longrightarrow \text{Zn}^{2+} + 2\,\text{e}^- \tag{2.8}$$

Therefore, the specific energy and energy density can be improved in several ways. First, by the use of electrode materials with higher specific charge capacities. Second, by implementation of cathode materials with higher redox voltage potential. Third, by making use of anode materials with low redox voltage potential. Fourth, by using active materials to transfer more electrons per molecule [95].

The four most promising battery technologies for aircraft applications are discussed from Section 2.5.2.

[7] LibreTexts. Electrochemical Cells and Thermodynamics.
URL: https://chem.libretexts.org/Bookshelves/Analytical_Chemistry/Supplemental_Modules_(Analytical_Chemistry)/Electrochemistry/Electrochemical_Cells_and_Thermodynamics.
Accessed on: 10/09/2020

2.5.2. LITHIUM-ION BATTERY

Most rechargeable battery cells basically consists of a negative electrode (anode), a positive electrode (cathode), electrolyte (transport medium), a separator, current collectors, and a cell case. The most influential parts are the electrodes, as they determine the energy density and the capacity of the cell [50]. Li-ion electrolytes are based on non-aqueous solutions of lithium containing salts, dissolved in an organic liquid solvent mixture. An organic solvent is a type of Volatile Organic Compound (VOC) that will vaporise at room temperature and is capable of dissolving non-aqueous soluble materials. Current collectors are mostly made of copper for the anode and aluminium for the cathode. The cell case is a sealed container, generally made of steel or aluminium to get satisfactory mechanical and thermodynamic properties. Typical Li-ion cells are mostly shaped in either a prismatic or a cylindrical shape [8]. The working principle of a typical Li-ion cell is schematically presented in Figure 2.10.

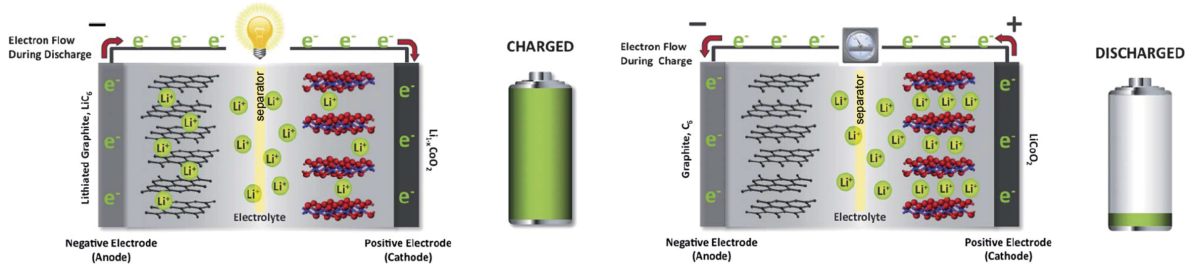

(a) Discharging **(b)** Charging

Figure 2.10: Working principle of a typical $Li_xC_6/Li_{1-x}CoO_2$ Li-ion cell [97].

The charge and discharge processes are based on the transportation of lithium ions between the electrodes, facilitated by the electrolyte. When the cell is charged, external electric energy is used to extract positively charged intercalated lithium ions from the cathode and forced to travel trough the electrolyte and the separator to be stored at the anode, see schematic in Figure 2.10b. Both cathode and anode can intercalate (absorb) lithium ions inside the electrode structure, together with an equal amount of corresponding electrons. The electrolyte is used as transport medium for the lithium ions and the separator functions as a short circuit protection. The separator is a permeable thin layer, allowing lithium ions to pass through. While positively charged lithium ions are moving from the cathode to the anode, the same amount of negatively charged electrons is simultaneously released at the cathode. The electrons are collected and transported to the anode, to keep electric equilibrium. The connected voltage source between the cathode and the anode increases the electric potential of the electrons which are finally reassembled at the anode to maintain electric charge equilibrium. The chemical redox reactions are given in Equations 2.9 to 2.11, by using a lithium cobalt oxide ($LiCoO_2$) cathode and graphite (C_6) anode Li-ion cell.

$$\text{Cathode reactions:} \quad LiCoO_2 \underset{\text{discharge}}{\overset{\text{charge}}{\rightleftharpoons}} Li_{1-x}CoO_2 + xLi^+ + xe^- \tag{2.9}$$

$$\text{Anode reactions:} \quad C_6 + xLi^+ + xe^- \underset{\text{discharge}}{\overset{\text{charge}}{\rightleftharpoons}} Li_xC_6 \tag{2.10}$$

$$\text{Total cell reactions:} \quad C_6 + LiCoO_2 \underset{\text{discharge}}{\overset{\text{charge}}{\rightleftharpoons}} Li_{1-x}CoO_2 + Li_xC_6 \tag{2.11}$$

From Equation (2.9), it can be seen that during cell charge, oxidation takes place for $LiCoO_2$ at the cathode. An equal charge left and right of the reaction arrow is required for equilibrium. At the anode, reduction takes place for C_6 during charge, shown in Equation (2.10). By combining the two half reactions, the total cell reaction can be obtained, given in Equation (2.11). During discharge, the opposite reactions take place, shown in the schematic of Figure 2.10a.

The theoretical specific energy does not take packaging at cell and battery level into account. Therefore, the specific energy at cell level is always lower than theoretically calculated. This will reduce the energy per

[8] Panasonic. Lithium-ion Batteries. URL: https://industrial.panasonic.com/ww/products/batteries/secondary-batteries/lithium-ion. Accessed on: 12/09/2020

unit mass. The installation effects of cells eventually determine the battery specific energy. This includes additional material and mass due to the connection of cells in battery modules, implementation of a TMS, and a frame structure. Taking the $Li_xC_6/Li_{1-x}CoO_2$ Li-ion battery, the theoretical specific energy is calculated on 584 Wh/kg, for x=1 [97]. Commercially available Li-ion batteries have a specific energy in the order of 200 Wh/kg, depending on the cell and battery module integration [50]. It is estimated that the maximum specific energy of Li-ion battery packs will flatten close to 300 Wh/kg [97].

ENVIRONMENTAL IMPACT

Other key issues in the quest towards improved secondary batteries are the use of critical elements and the environmental impact of the mining process. Cobalt already has a critical status, which is also predicted for lithium in the future. To improve sustainability, several action points should be considered [31]. First, a reduction of the environmental footprint of the mining process. Second, an effective battery collection and recycling scheme. Third, a dependency minimisation on critical raw materials. Fourth, a wider implementation, market growth, and lower battery costs.

THERMAL ISSUES

Thermodynamic effects become even more critical as more reactive electrode materials are used to improve battery performance. Related thermal issues are discussed based on Li-ion batteries, as the characteristics are to a certain extent representative for other, more advanced battery technologies.

The temperature plays an important role, as it can impact the battery performance in several ways [50]. For Li-ion batteries, the acceptable operating temperature range is between −20 °C to 60 °C, while battery performance is improved in the temperature range between 15 °C to 40 °C, which depends on the cell chemistry [50, 98]. Battery charge capacity loss will occur when the operating temperature is outside the desired range. To further enhance battery performance, the temperature difference between cells and battery modules should not be greater than 5 °C [46].

For a given voltage, it has been found that the charge capacity drops for an increase in the cycle numbers (charge-discharge process). In case higher temperatures are imposed for a given number of cycle, the charge capacity drops as well due to internal losses [99]. Furthermore, when high temperatures are reached in a battery cell, e.g. by short circuiting or a too long overcharge, a thermal runaway can be induced [50]. During a thermal runaway, exothermic chain reactions are initiated, which increase internal temperature and pressure. This results in a high risk of a catastrophic explosion. It was found that prediction methods to manage a thermal runaway, based solely on the surface temperature are likely to have a large error. The surface temperature is not fully representative as the core temperature can be much higher due internal reactions and low thermal conductivity of the casing [100]. To ensure a save use without core temperature modelling, a lower applied load is required to account for the internal temperature uncertainty, reducing the cell performance. Further measures that can be taken in order to reduce the risk of a thermal runaway are for example: an adequate battery TMS, pressure release valves, thermal fuses, shutdown separators, and usage of thermal retardant materials [101].

Heat is generated during the charge/discharge process, as a result of internal impedance and electrochemical reactions. In case of fast charging and discharging, even more heat is generated. Within a cell, non-uniform temperature distribution is present as most heat is generated at the electrodes where the electrochemical reactions take place [50, 102]. This non-uniform temperature distribution can result in reduced cell and battery performance. Furthermore, a higher heat dissipation rate at the outer side of a battery pack, due to natural or forced heat dissipation (cooling system), enhances the temperature non-uniformity as well. Taking into account a safe operating temperature range for each cell, the battery performance will be adapted to the cell with the lowest performance [50]. In order to improve battery performance, temperature non-uniformity should be mitigated for example by: electrode modification to improve cell temperature uniformity, using electrolyte as a coolant, or by implementing a battery TMS to reduce and even temperature differences [50].

While Li-ion battery performance degrades with high temperatures, similar phenomena are present at low temperatures [103]. For this reason, battery heating should also be possible when considering a battery TMS. Different battery heat capturing methods are discussed in [50].

2.5.3. LITHIUM-SULPHUR BATTERY

Lithium-Sulphur (Li-S) battery technology is promising due to its low cost, high charge capacity, and sulphur abundance [104]. Conventional Li-S cells are based on a sulphur cathode, a lithium anode, and an organic electrolyte, see Figure 2.11b. The theoretical specific energy and energy density of a Li-S cell is 2500 Wh/kg and 2800 Wh/l respectively [105]. When packaging is taken into account, the practical battery pack energy density is calculated in the order of 500 Wh/kg [106, 107]. Compared to advanced Li-ion batteries with a battery specific energy of 250 Wh/kg, Li-S has the potential to increase the specific energy with a factor of two. In Figure 2.11, Li-S and other battery alternatives are compared with gasoline in terms of their theoretical and practical battery gravimetric energy densities. The dashed black line in Figure 2.11a represents a 100 % use of the theoretical energy density value, while the dashed grey line depicts a 20 % value of the black line. The practical energy density of gasoline is presumably based on the average tank-to-wheel efficiency of cars [108]. As no commercial Li-oxygen batteries are available at the moment, practical values are projected estimations. Li-S prototype batteries are already produced on a very small scale and used in test vehicles to be further developed. Energy densities of these cells vary between 400-500 Wh/kg and 400-1000 Wh/l[9], [10]. The optimal operating temperature of the OXIS cell[9] is between 0 °C and 30 °C.

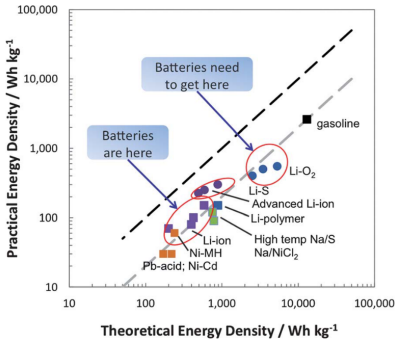

(a) Practical specific energy (gravimetric energy density) plotted as a function of the theoretical specific energy of secondary batteries [97].

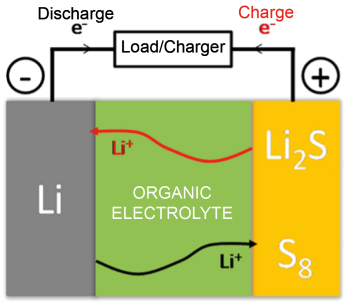

(b) Working principle of a Li-S battery [109].

Figure 2.11: Comparison of battery energy densities with gasoline and working principle of a typical Li-S cell.

The charge and discharge processes are complex, due to multiple side reactions that simultaneously occur. During discharge several reduction stages are present, influenced by the electrolyte composition [104]. The first stage is the reduction of sulphur (S_8) to the lithium polysulphide Li_2S_4. The created lithium polysulphides are then dissolved into the electrolyte. While the discharge continues, a further reduction of the lithium polysulphides takes place to lower orders namely: Li_2S_n ($2 < n < 4$) and Li_2S. The dissolution and diffusion of lithium polysulphides in the electrolyte negatively influence the electrochemical performance. Dissolved Li_2S_n particles are able to flow between the electrodes, through the separator (shuttle effect). Due to the shuttle effect, Li_2S_n particles are likely to cover the lithium anode surface with an inactive solid layer of Li_2S_2 and Li_2S [106]. The reverse process occurs during charging. This results in irreversibly reduced charge capacity, reduced Coulombic efficiency[11], and poor cycling performance due to reduced active material (electrochemical couples) and increased cell impedance [110]. Other issues are the volume change of sulphur close to 80 %, which reduces its electrical contact with the conductive substrate or the current collector and the forming of lithium dendrites during cycling [104, 106, 110]. The focus of current research is to tackle these issues. The redox reactions are given in Equations 2.12 to 2.14 [105].

$$\text{Cathode reaction:} \quad 8\,Li_2S \underset{\text{discharge}}{\overset{\text{charge}}{\rightleftharpoons}} S_8 + 16\,Li^+ + 16\,e^- \tag{2.12}$$

$$\text{Anode reaction:} \quad 16\,Li^+ + 16\,e^- \underset{\text{discharge}}{\overset{\text{charge}}{\rightleftharpoons}} 16\,Li \tag{2.13}$$

$$\text{Total reaction:} \quad 8\,Li_2S \underset{\text{discharge}}{\overset{\text{charge}}{\rightleftharpoons}} S_8 + 16\,Li \tag{2.14}$$

[9] OXIS Energy. Products. URL: https://oxisenergy.com/products/. Accessed on: 14/09/2020
[10] Sion Power. Products. URL: https://sionpower.com/products/. Accessed on: 14/09/2020
[11] Coulombic efficiency is the ratio between the extracted charge and the total provided charge over a full cycle.

2.5.4. LITHIUM-OXYGEN BATTERY

Li-oxygen ($Li-O_2$) battery technology is one of the most promising future battery technologies, due to its potentially high energy density, and cheap and abundant oxygen supply [111]. A $Li-O_2$ battery typically consists of a lithium anode, a porous carbon cathode, an electrolyte, a separator, and catalysts [112]. The type of electrolyte is used to further classify four different types of $Li-O_2$ batteries, namely: non-aqueous (also called aprotic), aqueous, hybrid, and solid state, shown in Figure 2.12. Amongst these four types, studies have been mainly focused on the non-aqueous $Li-O_2$ types. This is due to its higher theoretical specific energy compared to the aqueous type, while it is regarded as the simplest cell architecture amongst the rest [112–114]. Therefore, the non-aqueous $Li-O_2$ type is considered to be the most promising future battery technology [108]. The theoretical specific energy and specific density of the lithium metal/lithium-peroxide couple are calculated at 3458 Wh/kg and 3445 Wh/l respectively [113]. Corresponding redox reactions are given in Equations 2.15 to 2.17. The practical energy density at cell level is however estimated at 1700 Wh/kg and will be around 850 Wh/kg at battery system level [115]. Wu et al. [111] classified $Li-O_2$ based on pure oxygen batteries as conventional (closed cycle), while $Li-O_2$ batteries based on air are classified as advanced batteries (open cycle). The difference is based on how oxygen is fed into the system, in a pure form or contained within air.

During the discharge process of a $Li-O_2$ battery, lithium is oxidised at the anode, shown in Equation 2.16 and Figure 2.12. The Li^+ ions travel through the electrolyte to the cathode, while the electrons are diverted along an applied load. At the cathode side, the Li^+ ions react with the dissolved O_2 to form Li_2O_2, shown in Equation 2.15. During charging, the reactions are reversed. In Figure 2.12, it can be seen that catalysts are placed at the cathode. This is needed to speed-up the rather slow oxidation and reduction reactions at the cathode, improving battery performance. The need for catalysts increases the complexity of the battery [111].

$$\text{Cathode reaction:} \quad Li_2O_2 \underset{\text{discharge}}{\overset{\text{charge}}{\rightleftharpoons}} 2Li^+ + O_2 + 2e^- \tag{2.15}$$

$$\text{Anode reaction:} \quad 2Li^+ + 2e^- \underset{\text{discharge}}{\overset{\text{charge}}{\rightleftharpoons}} 2Li \tag{2.16}$$

$$\text{Total reaction:} \quad Li_2O_2 \underset{\text{discharge}}{\overset{\text{charge}}{\rightleftharpoons}} 2Li + O_2 \tag{2.17}$$

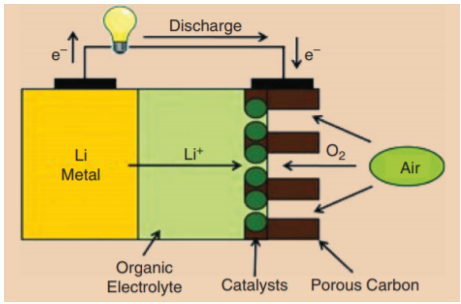

(a) $Li-O_2$ type: non-aqueous electrolytic.

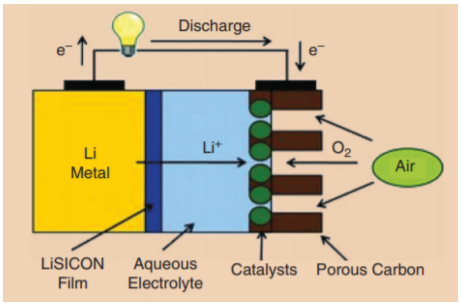

(b) $Li-O_2$ type: aqueous electrolytic.

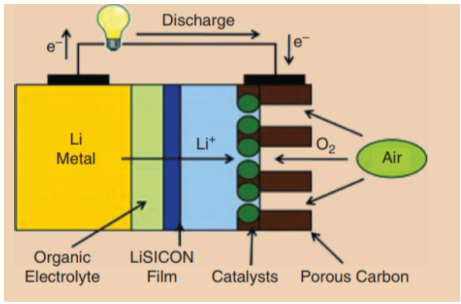

(c) $Li-O_2$ type: hybrid.

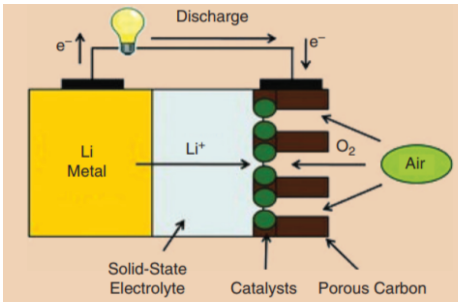

(d) $Li-O_2$ type: solid-state.

Figure 2.12: Four types of $Li-O_2$ batteries [116].

Many challenges have to be faced to improve the performance of Li−O_2 batteries. Rahman et al. [117] discussed the main issues to be solved. One of the most critical parts is the porous cathode in terms of the used materials, structures, and fabrication [108]. As the cathode is responsible for the highest cell voltage drop, most electrochemical energy is converted at the cathode. The large deficit between the theoretical and practical energy densities is due to the early termination of the discharge process. One of the reasons is the blockage of the porous cathode, causing the pores to be not fully filled with Li_2O_2. Another cathode related issue is the degradation of the cathode by environmental humidity. Furthermore, the need for a catalyst increases cell complexity, while the ones currently used are costly as gold and platinum particles are needed to enhance performance [117]. While a closed cycle can be used to supply oxygen in a controlled manner, the ultimate goal is to filter oxygen from the open air. The challenge is to avoid infiltration of moisture from the air, as it will also deteriorate the electrolyte and the lithium anode to cause a poor life cycle [118]. Moreover, novel electrolytes have to be found to counteract side reactions. With the use of a lithium metal anode, dendrite formation forms a main issue that can cause poor cycle life and the risk of short-circuiting. The use of a stable SEI film on the anode surface or a solid polymer electrolyte are solutions to counteract the dendrite formation while still conducting Li^+ ions. On top of this, both aqueous and non-aqueous Li−O_2 batteries experience a weight and volume change during cycling, making the design even more complex. This is mainly caused by the shrinkage of the lithium anode due to oxidation and by the solubility of Li_2O_2 [119]. Based on a Li−O_2 gravimetric and volumetric energy density prediction model, a weight increase close to 10 % and a volume decrease close to 20 % is calculated from a fully charged to a fully discharged cell [120].

Recent studies reported Li−O_2 batteries with specific energies and energy densities at cell level in the order of 1200 Wh/kg and 880 Wh/l respectively [121, 122]. In the study conducted by Park et al.[121], inadequate cycle lifetime performance was concluded. Only seven charge and discharge cycles could be conducted while maintaining 500 Wh/kg, after which the capacity severely dropped. Another promising recent study demonstrated a Li−O_2 battery at cell level, capable of performing 700 charge and discharge cycles without any visible degradation and side reactions. Li−O_2 batteries are not commercially available [123]. A market readiness from 2030 is expected for Li−O_2 batteries [124].

2.5.5. FLUORIDE-ION BATTERY

Fluoride-ion (F-ion) battery technology is another potential altnernative to increase battery performance. This novel battery technology allows, with certain material combinations, for a theoretical specific energy, and energy density in the order of 1500 Wh/kg and 5000 Wh/l respectively [96, 125, 126]. The working principle is schematically shown in Figure 2.13, based on a BiF_3/Mg electrochemical couple. The main parts are a cathode based on a metal fluoride, a metal anode, electrolyte, and a separator (not shown in Figure 2.13). During discharge, a multi-electron redox reaction takes place, at which two electrons are released at the anode. At the same time, the transport of fluoride-ions occurs trough the electrolyte. At the cathode, a neutral metal is formed with the electrons and the fluoride-ions [127]. The electrolyte is one of the most critical parts as it should support fast conduction of the fluoride-ions at satisfying conditions [126]. Until recently, only solid-state electrolytes were able to support high ion–conduction with operating temperatures of 150 °C and above [125]. These eleveted operating temperatures are not suitable for real world applications. However, a recent study by Davis et al. [125] reported a breakthrough in terms of an liquid electrolyte, to be used at room temperatures in combination with a core shell cathode material to improve charge and discharge cycles. In essence, fluoride-ion batteries are not more dangerous than other battery types as long as adequate safety measurements are taken. Next to this, fluoride containing materials, e.g. in the form of calcium fluoride, are globally abundant [127]. Car manufacturer Honda is already closely involved in the development of this battery technology[12].

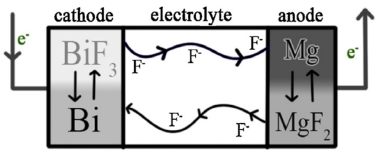

Figure 2.13: Working principle of a BiF_3 cathode, Mg anode fluoride ion cell [127].

[12] ECS. Honda'a Battery Breakthrough. URL: https://www.electrochem.org/redcat-blog/hondas-battery-breakthrough/. Accessed on: 15/09/2020

2.5.6. BATTERY TECHNOLOGY COMPARISON

A battery comparison is presented in Table 2.3 at pack level, based on the study conducted in 2012 by Gerssen-Gondelach et al. [107]. Several values have been updated. If only theoretical values are known, battery pack values are estimated based on 33 % of the theoretical values [128, 129]. If only state-of-the-art values at cell level are known, battery pack values are estimated with 93.5 % of the cell values [130]. This takes into account the additional weight for battery accessories.

Table 2.3: Comparison of future battery technology at battery pack level for beyond 2025, based on [107]

Battery type	Specific energy [Wh/kg]	Specific power [W/kg]	Energy density [Wh/l]	Cycling efficiency [%]	Cycle life [# Cycles]	OTR[13] range [°C]	DOD [%]	Lifetime [Years]	Costs [$/kWh]	Uncertainty
Li-ion [31, 97, 107] [131, 132]	250-300	400-600	~ 600	90-95	2000–3000	-20 to 60	70-90	7-15	190	low
Li-S [106, 128]	500-600	~ 400	~ 1000	70-90	500-1000	-20 to 60	90-100	5-10	250-500	medium
Li-air (open cycle) [119, 122, 129]	~ 1100[14]	~ 300	~ 850[14]	60-85	500-1000	25 to 100	70-90	5-10	300-700	high
F-ion [96, 125]	495[15]	-	1650[15]	-	-	≥150,20	-	-	-	very high

It is likely that Li-S batteries are going to improve Li-ion battery performance with a factor of two. Only Li-air batteries have the potential to further improve the specific energy with a factor of around 4, compared to current Li-ion batteries. The development of fluoride-ion batteries offers high energy densities while the specific energy is lacking so far and comes with even more uncertainty than Li-air batteries. A NASA projection of potential improvements at battery cell level, for 10 years and 25 years from now, shows similar battery developments [80].

[13] OTR: Operating Temperature Range
[14] 93.5% of cell value
[15] 33% of theoretical value

3

METHODOLOGY

This section presents the methodology used to size the coupled parallel HEP and liquid cooled TMS. First, an overview of the used sizing strategy is given in Section 3.1. Second, the sizing methods for the electric part of the propulsive powertrain are presented in more detail in Section 3.2. Third, the sizing methods for the TMS components are presented in Section 3.3.

3.1. SIZING METHOD APPROACH

The sizing method that is applied to size the coupled parallel HEP and liquid cooled TMS uses an upstream power-based sizing approach, i.e. the component sizing starts from the Propulsive Power Unit (PPU) and goes back to the battery pack. The flowchart that describes the sizing method is presented in Figure 3.1.

The sizing process starts with defining the top level inputs. These are fixed inputs for a given scenario and apply to the whole flight mission analysis. Once the top level inputs are set, the thermally-controlled electric propulsion system is sized in the system sizing loop, indicated by the dashed box shape in Figure 3.1.

The system sizing loop starts with imposing the required inputs for the first flight segment at which hybridisation is required. The parallel HEP hybridisation strategy of [20] is used to extract the total required propulsive electric power and is equally split over the two PPUs. For simplicity reasons, a single point performance condition is chosen that represents a single flight segment, as is defined in [20]. This point is chosen based on the average propulsive electric power. Therefore, the propulsive electric power is constant if hybridisation is required and zero if not. The related flight altitude and Mach number, for the single point performance condition, are then used to compute the corresponding atmospheric conditions based on the given atmospheric profile. Furthermore, heat power capture ratios have to be set for each component to be cooled, i.e. the cooling strategy. Once the required power for each PPU is imposed, the upstream power-based sizing propagation starts, given by the powertrain electric component module.

The coupling of the PPU to the HEP is represented in Figure 3.2 by a rotational load (engine coupling) in combination with a gearbox. The power required increases for each upstream component due to inefficiencies. The maximum powers required are the sizing powers and are used to estimate the weight and volume of these components.

The resulting electric power production by the battery pack, including its own inefficiency, is used as its sizing power. The resulting heat capacity of the battery pack is also taken into account, in order to establish a thermal balance between a controlled temperature change and an active heat power cooling during operation. This means that a higher battery pack sizing power can occur than strictly required, in order to acquire a higher heat capacity to comply with the thermal balance. The accumulated component heat production is collected by a liquid cooled TMS and rejected via a ram air heat exchanger (HEX), as shown in Figure 3.2.

As the TMS components take their electric power from the battery pack (no bleed air usage), the battery pack sizing power increases and causes more heat power loss, which increases the TMS component sizing powers

again. An iterative sizing loop arises when the component heat power losses are steadily increased up to the point to comply with the cooling strategy. This iterative flight segment sizing loop is indicated by I in Figure 3.1. This loop is converged when the whole thermally-controlled electric propulsion system has reached the imposed cooling strategy, while the required powers stay below the sizing powers.

If the first sizing loop is converged, a second check is performed to see if any of the four imposed sizing constraints are violated. These include the battery pack minimum SOC, the maximum allowable cooling power ratio (ratio of extracted electric power from the battery pack consumed by the TMS components), the maximum ram air inlet flow rate, and the minimum chain efficiency (see Equation (3.1)). If one of these constraints is violated, the electric power of the PPU is reduced, i.e. the hybridisation in that flight segment is reduced. The second flight segment loop is then initiated, indicated by II in Figure 3.1. The sizing of all components is re-assessed, which triggers again the first sizing loop.

Once the first and second sizing loops have been converged, the resulting sizing data is passed on to the successive flight segment. This process is indicated by third sizing loop III in Figure 3.1. If for example the last flight segment increases some component sizing values, then these values are re-assessed in all previous flight segments. The flight mission is converged once all flight segments are converged. The sizing results include performance indicators at component level and at system level.

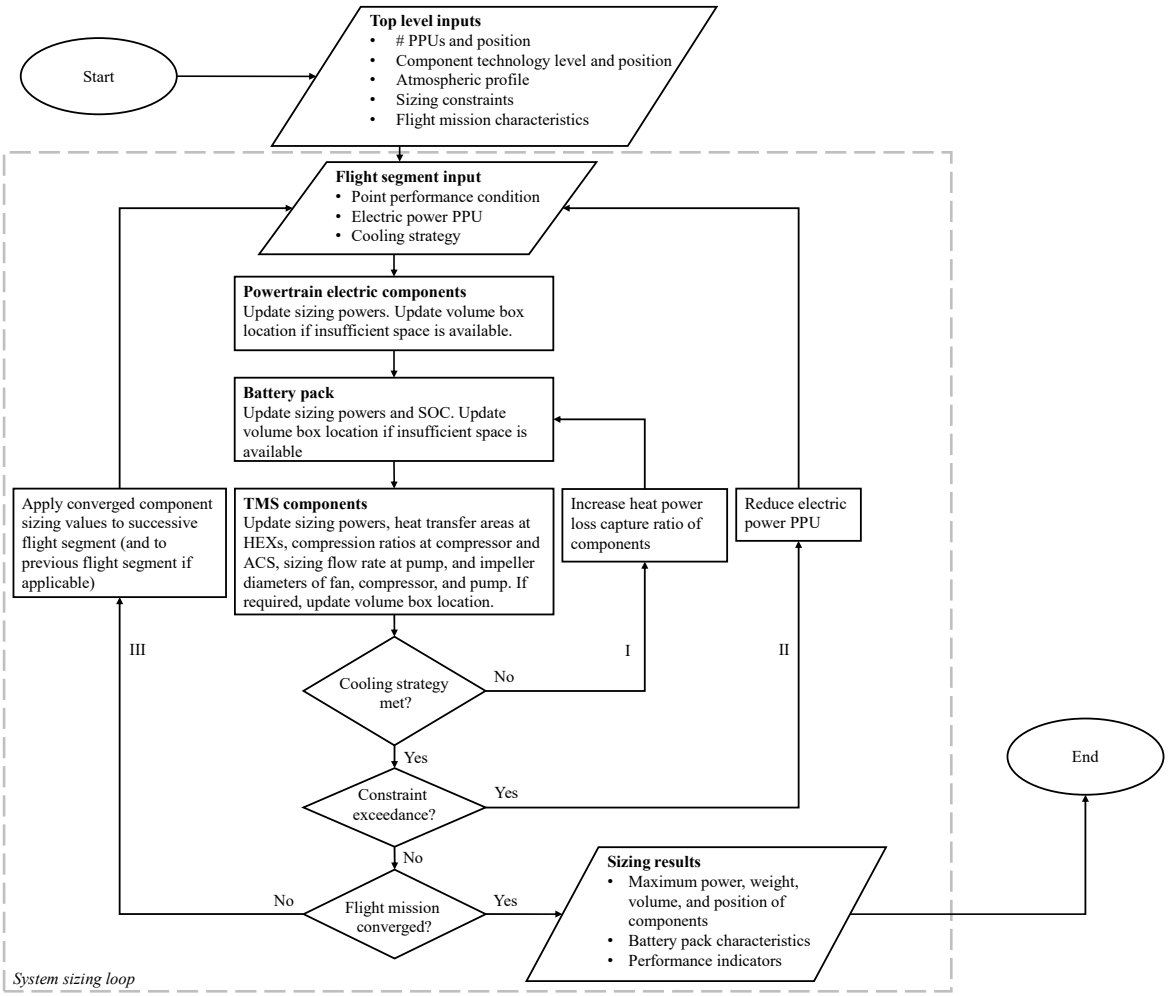

Figure 3.1: Flowchart of the used sizing methodology for a coupled propulsion and liquid cooling system.

3.1.1. SYSTEM ARCHITECTURE OVERVIEW

The centralised liquid cooled TMS (red box) and the electric part of the parallel HEP (blue box) are shown in Figure 3.2. For the sake of capturing the essential system behaviour characteristics, a centralised cooling approach is considered. Nonetheless, if the TMS fails, a second cooling system should be present for redundancy reasons. The term "system" is used to capture all components within red and blue boxes of Figure 3.2.

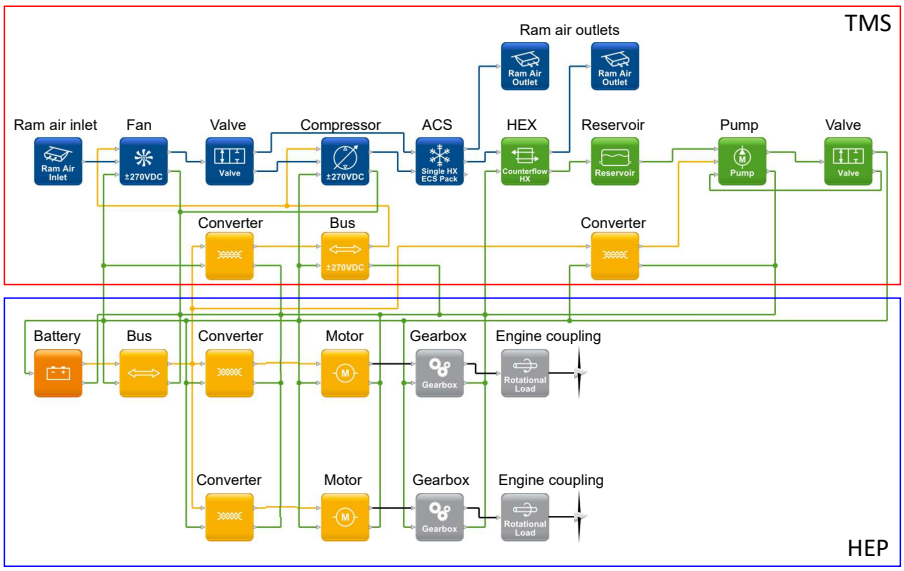

Figure 3.2: System architecture modelled in Pacelab SysArc. Blue routing lines: pneumatic ducts, green routing lines: hydraulic pipes, and yellow routing lines: electric cables.

3.2. PARALLEL HYBRID-ELECTRIC POWERTRAIN SIZING

The sizing of the parallel HEP excludes the sizing of the gas turbine to simplify the analysis. The presented methodology in Figure 3.1 is therefore only suitable to assess the impact on power usage, weight, and volume for a given hybrid-electric flight mission study. Resulting fuel consumption changes due to ram drag are not computed as simplistic low fidelity calculations are used and are therefore assumed insufficient for further processing. However, the calculated total drag coefficients at each flight segment are able to indicate critical flight segments. The HEP system components presented in Figure 3.2 are discussed separately. The general system characteristics are presented first.

3.2.1. GENERAL SYSTEM CHARACTERISTICS

Two general system parameters are used to assess the performance of the system, as shown in Figure 3.2. The chain efficiency (η_{chain}) is used to analyse the total effective power received by all the PPUs ($P_{\text{PPU}_{\text{total}}}$) at the gearbox ($P_{\text{GB}}$) from the battery pack ($P_{\text{bat, out}}$) [133], see Equation (3.1):

$$\eta_{\text{chain}} = \frac{P_{\text{PPU}_{\text{total}}}}{P_{\text{bat, out}}} = \frac{\prod_{i=1}^{j} P_{\text{GB},i}}{P_{\text{bat, out}}} \tag{3.1}$$

The Combined Specific Power (CSP) [kW/kg] indicates the effective total power at the PPUs over the total system weight (m_{system}) and is given in Equation (3.2):

$$\text{CSP} = \frac{P_{\text{PPU}_{\text{total}}}}{m_{\text{system}}} = \frac{P_{\text{PPU}_{\text{total}}}}{\sum_{i=1}^{n} m_i} \tag{3.2}$$

The index i covers all j or n components. The battery efficiency is not taken into account in the chain efficiency and no losses are assumed at the mechanical power node between the gearbox and the PPU.

3.2.2. GEARBOX

The equations presented are for a single PPU powertrain. As the total PPU power is equally split over two power trains, the sizing for both PPUs is identical. With the imposed electric PPU power in combination with the gearbox (GB) efficiency (η_{GB}), the gearbox input power ($P_{GB,\,in}$) can be calculated as presented in Equation (3.3):

$$P_{GB,\,in} = \frac{P_{GB,\,out}}{\eta_{GB}} \tag{3.3}$$

The resulting total heat power ($P_{GB,\,loss}$) loss can then be computed by Equation (3.4):

$$P_{GB,\,loss} = P_{GB,\,in} \cdot (1 - \eta_{GB}) \tag{3.4}$$

The weight estimation is based on a weight correction factor (k_{GB}), the in and out rotational speeds (rpm) and the weight of the cold plates (CPs) ($m_{GB,\,CP}$) as given in Equation (3.5) [134]:

$$m_{GB} = k_{GB} \cdot P_{GB}{}^{0.76} \cdot \frac{\text{rpm}_{in}{}^{0.13}}{\text{rpm}_{out}{}^{0.89}} + m_{GB,\,CP} \tag{3.5}$$

The weight correction factor accounts for a certain system technology level. A weight correction factor of 34 is suggested for current technology, while for future technologies a value of 26 is proposed [81]. The out rotational speed depends on the maximum tip Mach number of the PPU. The in rotational speed follows from a given gearbox ratio [20]. The volume is estimated by its sizing power (P_{GB}) divided by a constant power density value ($\hat{v}$) [kW/m^3] and the cold plate volume ($v_{GB,\,CP}$), as can be seen in Equation (3.6):

$$v_{GB} = \frac{1}{\hat{v}_{GB}} \cdot P_{GB} + v_{GB,\,CP} \tag{3.6}$$

For both the gearbox weight and volume estimation, the cold plate weight and volume are taken into account. Cold plate sizing is further discussed in Cold plates. The efficiency of the gearbox is estimated based on an efficiency curve for a given part load [135]. The efficiency curve used is presented in Figure 3.3. It can be seen that the highest efficiency is obtained at maximum allowed power usage.

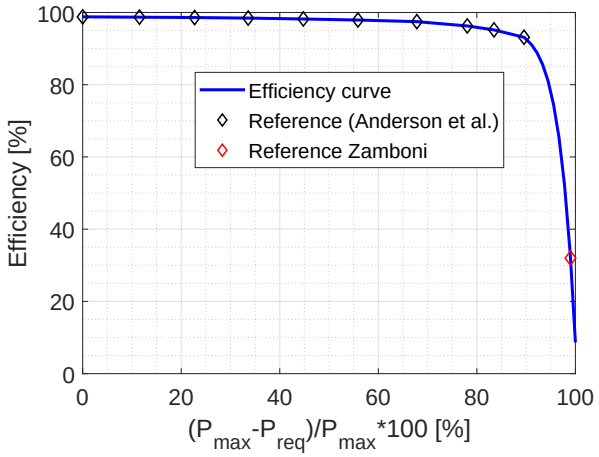

Figure 3.3: Gearbox efficiency curve [20, 135].

3.2.3. ELECTRIC MOTOR

The conversion of electric power into mechanical shaft power is accomplished by an Electric Motor (EM) in the parallel HEP. A permanent magnet Brushless Direct Current (BLDC) electric motor is modelled, similar to [20], as it allows for a high power density, efficiency, reliability, and low maintenance [1] [136, 137]. Furthermore, for an inner rotor BLDC design, the main heat source is the outer stator at which current goes through the coils. This makes cooling less difficult as the heat source is not rotating and located at the outer layer

[1] Siemens. eAircraft. URL: https://www.bbaa.de/fileadmin/user_upload/02-preis/02-02-preistraeger/newsletter-2019/02-2019-09/02_Siemens_Anton.pdf . Accessed on: 16/09/2020

[137, 138].

The required input power ($P_{\text{EM, in}}$) for the electric motor and the heat power loss ($P_{\text{EM, loss}}$) are based on the total efficiency ($\eta_{\text{EM, total}}$) of the electric motor itself and of the electric motor controller (EMC). The required input power and total heat loss power are given in Equation (3.7) and Equation (3.8) respectively:

$$P_{\text{EM, in}} = \frac{P_{\text{EM, out}}}{\eta_{\text{EM, total}}} = \frac{P_{\text{GB, in}}}{\eta_{\text{EM}} \cdot \eta_{\text{EMC}}} \tag{3.7}$$

$$P_{\text{EM, loss}} = P_{\text{EM, in}} \cdot (1 - \eta_{\text{EM, total}}) \tag{3.8}$$

An electric motor controller is only coupled for weight, volume, and efficiency estimation purposes. A constant electric motor controller efficiency is imposed. Detailed modelling of the controller is not included in this study. The weight and volume for both the electric motor and electric motor controller are estimated with Specific Power values (SP) [kW/kg] and power density values ($\hat{\nu}$) [kW/m^3] times the sizing power (P_{EM}), see Equation (3.9) and Equation (3.10):

$$m_{\text{EM}} = \frac{1}{\text{SP}_{\text{EM}}} \cdot P_{\text{EM}} + \frac{1}{\text{SP}_{\text{EMC}}} \cdot P_{\text{EM}} + m_{\text{EM, CP}} \tag{3.9}$$

$$\nu_{\text{EM}} = \frac{1}{\hat{\nu}_{\text{EM}}} \cdot P_{\text{EM}} + \frac{1}{\hat{\nu}_{\text{EMC}}} \cdot P_{\text{EM}} + \frac{1}{\nu_{\text{EM, CP}}} \tag{3.10}$$

To mimic the behaviour of a BLDC electric motor, the parametric electric motor model from [139] is used to relate the torque, rotational speed, and the efficiency. In order to assess the practical limitations of an electric motor, the torque dependency on the angular velocity is first discussed.

The produced shaft power ($P_{\text{EM, shaft}}$) of an electric motor is given in Equation (3.11), as the product of the angular velocity (ω) times the torque (Q):

$$P_{\text{EM, shaft}} = \omega \cdot Q \tag{3.11}$$

The torque is proportional to the electric current (I) flowing trough the coils, the magnetic flux (Φ), and the electric motor constant (k_{EM}). The latter is used to include the number of turns (n) in each coil, the magnetic field strength (B), the wire length (l), and the radius of the coil (r) [138]. The term $2 \cdot B \cdot l \cdot r$ is the magnetic flux (Φ) going through a coil. The torque can then be rewritten by using the electric motor constant (k_{EM}), which possesses the electric motor characteristics such as the number of turns in every coil, the number of pole pairs, and more design aspects [138]. The rewritten toque expression is given in Equation (3.12):

$$Q = 2 \cdot n \cdot B \cdot l \cdot r \cdot I = k_{\text{EM}} \cdot \Phi \cdot I \tag{3.12}$$

Due to the working mechanism of a BLDC, the current carrying coils at the outer placed armature cause the permanent magnets at the inside to move, where the magnetic field moves along. According to Faraday's Law [2], any change in the magnetic field flux results in an opposed electromotive force (or voltage). This self-generated electric potential or voltage is called back-Electromotive Force (EMF). Therefore, the electric motor partly acts as a generator [3]. The resulting effect of the back-EMF is that the input voltage that powers the electric motor is opposed by the induced back-EMF and therefore causing the electric current flow in the electric motor to reduce. The back-EMF depends on the number of turns, and the angular velocity. If the same BLDC electric motor is taken as for Equation (3.12), the same value for K_{EM} exists. As the same design characteristics captured in K_{EM} also influence the back-EMF behaviour, the back-EMF ($V_{\text{back-EMF}}$) can be written as follows:

$$V_{\text{back-EMF}} = k_{\text{EM}} \cdot \Phi \cdot \omega \tag{3.13}$$

The resulting voltage is therefore the difference between the supply voltage (V_{in}) and the back-EMF ($V_{\text{back-EMF}}$). The electric current can then be calculated with the electrical resistance of the armature coils (R_{a}) in Equation (3.14):

[2] LumenLearning. Faraday's Law. URL: https://courses.lumenlearning.com/boundless-physics/chapter/magnetic-flux-induction-and-faradays-law/. Accessed on: 16/09/2020

[3] LumenLearning. Back-EMF. URL: https://courses.lumenlearning.com/physics/chapter/23-6-back-emf/. Accessed on: 16/09/2020

$$I = \frac{V}{R_a} = \frac{V_{in} - V_{back\text{-}EMF}}{R_a} = \frac{V_{in}}{R_a} - \frac{k_{EM} \cdot \Phi}{R_a} \cdot \omega \tag{3.14}$$

It can be seen from Equation (3.14) that the current drops for a fixed magnetic flux intensity with an increase in angular velocity due to the back-EMF presented in Equation (3.13). Furthermore, when Equation (3.14) is substituted in Equation (3.12) the following results:

$$Q = \frac{k_{EM} \cdot \Phi \cdot V_{in}}{R_a} - \frac{(k_{EM} \cdot \Phi)^2}{R_a} \cdot \omega \tag{3.15}$$

From Equation (3.15), it can be seen that the torque linearly drops with increase in angular velocity. If the electric motor stalls, the highest electric current exists and therefore the maximum torque is reached. However, due to high heat losses around this point, practical limitations are present to prevent too high internal losses that generate heat. The increase in angular speed is controlled by adapting the supply voltage.

In order to construct a parametric model to estimate the electric motor efficiency as a function of angular velocity and torque, the effect of losses should first be assessed. The four main power loss types are the same for all electric motors [138]. First, copper losses account for electric resistance in e.g. copper wires that cause heat generation. Copper losses, also called Ohmic losses ($P_{Ohmic\ loss}$) as discussed in Section 2.3, are proportional to the square of the electric current and given in Equation (3.16):

$$P_{Ohmic\ loss} = I^2 \cdot R \tag{3.16}$$

Given Equation (3.12), the torque is a function of electric current. Therefore, the copper losses are proportional to the square of the torque and a constant k_c that depends on electric motor characteristics, as shown in Equation (3.17):

$$\text{Copper losses} = k_c \cdot T^2 \tag{3.17}$$

Second, iron losses are magnetic effects present in the iron part of the electric motor. These are also called core losses. There are two main causes for iron losses. The first cause is related to the required energy to continuously magnetise and demagnetise the iron material. The aligning and re-aligning of the magnetic dipoles is slower than the change of magnetic field and causes hysteris losses. The second cause is related to electric current heating of the iron material. These electric currents are caused in the iron material by the changing magnetic field. These currents are also called eddy currents. The iron losses are therefore proportional to the magnetic field change frequency and a constant k_i, which is assumed to be a constant to capture a first order estimation, see Equation (3.18):

$$\text{Iron losses} = k_i \cdot \omega \tag{3.18}$$

Third, friction and windage losses are related to contact surfaces of moving parts and the drag of rotating components. Friction losses and windage losses are scaled with a certain friction torque Q_f and windage scaling factor k_w. Related loss equations are given in Equation (3.19) and Equation (3.20) respectively:

$$\text{Friction losses} = Q_f \cdot \omega \tag{3.19}$$

$$\text{Windage losses} = k_w \cdot \omega^3 \tag{3.20}$$

Fourth, constant losses which do not vary with rotational speed or torque, i.e they occur also in the stationary condition. Constant losses are indicated with the letter C in this context. The total power loss is found by combining the separate losses. The iron losses and the friction losses are combined in the constant k_i as they are both proportional to the angular velocity. The total power loss is given in Equation (3.21):

$$\text{Total power loss} = k_c \cdot T^2 + k_i \cdot \omega + k_w \cdot \omega^3 + C \tag{3.21}$$

The total efficiency can then be calculated if electric motor characteristics are known by Equation (3.22):

$$\eta_{EM} = \frac{P_{EM,\ shaft}}{P_{EM,\ shaft} + P_{loss,\ total}} = \frac{\omega \cdot Q}{\omega \cdot Q + P_{loss,\ total}} = \frac{\omega \cdot Q}{\omega \cdot Q + \left(k_c \cdot T^2 + k_i \cdot \omega + k_w \cdot \omega^3 + C\right)} \tag{3.22}$$

In order to create a scalable 'rubber' electric motor model without prior knowledge of the internal configuration characteristics, an approach is suggested by [139], which is based on the loss equations discussed so far. The scalable electric motor approach uses seven parameters to fully define the relation between the efficiency, rotational speed and torque.

The first four parameters are used to account for the discussed power losses. The optimum torque ($\hat{Q}$), optimum efficiency ($\hat{\eta}$), optimum rational speed ($\hat{\omega}$), and the parasite loss ratio (k_0) are used in Equations (3.23) to (3.26) as follows:

$$k_c = \frac{\hat{\omega} \cdot (1 - \hat{\eta})}{2 \cdot \hat{Q} \cdot \hat{\eta}} \tag{3.23}$$

$$k_i = \frac{-3 \cdot C_0}{2 \cdot \hat{\omega}} + \frac{\hat{Q} \cdot (1 - \hat{\eta})}{4 \cdot \hat{\eta}} \tag{3.24}$$

$$k_w = \frac{C_0}{2 \cdot \hat{\omega}^3} + \frac{\hat{Q} \cdot (1 - \hat{\eta})}{4 \cdot \hat{\eta} \cdot \hat{\omega}^2} \tag{3.25}$$

$$C = k_0 \cdot \frac{\hat{\omega} \cdot \hat{Q}}{6} \cdot \frac{1 - \hat{\eta}}{\hat{\eta}} \tag{3.26}$$

The remaining three parameters (k_Q, k_P, and k_ω) are used to determine the practical limits of the electric motor in terms of maximum torque (Q_{rated}), maximum power (P_{rated}), and rotational speed limit (ω_{limit}) respectively. The practical limit parameters are given in Equations (3.27) to (3.30):

$$Q_{rated} = k_Q \cdot \hat{Q} \tag{3.27}$$

$$P_{rated} = k_P \cdot \hat{\omega} \cdot \hat{Q} \tag{3.28}$$

$$\omega_{limit} = k_\omega \cdot \hat{\omega} \tag{3.29}$$

If Equation (3.27) and Equation (3.28) are combined based on Equation (3.11), then the rated rotational speed (ω_{rated}) can be found:

$$\omega_{rated} = \frac{k_p}{k_Q} \cdot \hat{\omega} \tag{3.30}$$

The rated rotational speed corresponds to the value at which the electric motor achieved both the rated (or maximum) torque and power. With the presented seven parameters $(\hat{Q}, \hat{\eta}, \hat{\omega}, k_0, k_Q, k_P$, and $k_\omega)$, a scalable electric motor can be designed. An example of such a motor with normalised torque and rotational speed is given in Figure 3.4. The corresponding parameters are: $\hat{\eta} = 95\%$, $k_0 = 0.5$, $k_Q = k_P = k_\omega = 2$.

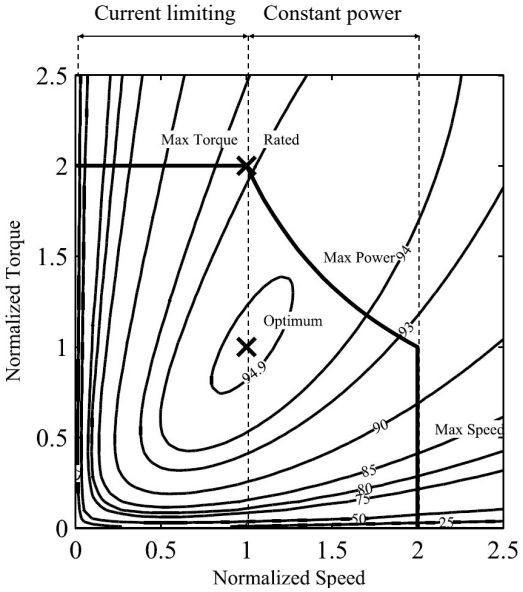

Figure 3.4: Electric motor efficiency map [139].

The practical limitations of an electric motor are also presented in Figure 3.4. A maximum torque segment is present $(0-\omega_{\text{rated}})$, which is limited by a maximum allowable electric current in the coils to prevent too high damaging heat generation. As the rotational speed increases by a higher supply voltage, the power increases as well. Similarly, the back-EMF increases also with higher rotational speed. The rated point is where the back-EMF limits the current that can be drawn from the supply [20]. The rated point is taken as sizing power point (rated power, P_{rated}) for the electric motor. The maximum power segment $(\omega_{\text{rated}}-\omega_{\text{limit}})$ is where the power stays constant with increase in rotational speed. Due to the increase in back-EMF, the torque starts to drop with increase in rotational speeds. The rotational speed limit (ω_{limit}) bounds the last practical limitation.

3.2.4. ELECTRIC ROUTING CABLE

The length (L) and position of the Electric Cables (CB) are a result of the automatic electric routing connection feature in Pacelab Sysarc. As non-superconducting electric transmission cables are used, a voltage drop ΔV is caused by the generated heat (Joule heating) as a function of the electric current (I). The voltage drop is based on a given Linear Resistance (LR) $[\Omega/m]$ as can be seen in Equation (3.31):

$$\Delta V_{\text{CB}} = I_{\text{CB}} \cdot L_{\text{CB}} \cdot \text{LR}_{\text{CB}} \tag{3.31}$$

The heat power loss ($P_{\text{CB, loss}}$) is given in Equation (3.32):

$$P_{\text{CB, loss}} = I_{\text{CB}} \cdot \Delta V_{\text{CB}} \tag{3.32}$$

The electric cable weight (m_{CB}) is calculated by a given Linear Density (LD) [kg/m], see Equation (3.33):

$$m_{\text{CB}} = L_{\text{CB}} \cdot \text{LD}_{\text{CB}} \tag{3.33}$$

3.2.5. POWER CONVERTER

The power converter is used to supply the correct voltage to the electric motor. The input power and heat loss power are given in Equation (3.34) and Equation (3.35):

$$P_{\text{PC, in}} = \frac{P_{\text{PC, out}}}{\eta_{\text{PC}}} = \frac{P_{\text{CB, in}}}{\eta_{\text{PC}}} \tag{3.34}$$

$$P_{\text{PC, loss}} = P_{\text{PC, in}} \cdot (1-\eta_{\text{PC}}) \tag{3.35}$$

The weight and volume estimations are based on the sizing power (P_{PC}), the specific power (SP_{PC}), and power density value ($\hat{v}_{\text{PC}}$) in Equation (3.36) and Equation (3.37) respectively:

$$m_{PC} = \frac{1}{SP_{PC}} \cdot P_{PC} + m_{PC,\,CP} \tag{3.36}$$

$$v_{PC} = \frac{1}{\hat{v}_{PC}} \cdot P_{PC} + v_{PC,\,CP} \tag{3.37}$$

The efficiency of the power converter is determined by an efficiency curve for a given part load [140], presented in Figure 3.5. This efficiency curve is translated along the y-axis to account for a different maximum efficiency.

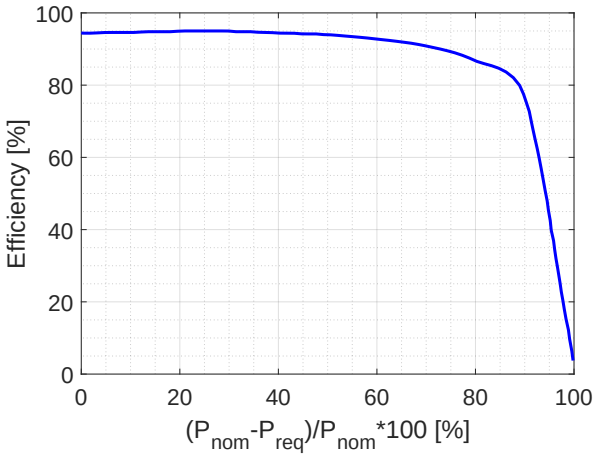

Figure 3.5: Power converter efficiency curve [140].

3.2.6. ELECTRIC BUS

The distribution of electric power over multiple transmission cables is done by the electric bus. The voltage drop (ΔV_{bus}) is again used to determine the heat power loss, given in Equation (3.39):

$$\Delta V_{bus} = I_{bus} \cdot R_{bus} \tag{3.38}$$

$$P_{bus,\,loss} = I_{bus} \cdot \Delta V_{bus} \tag{3.39}$$

$$P_{bus,\,in} = P_{bus,\,out} + P_{bus,\,loss} \tag{3.40}$$

The weight estimation (m_{bus}) is given in Equation (3.41), at which a weight isolation factor ($k_{isolation}$) is used in case a specific power value (SP_{bus}) is used without including isolation. The volume estimation (v_{bus}) is given in Equation (3.42):

$$m_{bus} = k_{isolation} \cdot \left(\frac{1}{SP_{bus}} \cdot P_{bus} \right) + m_{bus,\,CP} \tag{3.41}$$

$$v_{bus} = \frac{1}{\hat{v}_{bus}} \cdot P_{bus} + v_{bus,\,CP} \tag{3.42}$$

3.2.7. BATTERY PACK

The battery pack (bat) consists of electro-chemical cells, cold plates and packaging. The cells are connected in series and in parallel in order to satisfy the required system voltage and power. These numbers are determined by the sizing power and the cell characteristics. The number of cells connected in series ($N_{cells,\,series}$) is calculated based on an imposed system voltage ($V_{system,\,max}$) and the maximum cell voltage ($V_{cell,\,full}$) as shown in Equation (3.43):

$$N_{cells,\,series} = \frac{V_{system,\,max}}{V_{cell,\,full}} \tag{3.43}$$

The number of cells connected in parallel is determined by the maximum electric system current ($I_{\text{system, max}}$), the maximum cell current ($I_{\text{cell, max}}$), and the lowest allowable SOC, as shown in Equation (3.44):

$$N_{\text{cells, parallel}} = \frac{I_{\text{system, max}}}{I_{\text{cell, max}}} \cdot (1 + \text{SOC}_{\text{min}}) \tag{3.44}$$

To account for the fact that Li-ion batteries have a lower SOC limit, the nominal number of connected cells in parallel is increased by the lower SOC limit ratio to compensate the not available capacity. The capacity of the battery (Q_{bat}) is calculated by the cell capacity (Q_{cell}) and the number of cells in parallel ($N_{\text{cells, parallel}}$) [4], given in Equation (3.45):

$$Q_{\text{bat}} = Q_{\text{cell}} \cdot N_{\text{cells, parallel}} \tag{3.45}$$

The total resistance of the battery pack (R_{bat}) can then be calculated by Equation (3.46), which is then used to compute the battery efficiency (η_{bat}) in Equation (3.47):

$$R_{\text{bat}} = R_{\text{cell}} \cdot \frac{N_{\text{cells, series}}}{N_{\text{cells, parallel}}} \tag{3.46}$$

$$\eta_{\text{bat}} = \eta_{\text{bat, max}} - \frac{I_{\text{bat, out}} \cdot R_{\text{bat}}}{V_{\text{bat, full}}} \tag{3.47}$$

Once the efficiency is known, the heat power loss ($P_{\text{bat, loss}}$) can be calculated based on the supplied battery power ($P_{\text{bat, out}}$), as shown in Equation (3.48):

$$P_{\text{bat, loss}} = P_{\text{bat, out}} \cdot \left(\frac{1}{\eta_{\text{bat}}} - 1 \right) \tag{3.48}$$

By using batteries as the second energy source, the risks of battery performance degradation and thermal runaways are present. As safety is of paramount importance, adequate cooling is required. To estimate the ratio of the total heat power loss that needs to be actively dissipated, a first order estimation is implemented based on the battery heat capacity [141]. This ratio is called the Heat Capture Ratio (HCR). In order to find the expression for the HCR, the total battery heat power loss ($P_{\text{bat, loss}}$) is first split into the active heat power loss ($P_{\text{bat, loss, active}}$) and the passive heat power loss ($P_{\text{bat, loss, passive}}$), given in Equation (3.49):

$$P_{\text{bat, loss}} = P_{\text{bat, loss, active}} + P_{\text{bat, loss, passive}} \tag{3.49}$$

For simplicity, it is assumed that non of the passive heat power loss is dissipated from the source by convection. Therefore, the total passive heat loss causes a temperature rise in the battery. On the other hand, the active heat power loss is actively taken away by the liquid cooled TMS. The first expression for the HCR can be defined in Equation (3.50):

$$\text{HCR}_{\text{bat}} = \frac{P_{\text{bat, loss, active}}}{P_{\text{bat, loss}}} = \frac{P_{\text{bat, loss}} - P_{\text{bat, loss, passive}}}{P_{\text{bat, loss}}} = 1 - \frac{P_{\text{bat, loss, passive}}}{P_{\text{bat, loss}}} \tag{3.50}$$

Furthermore, for simplicity reasons, the total weight of the battery pack (m_{bat}) [kg] is taken and multiplied by the cell specific heat capacity ($c_{p,\text{cell}}$) [J/kg/K] to get the battery heat capacity [J/K]. The heat capacity ($m_{\text{bat}} \cdot c_{p,\text{cell}}$) is then multiplied by the given allowed battery temperature change over a given time ($\frac{\Delta T}{\Delta t}$) [K/s] to acquire the corresponding amount of passive heat power loss ($P_{\text{bat, loss, passive}}$) [J/s] needed to achieve this temperature change over time. The second expression for the HCR can then be constructed in Equation (3.51):

$$\text{HCR}_{\text{bat}} = 1 - \frac{\frac{\Delta T}{\Delta t} \cdot m_{\text{bat}} \cdot c_{p,\text{cell}}}{P_{\text{bat, loss}}} = 1 - \frac{P_{\text{bat, loss, passive}}}{P_{\text{bat, loss}}} \tag{3.51}$$

HCR values > 0 indicate that active cooling is required, while values < 0 are an indication for active heating. In this study, only active cooling is considered. Neither radiation nor convection effects are taken into account. The total weight of the battery pack is the weight summation of all the cells ($m_{\text{bat, cells}}$), cold plates ($m_{\text{bat, CP}}$), and packaging ($m_{\text{bat, package}}$), as shown in Equation (3.52):

[4] Battery University. Parallel Battery Configurations. URL: https://batteryuniversity.com/learn/article/serial_and_parallel_battery_configurations. Accessed on: 17/09/2020

$$m_{\text{bat}} = m_{\text{bat, cells}} + m_{\text{bat, CP}} + m_{\text{bat, package}} \tag{3.52}$$

The weight contribution of the cells is calculated in Equation (3.53), based on the total battery energy (E_{bat}) [Wh]) divided by the specific energy (ϵ_{cell}) [Wh/kg]. The total battery energy is equal to the the battery charge capacity (Q_{bat}) [Ah] times the full battery voltage ($V_{\text{bat, full}}$):

$$m_{\text{bat, cells}} = \frac{E_{\text{bat}}}{\epsilon_{\text{cell}}} = \frac{Q_{\text{bat}} \cdot V_{\text{bat, full}}}{\epsilon_{\text{cell}}} = \frac{Q_{\text{cell}} \cdot N_{\text{cells, parallel}} \cdot V_{\text{bat, full}}}{\epsilon_{\text{cell}}} \tag{3.53}$$

To determine the battery package weight, the Battery Pack Burden ratio (BPB) is used. It is the ratio of the total non-battery cell weight over the total battery pack weight [11] presented in Equation (3.54):

$$m_{\text{bat, package}} = m_{\text{bat}} \cdot \text{BPB} - m_{\text{bat, CP}} \tag{3.54}$$

The volumetric shape of the battery pack is determined by three stack factors that determine the number of cells in x, y, and z direction. A cylindrical cell shape is used at which the height of the cells results from the imposed cell energy density (ED) [Wh/l] for a given cell diameter. The required coldplate and packaging volumes are uniformly added on top of the volumetric shape of the battery cells. The resulting battery volume (υ_{bat}) is given in Equation (3.55):

$$\upsilon_{\text{bat}} = \upsilon_{\text{bat, cells}} + \upsilon_{\text{bat, CP}} + \upsilon_{\text{bat, package}} \tag{3.55}$$

As the battery pack is the most important component in this study, it is essential to adequately estimate the actual battery voltage over time with the corresponding SOC. For this reason, the medium fidelity dynamic battery model is used from [142], which allows to capture the typical battery discharge characteristics needed for conceptual design studies. The same battery model is previously implemented in the hybrid-electric aircraft study of Cinar et al. [93]. A notional discharge curve for a typical Li-ion battery is given in Figure 3.6, where the voltage is plotted as a function of its capacity for a constant discharge current.

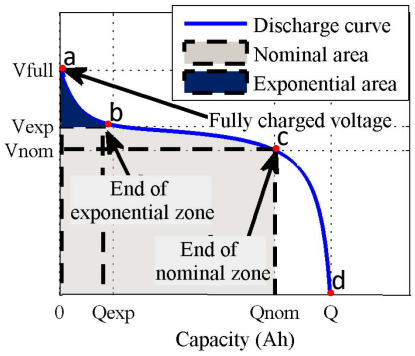

Figure 3.6: Characteristics of a typical Li-ion constant current discharge curve [142].

The used battery model will be explained on the basis of Figure 3.6. Four important points are indicated by a, b, c, and d. The fully charged voltage (V_{full}) is indicated at point a, at 0 Ah. The voltage curve is calculated with a constant discharge current and internal resistance. Once electric power is extracted from the battery, the voltage starts to drop exponentially until point b (V_{exp}, Q_{exp}). This region is called the exponential zone. Between point b and point c (V_{nom}, Q_{nom}) the voltage drop is less pronounced. This region is called the nominal zone. After the nominal zone, the voltage will decrease steeply until the the maximum capacity at point d (Q) is reached.

The used battery model allows to construct such discharge curves based on several parameters. Furthermore, it should be noted that temperature dependency on the discharge curve and the self discharge phenomenon are not taken into account in this model [142]. The battery model is further explained by first discussing the internal battery cell losses that occur once electric current starts to flow.

Three main types of internal battery cell losses can be identified and are visualised in Figure 3.7. These are the Internal Resistance (IR) losses, activation losses, and concentration losses. The term polarisation (or loss),

that is used in Figure 3.7, describes the change in electric potential (or voltage) of a cell from its open circuit value caused by an applied current. The first losses are the IR losses. These are caused by the internal cell resistance of the electrodes, membrane, and current collectors [143]. IR losses (or Ohmic losses) result in waste heat. The second losses are the activation losses. These are related to the energy consumption of the redox reactions themselves. The third type of losses are the concentration losses. These are caused by the non-uniformity of reactants at the electrodes. When higher discharge rates are present, less time is available for the reactants to mix, resulting in steeper concentration gradients at the electrode surface area and causing more resistance [144].

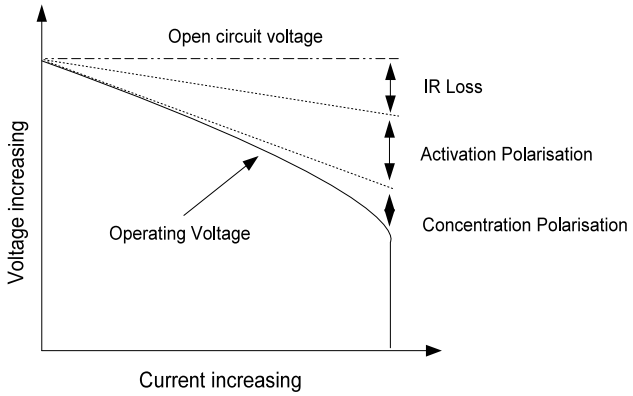

Figure 3.7: Breakdown of internal cell losses, expressed in voltage drop as a function of electric current [144].

The battery model predicts the battery voltage (V_{bat}) [V] based on internal cell losses. The general expression for Li-ion batteries is taken from [142] and given in Equation (3.56):

$$V_{\text{bat}} = V_0 - (R \cdot I) - K \cdot \frac{Q}{Q - Q_{\text{act}}} \cdot \left(Q_{\text{act}} + I^*\right) + A \cdot e^{-B \cdot Q_{\text{act}}} \tag{3.56}$$

To clarify Equation (3.56), the battery constant voltage is given by V_0, the term $(R \cdot I)$ presents IR losses, the polarisation constant K is expressed in [V/Ah] or [Ω], the Q represents the battery maximum capacity [Ah], as defined in Equation (3.45), the actual charge is given by Q_{act} [Ah], the term I^* represents the filtered discharge current [A], A is the exponential zone amplitude [V], and the last term B is the exponential zone time constant inverse [Ah^{-1}]. The filtered current I^* results from applying a first order low-pass current filter on the discharge current, which is favoured to improve simulation stability when this model is used in MATLAB/Simulink [145, 146]. However, the filtered current I^* is set in Pacelab Syarc as the actual discharge current I, as no stability issues are present.

The terms K, A, and B are calculated based on the typical points on the discharge curve from Figure 3.6. The polarisation constant K is calculated in Equation (3.57):

$$K = \frac{\left(V_{\text{full}} - V_{\text{nom}} + A \cdot \left(e^{(-B \cdot Q_{\text{nom}})} - 1\right)\right) \cdot (Q - Q_{\text{nom}})}{Q \cdot (Q_{\text{nom}} + I_{\text{nom}})} \tag{3.57}$$

As the battery pack consists of many cells, the typical discharge curve is scaled according to the numbers of cells connected in parallel and in series. The full battery voltage (V_{full}) is based on the imposed full cell voltage $V_{\text{cell, full}}$ and the number of cells connected in series ($N_{\text{cells, series}}$), see Equation (3.58):

$$V_{\text{full}} = V_{\text{cell, full}} \cdot N_{\text{cells, series}} \tag{3.58}$$

The battery constant voltage (V_0) depends on full battery voltage (V_{full}), the product of constant battery resistance (R_{bat}) and nominal current (I_{nom}), and the term A. V_0 is calculated in Equation (3.59):

$$V_0 = V_{\text{full}} + (R_{\text{bat}} \cdot I_{\text{nom}}) - A \tag{3.59}$$

The nominal current (I_{nom}) depends on the imposed nominal cell current ($I_{\text{cell, nom}}$). The term A is calculated based on the full battery voltage (V_{full}) and the exponential voltage (V_{exp}). The current I_{nom}, constant A, and constant B are presented in Equations (3.60) to (3.62):

$$I_{\text{nom}} = I_{\text{cell, nom}} \cdot N_{\text{cells, parallel}} \tag{3.60}$$

$$A = V_{\text{full}} - V_{\text{exp}} \tag{3.61}$$

$$B = \frac{3}{Q_{\text{exp}}} \tag{3.62}$$

The exponential voltage and charge ($V_{\text{exp}}, Q_{\text{exp}}$), corresponding to point b in Figure 3.6, are both based on the related imposed cell values. The definitions are given in Equations (3.63) and (3.64):

$$V_{\text{exp}} = V_{\text{cell, exp}} \cdot N_{\text{cells, series}} \tag{3.63}$$

$$Q_{\text{exp}} = Q_{\text{cell, exp}} \cdot N_{\text{cells, parallel}} \tag{3.64}$$

The nominal voltage and charge ($V_{\text{nom}}, Q_{\text{nom}}$) are similarly based on imposed related cell characteristics. These values correspond to point c in Figure 3.6 and are given in Equations (3.65) and (3.66):

$$V_{\text{nom}} = V_{\text{cell, nom}} \cdot N_{\text{cells, series}} \tag{3.65}$$

$$Q_{\text{nom}} = Q_{\text{cell, nom}} \cdot N_{\text{cells, parallel}} \tag{3.66}$$

In order to assess the battery SOC, i.e. how much charge capacity is left after a certain discharge time, the actual charge capacity (Q_{act}) should first be determined. The actual charge capacity is proportional to the discharge current (I) multiplied by a given discharge time (Δt) as shown in Equation (3.67):

$$Q_{\text{act}} = I \cdot \Delta t \tag{3.67}$$

The battery SOC can then be determined by Equation (3.68):

$$\text{SOC}_{i+1} = \text{SOC}_i - \int_{t_i}^{t_{i+1}} \frac{I}{Q} dt = \text{SOC}_i - \frac{Q_{\text{act}}}{Q} \tag{3.68}$$

Based on the fact that battery voltage will drop over time, a constant power requirement ($P = U \cdot I$) will imply a raise in electric discharge current. This inevitably results in that internal losses become more present and therefore further reduce the attainable output voltage, until discharge is stopped at the SOC limit.

3.3. THERMAL MANAGEMENT SYSTEM SIZING

A closed-loop liquid cooling system in combination with an air cycle system is modelled as the TMS. Liquid cooling is considered over active air cooling due to higher cooling capabilities [61]. Furthermore, the transportation of heat can be accomplished over a large distance [66]. Although a VCS cooling has a higher efficiency than liquid cooling, the design complexity is increased as two phases have to be considered. For the purpose of this study, liquid cooling is deemed to be the most suitable cooling strategy.

An air cycle system is coupled with the liquid cooling system to enable operation at high ambient temperature conditions. Nevertheless, the installation and maintenance of a liquid cooling should be kept in mind, considering leakage and related consequences.

In order to dissipate the calculated excessive heat from the components, cold plates are used to transfer this heat into the coolant flow. The required coolant flow rate (Q_{coolant}) [m^3/s] at each component is calculated in Equation (3.69):

$$Q_{\text{coolant}} = \frac{P_{\text{loss, active}}}{c_p \cdot \Delta T \cdot \rho_{\text{coolant}}} \tag{3.69}$$

The coolant flow rate is based on the calculated active heat power loss ($P_{\text{loss, active}}$) [J/S], the specific heat capacity (c_p) [J/kg/K], the temperature difference (ΔT) [K] between the coolant inlet temperature and the uniform component target temperature, and the density of the coolant (ρ_{coolant}) [kg/m^3]. The target temperature is set constant to simplify the calculations.

It should be noted that the hydraulic and pneumatic routing elements shown in Figure 3.2 also account for pressure losses. Only for the hydraulic pressure loss calculations, curved routing elements are taken into account. This is not the case for the pneumatic routing pressure loss calculation.

3.3.1. COLD PLATES

The capturing of excessive heat is accomplished by cold plates. A pressure drop results over the liquid cooling channels inside the cold plate, given by Equation (3.70).

$$\Delta p_{\text{CP}} = k_{\text{CP},1} \cdot \frac{Q_{\text{coolant}}}{N_{\text{CP}}} + k_{\text{CP},2} \cdot \left(\frac{Q_{\text{coolant}}}{N_{\text{CP}}} \right)^2 \tag{3.70}$$

The cold plate pressure drop expression is acquired based on a typical cold plate design for which an exponential relation was found based on constants $k_{\text{CP},1}$ and $k_{\text{CP},2}$, see Figure A.1. Cold plates are connected in parallel in case multiple cold plates are required, to reduce the total pressure drop [5]. The number of cold plates is calculated in Equation (3.71) and based on the active heat loss power ($P_{\text{loss, active}}$) [kW], a given cold plate power density ($\hat{v}_{\text{CP}}$) [kW/m^3], and the single cold plate volume ($v_{\text{CP, single}}$) [m^3]:

$$N_{\text{CP}} = \frac{P_{\text{loss, active}}}{\hat{v}_{\text{CP}} \cdot v_{\text{CP, single}}} \tag{3.71}$$

The total weight (m_{CP}) and volume (v_{CP}) are calculated in Equation (3.72) and Equation (3.73) respectively:

$$m_{\text{CP}} = \frac{P_{\text{loss, active}}}{\text{SP}_{\text{CP}}} \tag{3.72}$$

$$v_{\text{CP}} = v_{\text{CP, single}} \cdot N_{\text{CP}} \tag{3.73}$$

3.3.2. HYDRAULIC PUMP

The main purpose of the hydraulic pump is to provide sufficient coolant flow, to balance the required heat dissipation rates, while overcoming the overall hydraulic system pressure loss. The latter is the summation of the pressure losses in the routing elements and at the components. The hydraulic pump performance is based on typical curves for the static pressure increase and efficiency with mass flow as input. Hydraulic affinity laws are used to size the impeller diameter and to correct for rotational speeds change [147].

Two sets of hydraulic affinity laws can be defined, one for a constant impeller diameter (D) and one for a constant rotational speed (N) [148]. A change in impeller diameter, for a constant rotational speed can be required to match the peak system demand in terms of flow rate (Q) and pressure head (H). The related affinity laws are presented in Equations (3.74) and (3.75):

$$\frac{Q_1}{Q_2} = \frac{D_1}{D_2} \tag{3.74}$$

$$\frac{H_1}{H_2} = \left(\frac{D_1}{D_2} \right)^2 \tag{3.75}$$

A change in rotational speed, for a given sized impeller diameter, accounts for changing coolant flow rates and pressure head as given in Equations (3.76) and (3.77):

$$\frac{Q_1}{Q_2} = \frac{N_1}{N_2} \tag{3.76}$$

$$\frac{H_1}{H_2} = \left(\frac{N_1}{N_2} \right)^2 \tag{3.77}$$

[5] Engineering ToolBox. Pipes in Parallel. URL: https://www.engineeringtoolbox.com/pipes-series-parallel-d_1787.html. Accessed on: 18/09/2020

Furthermore, the hydraulic system is operating at a fixed system pressure to prevent coolant phase changes. The hydraulic pump is powered by a connected BLDC motor. The same electric motor model as described in Section 3.2.3 is used and sized to match the power and rotational speed requirement. The resulting electric power required by the hydraulic pump ($P_{\text{HP, in}}$) is based on the static pressure increase (Δp_{total}) [N/m^2] times the coolant flow rate (Q_{coolant}) [m^3/s], which is the power demand, and divided by the total efficiency ($\eta_{\text{HP, total}}$), given in Equation (3.78):

$$P_{\text{HP, in}} = \frac{P_{\text{HP, demand}}}{\eta_{\text{HP, total}}} = \frac{\Delta p_{\text{HP}} \cdot Q_{\text{coolant}}}{\eta_{\text{HP}} \cdot \eta_{\text{HP, EM}} \cdot \eta_{\text{HP, EMC}}} \tag{3.78}$$

$$P_{\text{HP, loss}} = P_{\text{HP, in}} - P_{\text{HP, demand}} \tag{3.79}$$

The weight (m_{HP}) and volume (v_{HP}) of the turbomachinery part of the hydraulic pump are estimated based on scaling factors ($k_{\text{HP, m}}, k_{\text{HP, v}}$), see Figure A.4 and are shown in Equation (3.80) and Equation (3.81) respectively:

$$m_{\text{HP}} = k_{\text{HP, m}} \cdot Q_{\text{coolant}} + \frac{1}{\text{SP}_{\text{HP, EM}}} \cdot P_{\text{HP}} + \frac{1}{\text{SP}_{\text{HP, EMC}}} \cdot P_{\text{HP, EMC}} + m_{\text{HP, CP}} \tag{3.80}$$

$$v_{\text{HP}} = k_{\text{HP, v}} \cdot Q_{\text{coolant}} + \frac{1}{\hat{v}_{\text{HP, EM}}} \cdot P_{\text{HP}} + \frac{1}{\hat{v}_{\text{HP, EMC}}} \cdot P_{\text{HP, EMC}} + v_{\text{HP, CP}} \tag{3.81}$$

3.3.3. HYDRAULIC ROUTING PIPE

The hydraulic routing pipe elements include a pressure loss (Δp) calculation based on the dynamic pressure (p_{dynamic}) and two friction factors (f) for straight and curved hydraulic pipes, see Equation (3.82):

$$\Delta p_{\text{pipe}} = p_{\text{dynamic}} \cdot \left(f_{\text{straight}} + f_{\text{curved}}\right) \tag{3.82}$$

These friction factors is called the Darcy–Weisbach friction factors. They depend on the Reynolds number (Re) and the roughness height relative to the inside diameter:

$$f = f\left(Re, \frac{\text{height}_{\text{roughness}}}{D_{\text{inside}}}\right) \tag{3.83}$$

The Darcy–Weisbach friction factor is numerically approximated by using the implicit Colebrook-White equation [149]. The sum of all individual pressure losses represents the total hydraulic pressure loss.

3.3.4. PNEUMATIC ROUTING DUCT

The pressure loss (Δp_{duct}) for a pneumatic routing duct is a function of the length (L), the mass flow rate ($\dot{m}$), the Darcy–Weisbach friction factor (f), the density (ρ), and the inside diameter (D_{inside}), given in Equation (3.84):

$$\Delta p_{\text{duct}} = \frac{8 \cdot L \cdot \dot{m}^2 \cdot f}{\rho \cdot \pi^2 \cdot {D_{\text{inside}}}^5} \tag{3.84}$$

The pressure loss is scaled with the Darcy–Weisbach friction factor, which is presented in Equation (3.83). The effect of curvature on the pressure loss is not taken into account. The resulting total pneumatic pressure loss is the sum of all individual pressure losses.

3.3.5. HEAT EXCHANGER

The collected waste heat is rejected at the air-to-liquid HEX. A counter-flow type is chosen as it allows for higher efficiencies than a cross-flow type [150]. The maximum possible heat exchange performance is based on the e-NTU method, which describes the overall effectiveness as a function of the Number of Transfer Units (NTU) and the ratio of heat capacity rates (C^*) as presented in [150, 151]. The NTU value is based on the overall heat transfer coefficient (U_{HEX}) [W/m^2/K] times the heat transfer area ($A_{\text{HEX, heat}}$)[m^2], divided by the minimum heat capacity rate (C_{min}) [W/K] to compute the maximum possible heat transfer between the air and the liquid. The calculation of the NTU is given in Equation (3.85):

$$\text{NTU} = \frac{U_{\text{HEX}} \cdot A_{\text{HEX, heat}}}{C_{\text{min}}} = \frac{U_{\text{HEX}} \cdot A_{\text{HEX, heat}}}{\min\left(\dot{m}_i \cdot c_{p_i}\right)} \tag{3.85}$$

The heat capacity rate (C) is calculated by the mass flow ($\dot{m}$) [kg/s] times the specific heat capacity (c_p) [J/kg/K]. As the liquid coolant flow (Q_{liquid}) is expressed in m^3/s, it is multiplied by its density (ρ_{liquid}) to get the mass flow. The c_p is a function of its temperature. Furthermore, the $c_{p,\text{liquid}}$ depends on the type of coolant used:

$$C_{\text{air}} = \dot{m}_{\text{air}} \cdot c_{p,\text{air}}(T) \tag{3.86}$$

$$C_{\text{liquid}} = Q_{\text{liquid}} \cdot \rho_{\text{liquid}} \cdot c_{p,\text{liquid}}(T, \text{liquid type}) \tag{3.87}$$

The ratio of heat capacity rates (C^*) is determined by respectively the minimum and maximum heat capacity rate, as given in Equation (3.88):

$$C^* = \frac{C_{\text{min}}}{C_{\text{max}}} \tag{3.88}$$

The actual heat transfer ($\dot{Q}$) results from multiplying the maximum heat transfer ($\dot{Q}_{\text{max}}$) with the effectiveness (ε). The effectiveness is equal to $\dot{Q}/\dot{Q}_{\text{max}}$, as shown in Equation (3.89):

$$\dot{Q} = \dot{Q}_{\text{max}} \cdot \varepsilon = C_{\text{min}} \cdot \left(T_{\text{hot, in}} - T_{\text{cold, in}}\right) \cdot \frac{\dot{Q}}{\dot{Q}_{\text{max}}} \tag{3.89}$$

The corresponding effectiveness ($\varepsilon_{\text{counter-flow}}$) for a counter-flow HEX is given in Equation (3.90). A rather similar expression can be found for a cross-flow HEX type [151]:

$$\varepsilon_{\text{counter-flow}} = \frac{1 - e^{(-\text{NTU}\cdot(1-C^*))}}{1 - C^* \cdot e^{(-\text{NTU}\cdot(1-C^*))}} \tag{3.90}$$

The weight (m_{HEX}) estimation is based on the combined material density ($\rho_{\text{HEX, total}}$) [kg/m^3] of the total HEX and corrected for the internal shape by the porosity factor (k_{porosity}) [152], given in Equation (3.91):

$$m_{\text{HEX}} = \rho_{\text{HEX, total}} \cdot v_{\text{HEX}} \cdot (1 - k_{\text{porosity}}) \tag{3.91}$$

The volume (v_{HEX}) is estimated by the effective heat transfer area ($A_{\text{HEX, heat}}$) [m^2] divided by the surface compactness ratio ($k_{\text{HEX, compactness ratio}}$) [$m^2/m^3$], see Equation (3.92):

$$v_{\text{HEX}} = \frac{A_{\text{HEX, heat}}}{k_{\text{HEX, compactness ratio}}} \tag{3.92}$$

3.3.6. PNEUMATIC FAN

Based on thermal balances at the HEXs, the required coolant air flow is calculated to reject excessive heat. In case not enough ram air is generated by the aircraft itself, the fan is turned on to compensate for this deficit. The electric power demand, the heat power loss, and the estimation for the weight and volume are fairly similar to those of the hydraulic pump. The scaling factor $k_{\text{PF,v}}$ is derived from Figure A.2. Equation (3.93) to Equation (3.96) present power related calculations and the estimations for the weight and volume:

$$P_{\text{PF, in}} = \frac{P_{\text{PF, demand}}}{\eta_{\text{PF}} \cdot \eta_{\text{PF, EM}} \cdot \eta_{\text{PF, EMC}}} = \frac{\Delta p_{\text{PF}} \cdot \dot{m}_{\text{PF, air}}}{\rho_{\text{PF, air}} \cdot \eta_{\text{PF}} \cdot \eta_{\text{PF, EM}} \cdot \eta_{\text{PF, EMC}}} \tag{3.93}$$

$$P_{\text{PF, loss}} = P_{\text{PF, in}} - P_{\text{PF, demand}} \tag{3.94}$$

$$m_{\text{PF}} = \frac{1}{\text{SP}_{\text{PF}}} \cdot P_{\text{PF}} + \frac{1}{\text{SP}_{\text{PF, EM}}} \cdot P_{\text{PF}} + \frac{1}{\text{SP}_{\text{PF, EMC}}} \cdot P_{\text{PF}} + m_{\text{PF, CP}} \tag{3.95}$$

$$v_{\text{PF}} = k_{\text{PF,v}} \cdot Q_{\text{air}} + \frac{1}{\hat{\nu}_{\text{PF, EM}}} \cdot P_{\text{PF}} + \frac{1}{\hat{\nu}_{\text{PF, EMC}}} \cdot P_{\text{PF}} + v_{\text{PF, CP}} \tag{3.96}$$

The sizing of the pneumatic fan is based on the pneumatic affinity laws for similar reasons as discussed for the hydraulic pump in Hydraulic pump. The pneumatic affinity laws use the pressure (p) and slightly differ from the hydraulic pneumatic affinity laws [153]. They are given in Equations (3.97) to (3.100):

$$\frac{Q_1}{Q_2} = \left(\frac{D_1}{D_2}\right)^3 \tag{3.97}$$

$$\frac{p_1}{p_2} = \left(\frac{D_1}{D_2}\right)^2 \tag{3.98}$$

$$\frac{Q_1}{Q_2} = \frac{N_1}{N_2} \tag{3.99}$$

$$\frac{p_1}{p_2} = \left(\frac{N_1}{N_2}\right)^2 \tag{3.100}$$

3.3.7. PNEUMATIC COMPRESSOR

In operational situations with high atmospheric temperatures, ram air needs to be cooled before entering the air-to-liquid HEX. This cooling is required to create a sufficient temperature difference between the ram air stream and the liquid coolant flow in the HEX. A possible solution to accomplish this pre-cooling of high temperature air is based on the open inverse Brayton cycle principle, also known as the bootstrap air cycle [54, 154]. The principle is based on two ram air streams. The main air stream, used in the air-to-liquid HEX, is first compressed, after which it is cooled down by the coolant air stream in the Air Cycle System (ACS), see Figure 3.2. The working principle of the ACS is further discussed in Air cycle system.

The compression of the main air stream is done by the pneumatic compressor. The pneumatic compressor sizing is based on pneumatic affinity laws as well, presented in Pneumatic fan. A BLDC motor, as explained in Section 3.2.3, is again modelled to power the pneumatic compressor. The required power for the pneumatic compressor ($P_{\text{PCO, in}}$) is based on the compression power ($P_{\text{PCO, demand}}$) and is a function of the pressure ratio, as can be seen in Equations (3.101) and (3.102):

$$P_{\text{PCO, in}} = \frac{P_{\text{PCO, demand}}}{\eta_{\text{PCO}} \cdot \eta_{\text{PCO, EM}} \cdot \eta_{\text{PCO, EMC}}} = \frac{\dot{m}_{\text{PCO, air}} \cdot c_{p_{\text{average}}} \cdot \left(T_{\text{PCO, out}} - T_{\text{PCO, in}}\right)}{\eta_{\text{PCO, total}}} \tag{3.101}$$

$$T_{\text{PCO, out}} = T_{\text{PCO, in}} \cdot \left(1 + \frac{\left(\frac{p_{\text{out}}}{p_{\text{in}}}\right)^{\frac{\gamma-1}{\gamma}} - 1}{\eta_{\text{PCO}}}\right) \tag{3.102}$$

In Equations (3.101) and (3.102), the specific heat capacity ($c_{p_{\text{average}}}$) is a function of the averaged inlet and outlet temperature and the heat capacity ratio for air is given by γ. The heat power loss, weight, and volume are calculated in the same manner as for the pneumatic fan in Pneumatic fan. The only difference is that the volume of the turbomachinery part of the pneumatic compressor is estimated based on the impeller diameter ($D_{\text{PCO, impeller}}$) and calculated in Equation (3.103) as follows:

$$v_{\text{PCO}} = \left(2 \cdot D_{\text{PCO, impeller}}\right)^3 \tag{3.103}$$

3.3.8. AIR CYCLE SYSTEM

After the main air stream is compressed, it is cooled by the the coolant air stream in the ACS. In case the ambient temperature is cold enough, no use of the combined pneumatic compressor and ACS is required. Air will then bypass the compressor and the ACS. These bypass ducts and actuators are not modelled, although this functionality is used. The ACS consists of a coupled compressor and turbine (air cycle machine: ACM) and an air-to-air HEX. Based on a thermal balance for the TMS components, the required coolant air stream from the air-to-liquid HEX is used to determine the coolant air stream in the ACS. The working principle with corresponding mathematical model of the ACS used is described in [54].

The pre-cooled air flow, which is used in the air-to-liquid HEX, is qualitatively presented by a T-s diagram in Figure 3.8. Ambient air is collected by the ram air inlet and raises both pressure and temperature (1-2). In case the fan is used, the pressure and temperature will slightly increase (2-3). If the compressor is also required to operate, the pressure and temperature significantly increase (3-4). Once the air has arrived at the ACS, it first goes through the compressor, to further increase the pressure and temperature (4-5). Second, the heat is extracted at the air-to-air HEX, to lower the temperature at the cost of some pressure loss (5-6). Third, the air flows trough the turbine to significantly reduce the pressure, while the temperature drops under the ambient

air temperature (6-7). The air flow leaves the ACS and goes into the air-to-liquid HEX to act as the heat sink for the collected waste heat (7-8). A pressure loss is again present over the HEX. The heated air flow is finally rejected at the ram air outlet at point 8.

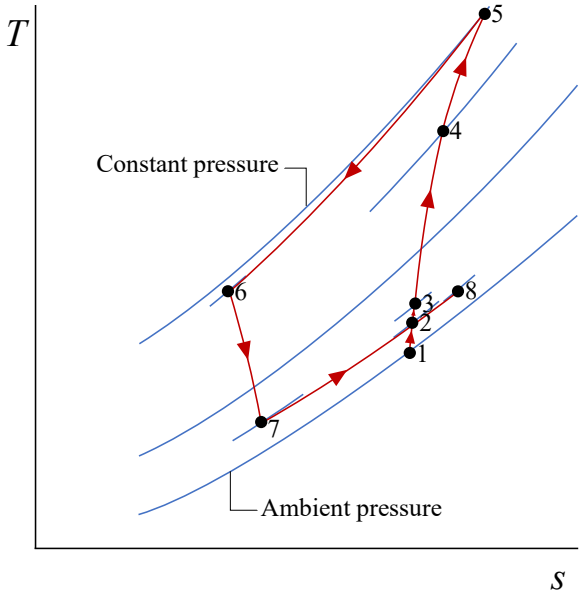

Figure 3.8: T-s diagram of the pre-cooled air coolant flow used at the air-to-liquid HEX.

A cross-flow type HEX is used in the ACS to allow enough installation and maintenance space at the cost of reduced efficiency [150]. The weight (m_{ACS}) of the ACS is split into the weight of the ACM ($m_{\text{ACS, ACM}}$) and the weight of the HEX ($m_{\text{ACS, HEX}}$), given in Equation (3.104):

$$m_{\text{ACS}} = \left(m_{\text{ACS, ACM}} + m_{\text{ACS, HEX}}\right) \cdot k_{\text{ACS}} \tag{3.104}$$

A correction factor (k_{ACS}) is used to account for additional smaller component weights in the ACS. The HEX weight is estimated with the same approach as is described in Heat exchanger. The weight ($m_{\text{ACS, ACM}}$) and volume ($v_{\text{ACS, ACM}}$) of the ACM are calculated by the scaling factors ($k_{\text{ACS, m}}$, $k_{\text{ACS, v}}$), see Figure A.3, based on the sizing air flow ($\dot{m}_{\text{ACS}}$) and given in Equation (3.105) and in Equation (3.106) respectively:

$$m_{\text{ACS, ACM}} = k_{\text{ACS, m}} \cdot v_{\text{ACS}} \tag{3.105}$$

$$v_{\text{ACS, ACM}} = k_{\text{ACS, v}} \cdot \dot{m}_{\text{ACS}} \tag{3.106}$$

3.3.9. RAM AIR INLET / OUTLET

The total required air flow is collected via a single ram air inlet and two ram air outlets are used to eject the coolant air flows to the ambient. The ram efficiencies for both the ram air inlet and outlets are set constant over the flight mission to simplify the calculation. In reality, if the required air flow is less than the maximum attainable ram air flow, the ram air flow is controlled by variable geometry inlet doors. This functionality is mathematically used in this study, however it is not modelled. The standard isentropic relations are used to compute the ram air pressure and temperatures, given in Equation (3.107) to Equation (3.109):

$$T_{\text{ram, in}} = T_{\text{ambient}} \cdot \left(1 + \frac{\gamma - 1}{2} \cdot M^2\right) \tag{3.107}$$

$$p_{\text{ram, in}} = p_{\text{ambient}} \cdot \left(1 + \eta_{\text{ram, in}} \cdot \frac{\gamma - 1}{2} \cdot M^2\right)^{\frac{\gamma}{\gamma - 1}} \tag{3.108}$$

$$T_{\text{ram, out}} = T_{\text{in}} \cdot \left(1 - \eta_{\text{ram, out}} \cdot \left(1 - \left(\frac{p_{\text{out}}}{p_{\text{in}}}\right)^{\frac{\gamma - 1}{\gamma}}\right)\right) \tag{3.109}$$

The general expression for the drag coefficient increment ($\Delta C_{D,\text{ram}}$) due to momentum drag (N_{drag}) is given in Equation (3.110), with V as the velocity:

$$\Delta C_{D,\text{ram}} = \frac{N_{\text{drag}}}{p_{\text{ambient}} \cdot A_{\text{wing, ref}}} = \frac{\dot{m}_{\text{ram}} \cdot V_{\text{ram}}}{p_{\text{ambient}} \cdot A_{\text{wing, ref}}} = \frac{\dot{m}_{\text{ram}} \cdot \frac{\dot{m}_{\text{ram}}}{\rho \cdot A_{\text{ram}}}}{p_{\text{ambient}} \cdot A_{\text{wing, ref}}} \tag{3.110}$$

The resulting total drag coefficient ($C_{D,\text{ram, total}}$) from the inlet and outlets is given in Equation (3.111):

$$C_{D,\text{ram, total}} = \sum_{i=1}^{n} \Delta C_{D,\text{ram, } i} \tag{3.111}$$

Neither weight nor volume calculations are included, as they are considered part of the structural design of the aircraft.

3.4. TEMPERATURE PROFILES

Three different atmospheric temperature profiles are used in this study, presented in Figure 3.9. The hot day temperature profile is used to size the thermally-controlled electric propulsion system, as is suggested by [42, 65]. Moreover, the maximum and average temperature of Brasilia International Airport [6] are plotted as well, to empathise the realistic need to size for a hot day scenario. The tropical day profile lies in between the International Standard Atmosphere (ISA) and the hot day temperature profiles.

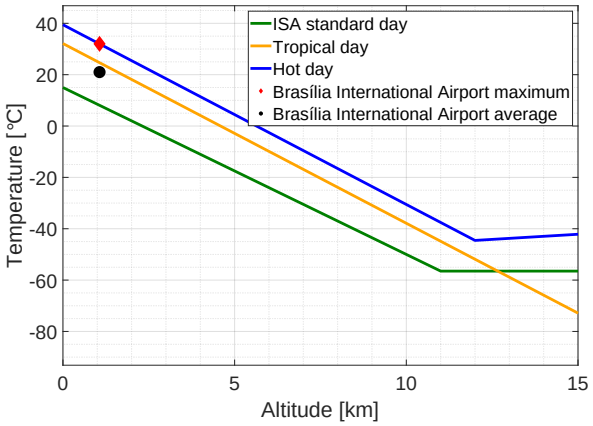

Figure 3.9: Atmospheric temperature profiles [6].

[6] World Weather Online. Brasilia. URL: https://www.worldweatheronline.com/brasilia-weather/distrito-federal/br.aspx. Accessed on: 19/09/2020

4

VALIDATION

This chapter is divided in two sections. First, the validation of individual components in presented in Section 4.1. Second, the baseline design characteristics for the parallel HEA are given in Section 4.2.

4.1. COMPONENT VALIDATION

As no similar adequate reference data could be found in literature for this thermally-controlled electric propulsion system architecture, validation is performed at individual system component level. The parametric models that are defined in more detail apply for the battery pack, electric motor, heat exchanger, and the ACS. These are validated in this section, along with behaviour characteristics of the fan, compressor, and pump. The control valves only account both for a fixed pressure ratio loss of 1 % and are not further modelled. The coolant reservoir is only included for visual purposes No calculation at the reservoir itself are performed.

4.1.1. BATTERY PACK MODEL

The battery model results at cell level are compared with results found in [93], that uses the same battery model. The considered cell characteristics are summarised in Table 4.1.

Table 4.1: Validation battery cell characteristics [93].

Parameter	Value
Cell capacity [Ah]	2.6
Cell full voltage [V]	4.2
Cell exponential zone charge [Ah]	0.1277
Cell exponential zone voltage [V]	3.889
Cell nominal current [A]	1.13
Cell nominal zone charge [Ah]	2.351
Cell nominal zone voltage [V]	3.6
Cell resistance [Ω]	0.01385

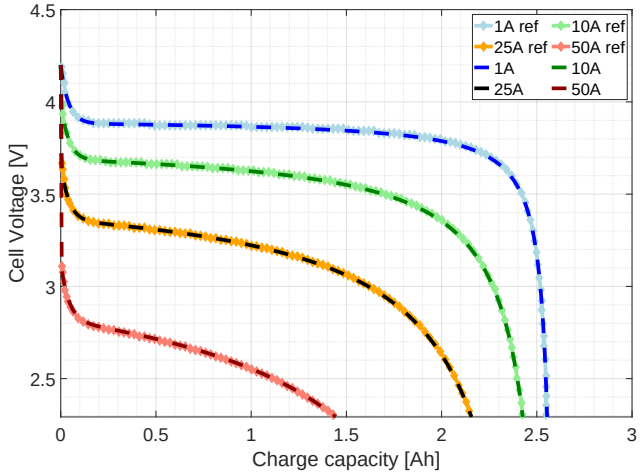

Figure 4.1: Battery pack validation, at cell level [93].

Four discharge curves, expressed in voltage as a function of the charge capacity, are compared in Figure 4.1. The corresponding discharge currents are set constant, where the blue line indicates a discharge current of 1 A. Similarly, the green line indicates a discharge current of 10 A. The overlay of the discharge curves shows the same model behaviour, due to the fact that the reference discharge curves originate from a simulation as well. Furthermore, the typical steeper drop in voltage with higher discharge currents can be noted, due to higher internal losses [93, 142]. When higher discharge currents are applied, the total energy (V · Ah) that can

be extracted from the same battery cell is less, as the cut-off voltage is reached earlier (e.g. if a fictive cut-off voltage is set at 2.5 V).

4.1.2. ELECTRIC MOTOR

The electric motor model behaviour is compared to a motor map of a real BLDC electric motor [1] (orange coloured) in Figure 4.2. The motor map shows the constant efficiency curves as a function of the torque and rotational speed. The blue curves at the right hand side of the Figure 4.2 indicate the constant power, where the maximum power is indicated by 100 %. The motor operating envelope is bounded by the maximum torque of 300 Nm, the maximum power of 125 kW, and the maximum rotational speed of 8000 rpm. Although the black efficiency curves do not perfectly match the reference data, on average the model sufficiently captures the effect of rotational speed and torque on the efficiency. As the torque, power, and rotational speed bounds of an electric motor are of prime concern, these should be captured to allow safe usage [139].

For the constant maximum power segment (blue dashed curve at 100 %), the torque is approximated well by the inverse of the rotational speed ($Q = P/\omega$). However, the real motor maximum power bound shows a rather linear decrease in power between 2500 rpm - 5000 rpm. Such a bound should be manually added in the model if this motor would be used. The power decrease for the real motor from 5000 rpm is probably linked to thermal issues to assure safe operations. As the real motor is liquid cooled [1], cooling limitations could be reached in that area, or related heating issues at the electric motor controller could be present.

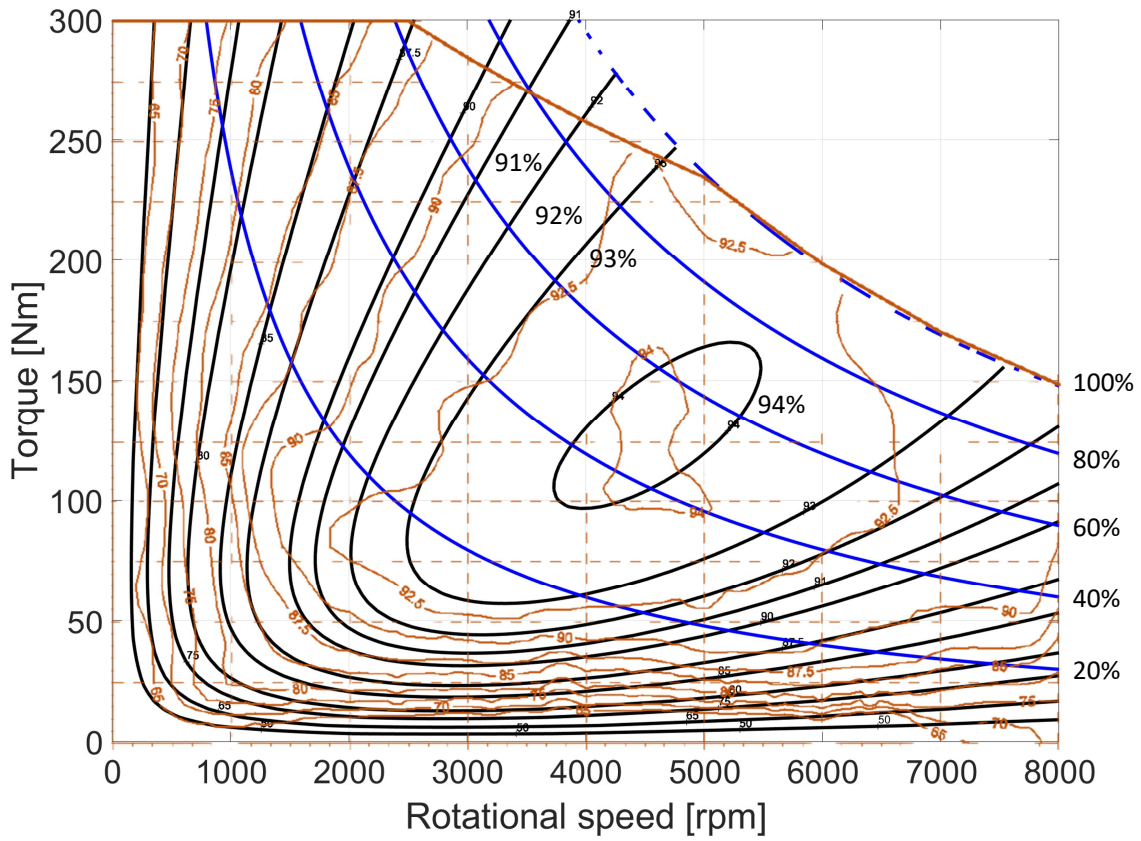

Figure 4.2: Electric motor validation ($\hat{Q} = 125\,\text{Nm}$, $\hat{\eta} = 94.1\,\%$, $\hat{\omega} = 4500\,\text{rpm}$, $k_0 = 0.95$, $k_Q = 2.4$, $k_P = 2.12$, and $k_\omega = 1.78$) [1].

[1] UQM. Powerphase HD 125. URL: https://wiki.neweagle.net/ProductDocumentation/EV_Software_and_Hardware/Traction_Inverters/UQM/PowerPhase_125_DataSheet.pdf. Accessed on: 21/09/2020

4.1.3. HEAT EXCHANGER

The counter-flow air-to-liquid HEX is validated in Figure 4.3, based on the effectiveness as a function of the NTU. The HEX model result in Figure 4.3b matches the typical curvature shape as shown in Figure 4.3a. The term C_{min}/C_{max} represents the ratio of heat capacity rates (C^*), given in Equation (3.88). Furthermore, cross-flow HEXs behave in a similar way [151].

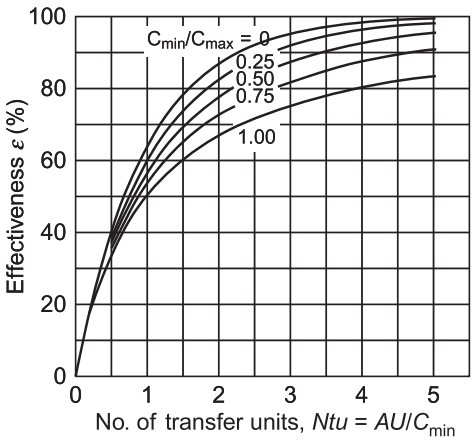

(a) Typical effectiveness for a counter-flow HEX [151].

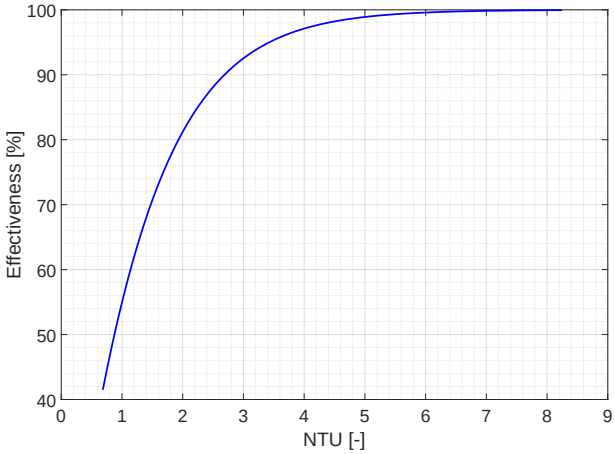

(b) Counter-flow HEX model result for the effectiveness as a function of NTU.

Figure 4.3: Counter-flow heat exchanger validation.

4.1.4. AIR CYCLE SYSTEM

The ACS is validated by comparing the coolant air flow rate behaviour as a function of the overall pressure ratio with a similar reference curve. The presented ACS model curve in Figure 4.4b qualitatively matches the behaviour of the reference ACS [155], shown in Figure 4.4a. Both pressure ratios presented include pre-compression, performed by an external compressor. The constant cooling load used in Figure 4.4a is 7.5 kW compared to 100 kW for Figure 4.4b, which explains the difference in absolute values for the air flow rates.

With a higher pressure ratio, the required coolant air flow starts to drop steeply, after which it flattens. This behaviour is probably driven by the diminishing increase of the NTU with higher pressure ratios, causing the effectiveness to also increase in a diminishing manner. According to Equations (3.86) and (3.89), for a constant heat load with a higher temperature difference and effectiveness, the mass flow rate goes down.

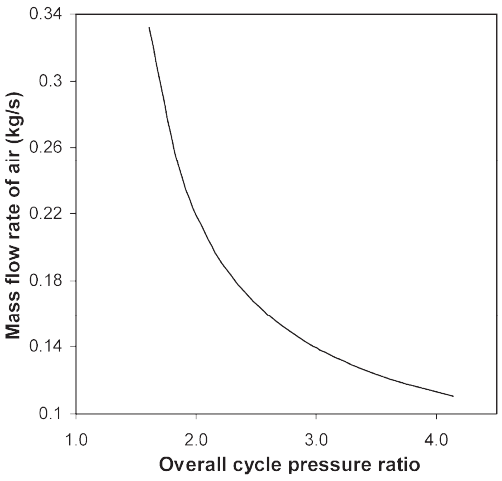

(a) Air mass flow rate as function of system pressure ratio [155].

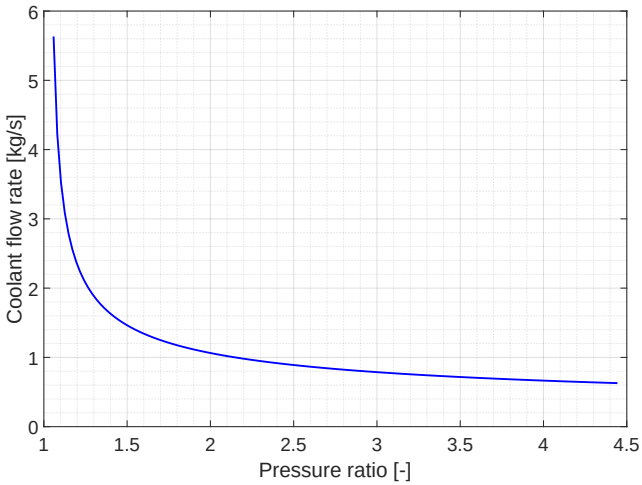

(b) ACS model result for the coolant air mass flow rate as a function of pressure ratio model.

Figure 4.4: Validation of the ACS.

4.1.5. FAN, COMPRESSOR, AND PUMP

The fan and compressor performance curve sizing characteristics are presented in Figures 4.5a and 4.5b. A typical reference pressure curve (blue) with corresponding impeller diameter is used. The impeller diameter can either be decreased or increased for a given rpm value, see the red curves in Figures 4.5a and 4.5b respectively. When the rpm is adjusted after the diameter, the green curve results. The corresponding efficiency, represented by the yellow line, indicates the mass flow that should be selected to acquire the highest efficiency. This shows the interaction between the mass flow rate, the pressure increase, and the corresponding efficiency. It must be noted that the reference pressure ratio curve for the compressor in Figure 4.5b has values below 1, which should be all above 1 for compression. This is due to a software related implementation flaw, noticed after the results are generated. The impact of this is that the volumetric sizing of the compressor is overestimated, due to a large increase in diameter, as can be seen in Figure 4.5b. Nevertheless, only feasible operating points of the compressor could be used, as the software can not mathematically converge with compression ratio values below unity.

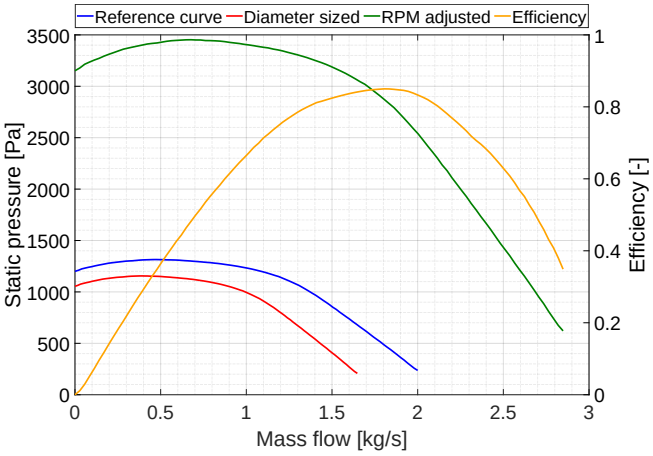

(a) Fan pressures and efficiency curves.

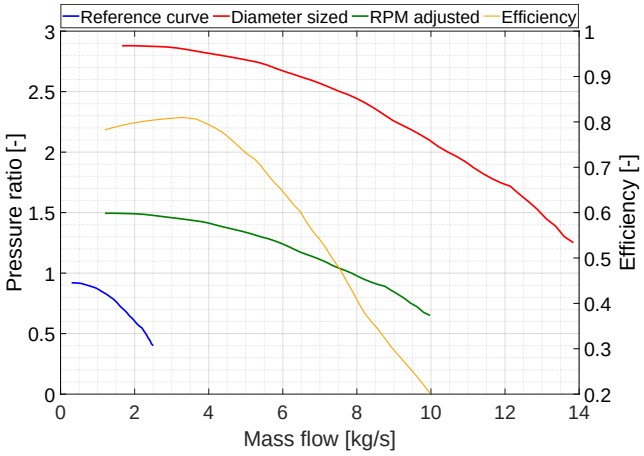

(b) Hydraulic pump pressures and efficiency curves.

Figure 4.5: Fan and compressor validation.

The sizing of the pump performance is also based on affinity laws, similar to the sizing procedure of the fan and compressor. An example study is presented in Figure 4.6a, that shows the different pump curves for different flight segments. It can be seen that the black line (first cruise segment) corresponds to the highest head demand, implying the highest heat load. The related yellow efficiency line indicates again the mass flow that should be used for the highest efficiency. The impact of a lower rotational speed on the efficiency is illustrated in Figure 4.6b. It shows a telescopic horizontal translation effect on the efficiency curve.

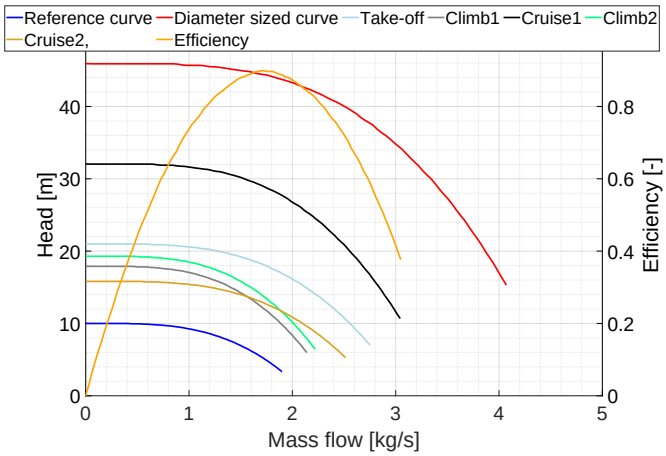

(a) Pump pressures and efficiency curves.

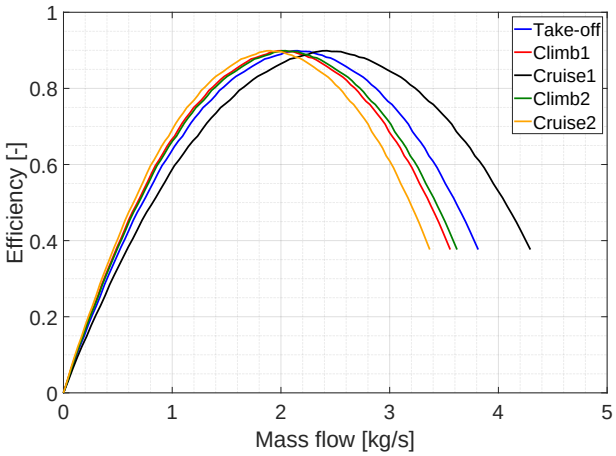

(b) Pump efficiency curves.

Figure 4.6: Hydraulic pump validation.

4.2. BASELINE DESIGN VALIDATION

The typical characteristics of the ATR72-600 regional turboprop aircraft are presented along with relevant data from the used reference parallel HEA study [20]. The harmonic flight mission used is taken from [20], according to data found in literature [15, 18, 156, 157]. The harmonic flight mission characteristics are shown in Table 4.2, where TOFL, and LFL stand for take-off field length and landing field length respectively.

Table 4.2: Harmonic flight mission parameters [15, 18, 20, 156, 157].

Harmonic mission		Reserves	
Passengers #	70	Diversion range [km]	188
Passenger weight [kg]	95	Diversion cruise altitude [m]	2743
Payload [kg]	7500	Hold time [min]	30
En-route range [km]	1525		
Cruise altitude [m]	5182		
Cruise Mach [-]	0.41		
Maximum TOFL [m]	1333		
Maximum LFL [m]	1067		
Taxi [min]	2 x 5		

Relevant results found in the reference parallel HEA study [20] are presented and compared to the conventional ATR72-600 characteristics in Table 4.3. Volume estimations are not considered in the reference study. Therefore, the total baggage volume of the conventional ATR72-600 [2] is assumed to be present in the baseline parallel HEA. For this study, the Maximum Take-off Weight (MTOW), Zero-Fuel Weight (ZFW), Operating Empty Weight (OEW), mission fuel weight, baggage volume, and the total PPU shaft power are assumed to be constant. The power distribution and the corresponding shaft power hybridisation strategy for the reference parallel HEA study are given in Figures B.1 and B.2 respectively.

Table 4.3: Comparison of the ATR72-600 and the used baseline parallel HEA [2] [20, 156].

Parameter	ATR72-600	Baseline parallel HEA	Difference [%]
Maximum take-off weight [kg]	23000	25600	+11.3
Zero-fuel weight [kg]	21000	21800	+3.81
Operating empty weight [kg]	13500	14300	+5.93
Payload [kg]	7500	7500	+0.00
Mission fuel weight [kg]	2000	1740	-13.0
Battery weight [kg]	-	2049	-
Baggage volume [m^3]	9.78	9.78	+0.00
Total PPU shaft power [MW]	4.10	4.46	+8.78

4.2.1. SIZING CONSTRAINTS

In order to let the sizing process converge, three hypothetical system sizing constraints have been set:

- Maximum ram air inlet mass flow: 10 kg/s
- Minimum chain efficiency: 70 %
- Maximum cooling power ratio: 15 %

4.2.2. PLANFORM COMPARISON

Finally, a planform comparison between the used aircraft model and the actual ATR72-600 [3] is presented in Figure 4.7. It includes the front, side, and top views. The main external shape differences are the following: more inboard position of the propellers, no fuselage-wing fairings, no fuselage-landing gear fairings, and a higher T-tail with a more aft position. Nevertheless, for the purpose of this conceptual study the aircraft model shape is deemed satisfactory.

[2] Amelia. ATR 72-600. URL: https://pro.flyamelia.com/en/flotte/atr72-2/. Accessed on: 22/09/2020

[3] Airlines travel. ATR 72-600. URL: https://en.airlinestravel.ro/a-sosit-primul-atr-72-600-tarom-inmatriculat-yr-atj-totul-despre-avantajele-acestui-model-de-avion.html. Accessed on: 22/09/2020

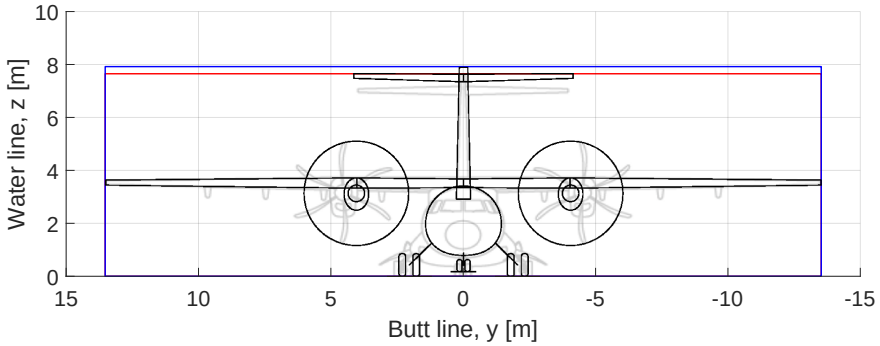

(a) Planform front.

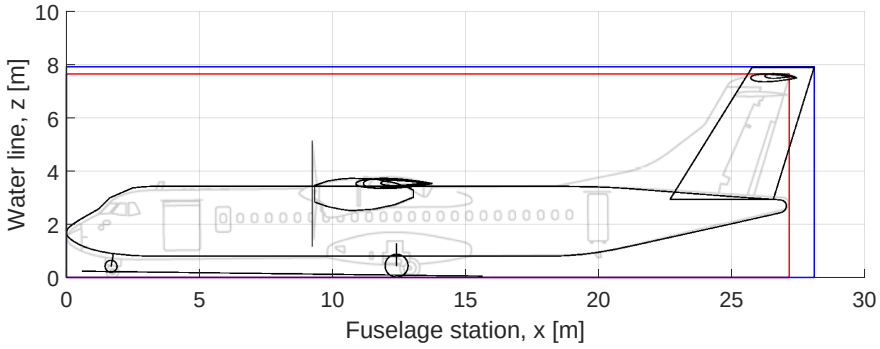

(b) Planform side.

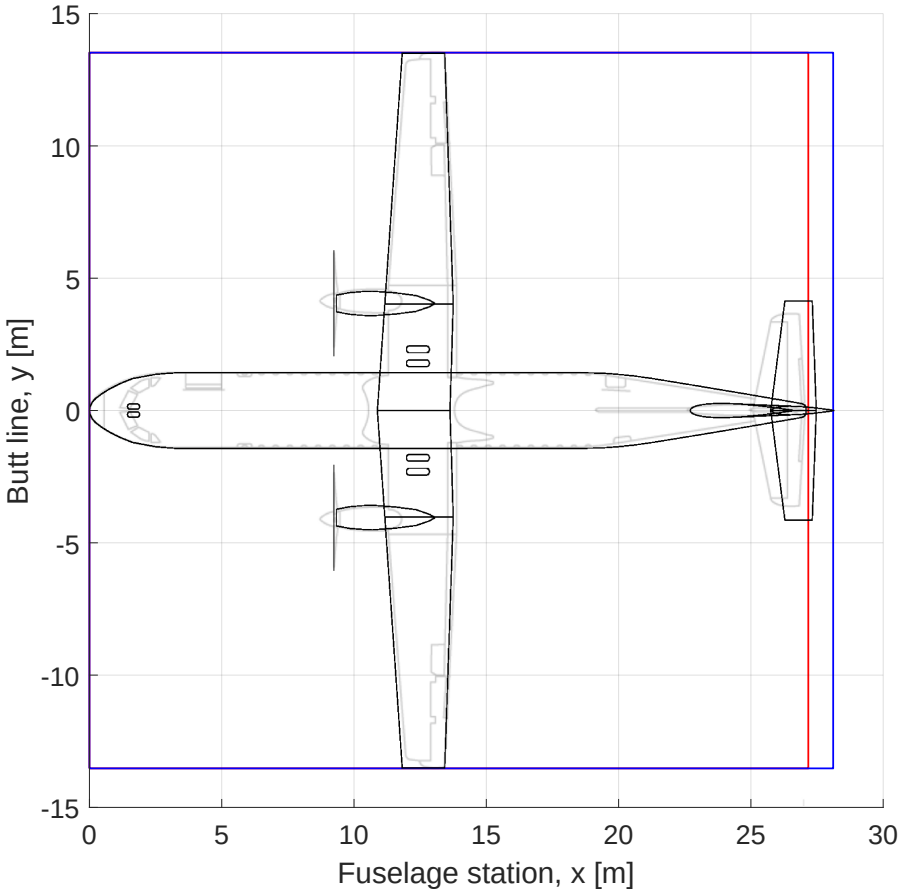

(c) Planform top.

Figure 4.7: Planform comparisons of the actual ATR72-600 (red box) and the modelled version used in this study (blue box) [3].

5

RESULTS

The results are divided into three sections. First, the sizing mission and technology level assumptions are given in Section 5.1. Second, the trade study results are discussed in Section 5.2. Third, the resulting weight and volume impact are presented in Section 5.3.

A simplified internal and external aircraft shape of the ATR72-600 is used, to visualise the volumetric system component impact. The term system includes both the TMS and the HEP components, as presented in Figure 3.2. Furthermore, limited flight mission results with near-term system technology level assumptions are presented. This scenario is deemed to be not feasible due the large weight and volume impact, discussed in Section 5.3. Likewise, a long-term technology level assumption scenario comprises high uncertainties. Therefore, only typical long-term component performance indicators are presented in Section 5.1, to give a notional insight in the potential development of the main system components. Mid-term technology developments are, however, seen as the limit of non-superconductive machines and are hypothesised to become viable from the year 2035 to 2040 [17, 158]. For this reason, only flight mission results with mid-term technology level assumptions are highlighted in this study in order to capture the coupled sizing characteristics and system behaviour. The results are generated with a manually driven system sizing loop, which is discussed in Section 3.1, due to implementation limitations in the software. Therefore, it should be emphasised that the obtained results are conservative.

5.1. SIZING CHARACTERISTICS

The flight mission altitude as a function of time is presented in Figure 5.1 [20]. For a flight segment at which hybridisation is required based on the mid-term hybridisation strategy of [20], a sizing point is set to represent that flight segment for simplicity purposes [43]. The sizing points are determined based on the average electric power demand by the PPUs between the start and the end of the flight segment. The resulting sizing points, corresponding to those averaged electric powers, are plotted as well in Figure 5.1. The five flight segments considered are the take-off, climb, cruise, diversion climb, and diversion cruise.

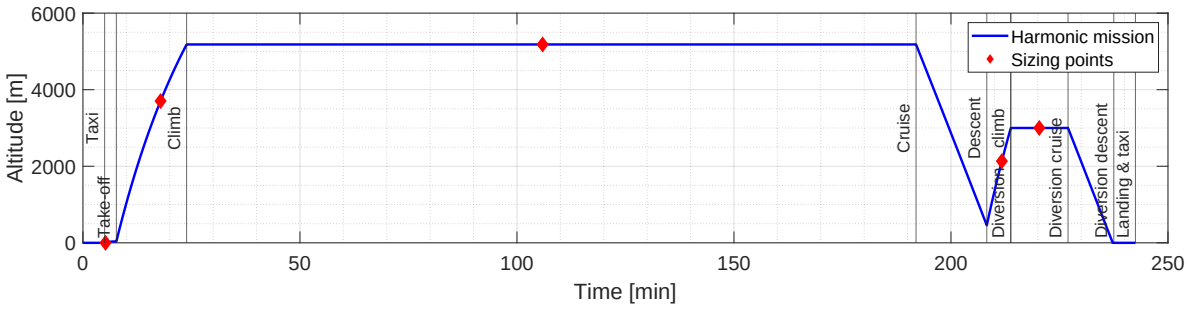

Figure 5.1: Harmonic flight mission [20].

The reference total electric power usage of the PPUs, calculated in [20], is simplified based on the determined sizing point powers, represented by the green line and red line respectively in Figure 5.2. The averaged electric power usage is set as the target usage for the sizing procedure. It should be noted that the reference data is the result of the mid-term technology level assumption study of [20]. Nevertheless, it is also used for the near-term scenario in this study.

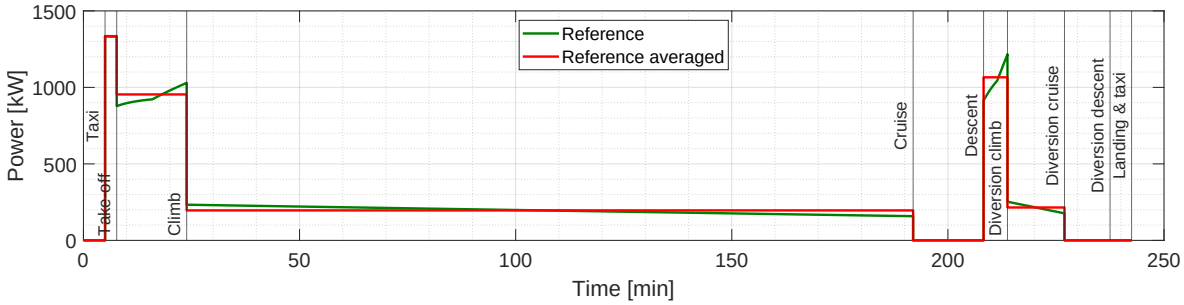

Figure 5.2: Reference total electric power usage of the PPUs [20].

For the system sizing, the hot day temperature profile is used, as presented in Figure 3.9. The atmospheric conditions along with the target electric power demands are summarised in Table 5.1. It can be noted that the sizing powers for the HEP components result from the take-off segment, supported by Figure 5.2. However, the resulting sizing powers used for the TMS components do not follow this pattern directly. This is further discussed in Section 5.2.1.

Table 5.1: Flight mission hot day sizing target conditions [20].

Parameter	Take-off	Climb	Cruise	Diversion climb	Diversion cruise
Altitude [m]	0	3700	5180	2130	3000
Temperature (atm) [°C]	39.5	13.5	3.18	24.5	18.5
Temperature (ram) [°C]	40.1	19.4	12.4	29.6	27.8
Air density [kg/m^3]	1.13	0.778	0.665	0.915	0.838
Pressure [bar]	1.01	0.640	0.527	0.782	0.701
Speed of sound [m/s]	354	339	333	346	342
Mach [-]	0.100	0.321	0.409	0.292	0.400
True air speed [m/s]	35.4	109	136	101	137
Total electric power [kW]	1335	954	196	1066	215
Duration [min]	2.68	16.2	168	5.53	13.2

The system voltage is set to 3000 VDC (Voltage Direct Current) to prevent high voltage drops and therefore power losses in the HEP [20, 159]. TMS components that use electric power operate at ±270 VDC (540 V) to match more electric aircraft standards [9]. Furthermore, the liquid coolant used is a water/glycol mixture (48 vol% water and 52 vol% ethylene glycol), to achieve lower system operating temperatures compared to pure water [43, 61, 160]. Next to this, only the battery pack has a defined heat capture ratio method as presented in Equation (3.51). For simplicity reasons, no additional methodologies are applied to determine the HCRs of the other components. Therefore, a fixed heat capture ratio of 10 % is applied to those components for non-cruise conditions. However, in the first cruise segment (not the diversion cruise), a HCR of 100 % is used for all components except the battery pack. A battery pack HCR > 100 % is used in the first cruise segment to cool the battery down to a temperature of 25 °C. As it is assumed that the battery pack is cooled as well during charging on the ground, a fixed temperature of 15 °C is set at the start of all take-off conditions [50]. The general battery pack temperature profile used is shown in Section 5.2.2. A maximum battery pack temperature of 40 °C is used to prevent premature degrading and capacity fade [11]. Moreover, the PPU electric power usage impact on the total system weight is only assessed based on a reduction in payload, to maintain a constant flight mission range of 1713 km or 925 NM [20, 154], which is discussed in Section 5.3.
The resulting mid-term scenario electric power usage of the PPUs is compared with the target usage in Fig-

ure 5.3. It can be seen that the target powers are not reached at the take-off, climb, and at the diversion climb segments. Due to the imposed sizing constraints, presented in Section 4.2.1, the maximum cooling power ratio is reached at the first climb segment, while the maximum ram air mass flow is reached in the diversion climb. At take-off, the electric power is slightly reduced to improve the mathematical convergence procedure in the software, i.e., to make this system more robust when changing parameters.

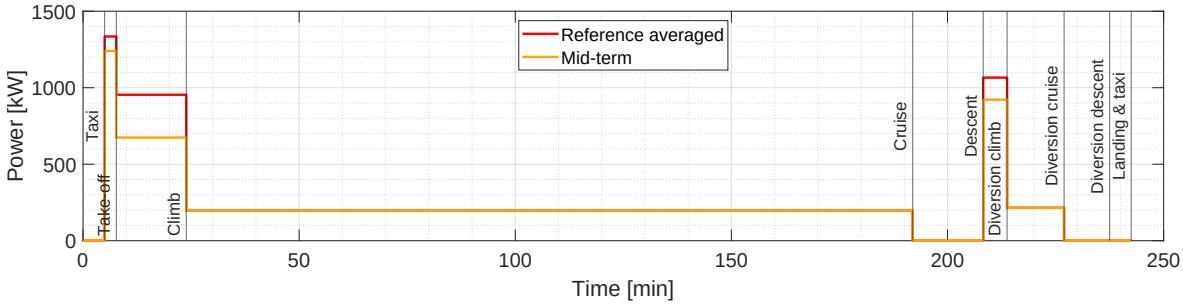

Figure 5.3: Mid-term scenario total electric power usage of the PPUs.

An optimised mid-term scenario is conducted in the attempt to further approach the target usage, at the costs of a less robust mathematical system convergence behaviour. The main difference with the standard mid-term scenario of Figure 5.3 is a 0.5 °C higher maximum battery temperature of 24.0 °C at take-off. The result of this mid-term (optimised) scenario is presented in Figure 5.4. It can be seen that the take-off power is approximated quite well. However, at the first climb segment the minimum chain efficiency is reached, which leaves a power deficit. Similarly, the maximum ram air flow is again reached at the diversion climb.

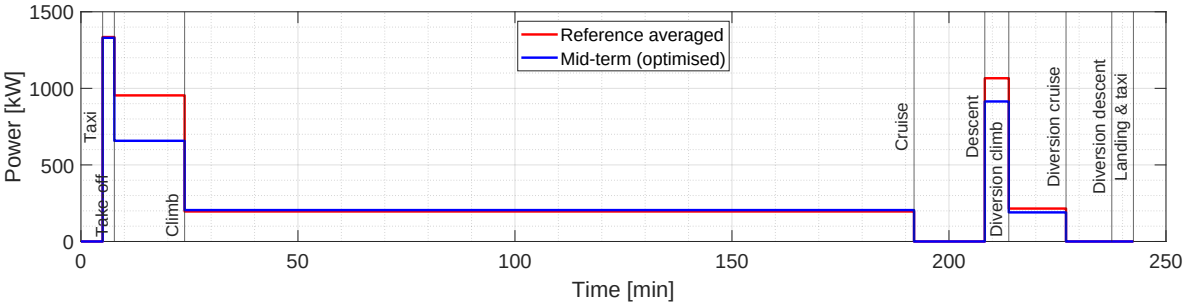

Figure 5.4: Mid-term (optimised) scenario total electric power usage of the PPUs.

A comparison between the near-term and the two mid-term scenarios is shown in Figure 5.5. It can be noticed that all three scenarios have a target power deficit at both climb segments, due to the fact that sizing limitations are reached. For the near-term scenario, even lower powers at the climb segments are present. This is caused by lower component efficiencies, which consequently require more cooling for the same required electric PPU power. Therefore, the sizing constraints are reached earlier. Furthermore, the power deficits imply that hybridisation should is reduced, at which more power is required from the gas turbine part to compensate for these deficits. This lessens the in-flight emission reduction potential compared to [20]. The power deficits for the near-term, mid-term, and mid-term (optimised) are at takeoff: 6.37 %, 7.12 %, and 0.375 %, at climb 50.7 %, 29.3 %, and 31.1 %, and at the diversion climb: 26.2 %, 13.5 %, and 14.2 % respectively.

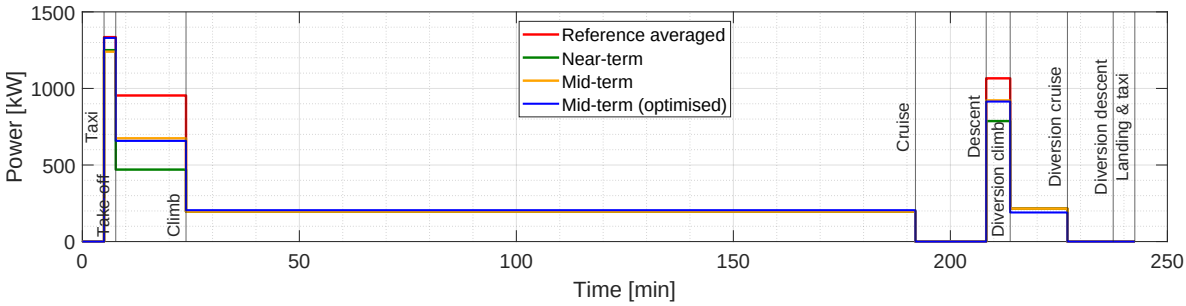

Figure 5.5: Comparison of the near-term, the mid-term, and mid-term (optimised) total electric power usage of the PPUs.

The system component technology level assumptions are summarised in Table 5.2. In case no corresponding value could be found, an interpolated design assumption (DA) is used. It can be seen that long-term system developments offer the potential to further improve the overall system efficiency while reducing its weight. Nevertheless, these projections are mostly based on cryogenic superconducting technology that require a cryogenic cooling system as well [81]. The component parameters that are kept constant for all scenarios are summarised in Appendix C.

Table 5.2: System component technology level assumptions.

Component	Parameter	Symbol	Near-term	Mid-term	Long-term	Source
Electric motor	Specific power [kW/kg]	SP_{EM}	6	13	16	[9], [158], [158]
	Power density [kW/m^3]	$\hat{\nu}_{EM}$	9300	25000	40000	[1], DA, [81]
	Maximum efficiency [%]	η_{EM}	95	96	98	[3], [158], [158]
Electric motor controller	Maximum efficiency [%]	η_{EMC}	95	97	99	DA, [161], [158]
Gearbox	Weight factor [-]	k_{GB}	34	26	26	[81], [81], [81]
Electric power converter	Specific power [kW/kg]	SP_{EM}	6.7	13	19	[161], DA, [158]
	Maximum efficiency [%]	η_{pc}	95	97	99	[161], DA, [158]
Battery pack	Specific energy [Wh/kg]	ϵ_{bat}	500	750	1200	[20], [20], [122]
	Energy density [Wh/l]	$\hat{\rho}_{bat}$	1000	1000	900	[2], [2], [122]
	Maximum efficiency [%]	η_{bat}	85	90	96	[20], [20], [11]
	Minimum state of charge [%]	SOC_{lim}	20	15	10	[20], DA, [11]

5.2. TRADE STUDIES

Three sets of results are presented in this section. They are all based on the mid-term component technology level assumptions and are sized with the hot day temperature profile (see Figure 3.9). The first set of results is the comparison between this study and the reference study [20] in Section 5.2.1. The second set of results analyses the impact of the maximum battery temperature at take-off on the system sizing characteristics, presented in Section 5.2.2. The third set of results presents the impact of lower atmospheric temperatures on the system performance in Section 5.2.3.

5.2.1. COMPARISON TO REFERENCE CASE

This study is based on the reference parallel HEA case study of [20], which did not include a coupled sized TMS. This comparison presents the main sizing characteristics to clarify what happens if the reference parallel HEA case study is taken as input and sized with a coupled TMS.

The mid-term (optimised) scenario, given in Figure 5.4, is used for this comparison as it comes the closest to the reference PPU electric power usage of [20]. The battery discharge voltage is given in Figure 5.6. It shows a steep decline in voltage at the take-off and the diversion climb segments. This corresponds to the typical dynamic behaviour of a Li-ion battery, which is mimicked to represent future battery cell technology.

[1] UQM. Powerphase HD 250. URL: https://wiki.neweagle.net/ProductDocumentation/EV_Software_and_Hardware/Electric_Motors/UQM/PowerPhase%20HD%20250%20web.pdf. Accessed on: 22/09/2020

[2] Sion Power. Products. URL: https://sionpower.com/products/. Accessed on: 22/09/2020

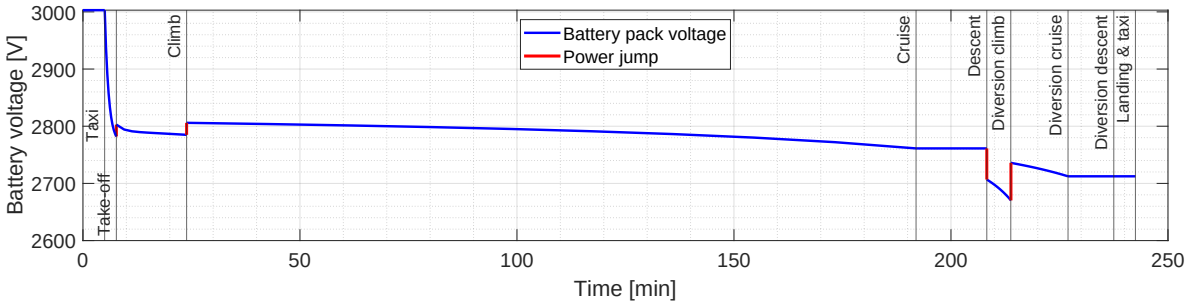

Figure 5.6: Battery pack discharge curve of the the mid-term (optimised) scenario.

A fairly constant behaviour can be noticed in the cruise segment. This agrees with the fact that lower electric power is demanded.

The battery SOC comparison with [20] is presented in Figure 5.7. The SOC curve of this study significantly differs from the reference cure at the first climb and cruise segments. A higher SOC decline for the reference curve in the climb segment can be noticed. The opposite happens in the cruise segment, where a higher decline is present for the mid-term (optimised) curve. This is caused by a lower electric power usage during the climb segment, while a slightly higher electric power usage can be observed during cruise, compared to the reference curve, see Figure 5.4. For the climb segment, the system sizing loop is converged at a cooling power ratio of 15 %, for a total PPU electric power usage of 657 kW. The final SOC of the mid-term (optimised) scenario is 20.3 %. If one wants to approach the reference SOC, a maximum cooling power ratio higher than 15 % should be applied in order to let the electric power usage of the PPU increase. This comparison shows that the battery SOC curves feature comparable discharge characteristics.

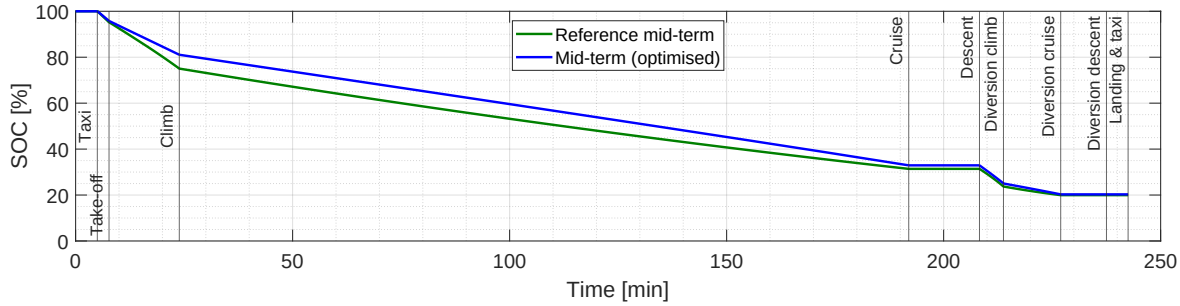

Figure 5.7: Battery state of charge comparison between the mid-term (optimised) scenario and the reference case.

The power distribution at the electric bus, the one connected to the battery pack, is given in Figure 5.8. It includes the corresponding transferred heat power at the air-to-liquid HEX. It is clear that both climb segments require the highest cooling power, of which the diversion climb is highest with 156 kW. The large difference between electric cooling and propulsion power at take-off is due to the fact that the battery pack is highly used as a heat sink, requiring less cooling power. This causes the battery pack temperature change rate to be 0.0560 K/s for take-off, while for the subsequent climb segment it is 0.0165 K/s, i.e. 3.4 times larger at take-off. Furthermore, the heat power transferred is the highest at cruise, while the cooling power is the lowest due to a sufficiently low atmospheric temperature, see Table 5.1. The only TMS component that needs electric power during cruise is the hydraulic pump. A coolant flow rate of 80 liter/min is required to transfer 105 kW of heat power during cruise.

A figure of merit that can be deduced from Figure 5.8, to see the normalised cooling power impact, is the ratio of maximum cooling power over the maximum take-off power of 4460 kW (the total PPU shaft power as presented in Table 4.3). This results in a percentage of 3.50 %. If only the maximum electric take-off power of 1330 kW is used, the percentage becomes 11.7 %. For the maximum cooling power, the fan itself consumes 0.761 kW, the compressor 150 kW, and the pump 0.101 kW. A difference of 5.14 kW is present between the sum of the usages of the individual components and the maximum cooling power of 156 kW, due to inefficiencies of intermediate components. The compressor accounts for 96 % of the maximum cooling power.

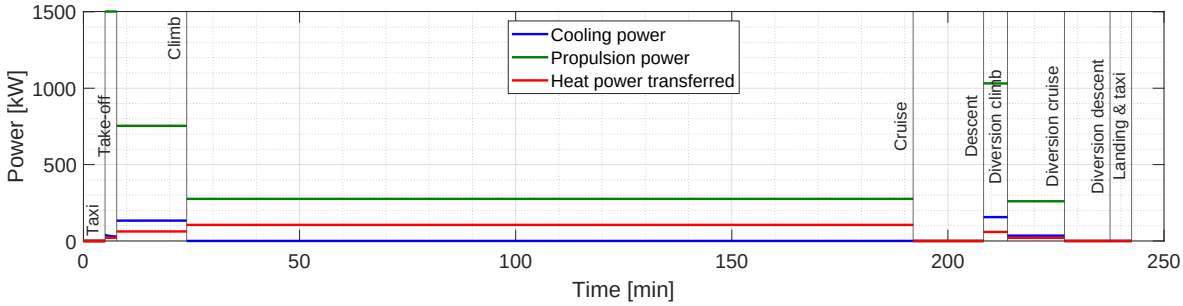

Figure 5.8: Power distribution for the mid-term (optimised) scenario, that includes cooling, propulsion, and heat transferred power.

The total ram drag coefficients in terms of drag counts (1 count = 0.0001 C_D) are presented in Figure 5.9. The values are rather an implicit indication of how much ram air is required by the cooling system than an actual quantitative insight, as a low fidelity model is used to capture the ram drag. The total ram drag coefficient, as presented in Equation (3.111), does not account for any drag reduction measures. The latter is however considered in [70], by making use of the so-called Meredith effect to offset the ducted radiator drag by providing positive net thrust from the exit ram air [8]. Nevertheless, the highest drag is attained during the diversion climb segment with a corresponding ram air flow of 10 kg/s. This results from approaching the target power, presented in Figure 5.4. The high total drag at the diversion climb is caused by the combination of a relatively high electric PPU power and a high atmospheric temperature. Consequently, the fan, compressor, and ACS are required to operate.

For this scenario, three sizing flight segments can be identified. First, the HEP components are sized according to the maximum electric PPU power at take-off. Second, the air-to-liquid HEX and the hydraulic pump are sized by the cruise segment. Thirds, the fan, compressor, and the ACS are sized by the diversion climb segment.

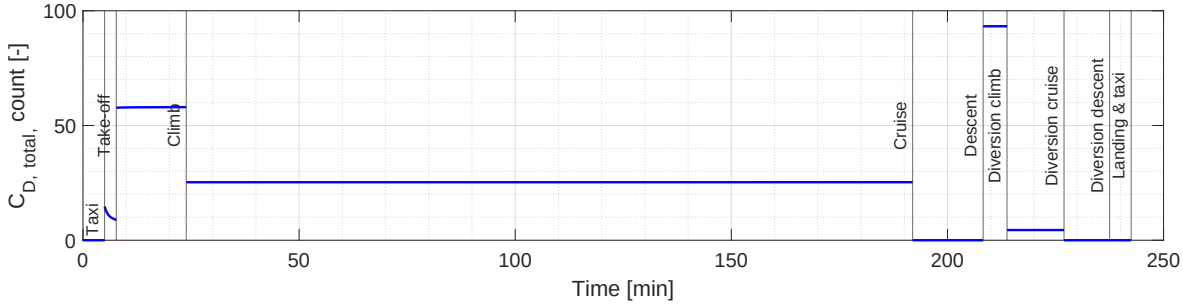

Figure 5.9: Total ram air drag counts for the mid-term (optimised) scenario.

The resulting chain efficiencies, as defined in Equation (3.1), are presented in Figure 5.10 and expressed in the text with [%]. The maximum value of 86.9 % is found at take-off, while for cruise a value of 74.3 % is found. It should be noted that at the diversion cruise a chain efficiency of 64.4 % is allowed to approach the SOC limit of 20 %.

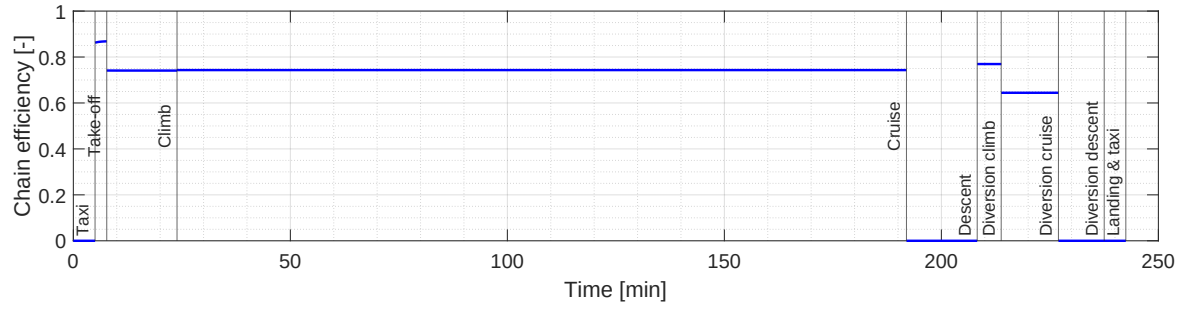

Figure 5.10: Chain efficiencies for the mid-term (optimised) scenario.

The resulting maximum combined specific power is presented in Table 5.3. It is compared to the near-term and standard mid-term scenarios. The highest CSP values result from the highest electric power extraction during take-off, according to Equation (3.2). Moreover, a significantly lower maximum CSP value is present for the near-term scenario due to a higher system weight, further discussed in Section 5.3.1. The mid-term scenarios are quite similar.

Table 5.3: Maximum combined specific power comparison for the near-term, mid-term and mid-term (optimised) scenarios.

Scenario	Maximum CSP
Near-term	0.273
Mid-term	0.415
Mid-term (optimised)	0.426

5.2.2. TAKE-OFF BATTERY TEMPERATURE IMPACT

The impact of a reduced maximum take-off battery temperature on the maximum electric PPU power at take-off is assessed based on the standard mid-term scenario, given in Figure 5.3. The battery pack temperature profiles considered are shown in Figures 5.11 and 5.12. The converged electric PPU power at take-off for the reduced maximum take-off temperature is presented in Figure 5.13. To clarify, the yellow line in Figure 5.11 is the general battery pack temperature profile used for the system sizing, except for the mid-term (optimised scenario) that uses a maximum take-off battery pack temperature of 24 °C, as described with Figure 5.4.

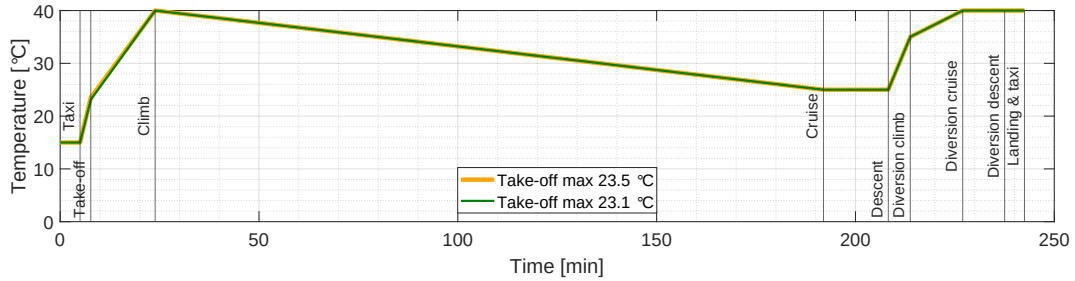

Figure 5.11: Battery temperature profiles for the mid-term scenario.

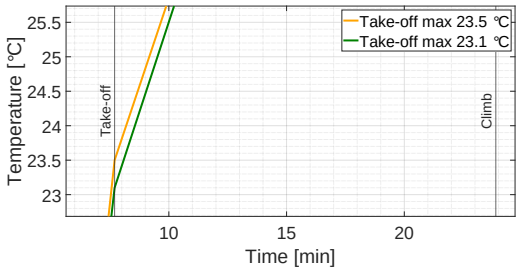

Figure 5.12: Battery temperature profiles, zoomed in, for the mid-term scenario.

The fairly small temperature reduction of 0.4 °C shows a reduced converged attainable take-off power of 1200 kW compared to 1240 kW, as can be seen in Figure 5.13. As the same system is used with the same flight mission characteristics, the subsequent flight segments have a similar electric PPU power usage. The final SOC is 22.9 % for the reduced maximum take-off temperature of 23.1 °C, compared to a final SOC of 22.3 % for the 23.5 °C temperature case. This is due to a lower energy extraction for the same battery size.

Furthermore, the maximum drag count at take-off for the 23.1 °C case is 6.44, to dissipate 18.8 kW of heat power with a ram air inlet mass flow of 0.604 kg/s. The ACS ratio of coolant air flow over pre-cooled air flow is 0.574 (see Air cycle system for clarification). For the 23.5 °C case, the maximum drag count of 62.2 results at take-off to dissipate a heat power of 25.5 kW with a corresponding ram air inlet mass flow of 3.49 kg/s. The corresponding ACS coolant air flow over pre-cooled air flow ratio is 1.788. The resulting ram air inlet

mass flows differ with a factor of 5.38 , for a heat power difference of 6.70 kW. When comparing the ACS air flow ratios, it can be noted that relatively more air is required to pre-cool the air for higher heat loads. This indicates a sensitive nonlinear response of the interacting TMS components.

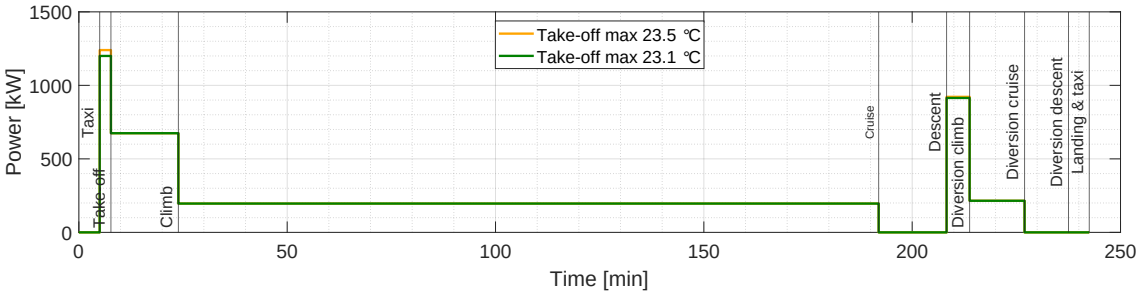

Figure 5.13: Electric power demands of the two maximum take-off battery temperatures for the mid-term scenario.

A higher allowable battery pack temperature during take-off allows for a higher possible electric PPU power at take-off. This phenomenon could contribute to the power shaving approach for the conventional gas turbine [20]. This means that the gas turbine could be less oversized to satisfy high powers at the take-off condition, allowing an improved design for the cruise segment. Moreover, the performance of electric motors is not affected by altitude while the efficiencies stay rather high at different power settings. On the contrary, it should be noted that the ram air drag is also increased with higher electric PPU power settings, which requires more thrust to compensate the drag. This causes an increase in fuel consumption for a given electric PPU power supply. If the aim is to reduce in-flight emissions, the contribution of both the power shaving aspect and the ram air drag aspect should give a net positive result in terms fuel consumption.

To reduce the ram air drag while keeping the same maximum battery take-off temperature, with corresponding electric power usage of the PPU, an increased battery cell specific heat capacity design could offer a solution [162]. For the same mid-term scenario (see Figure 5.3), the battery cell specific heat capacity is raised from 1200 J/kg/K to 1250 J/kg/K. The impact on the ram drag is presented in Figure 5.14. A significant reduction results at both climb segments, due to the fact that the battery can absorb more heat loss and it can therefore lower the cooling burden.

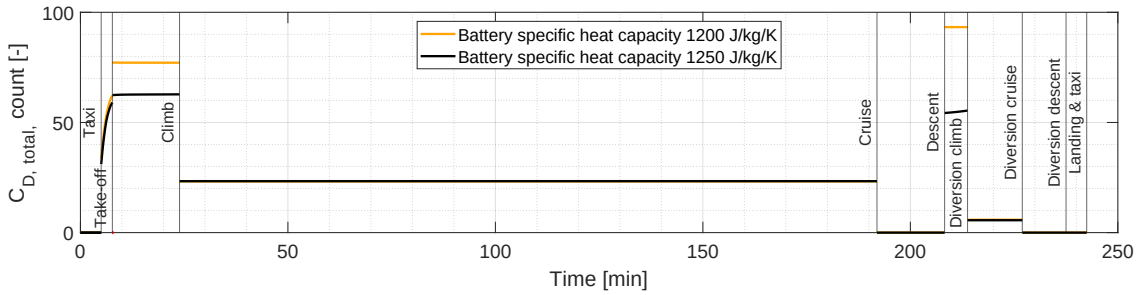

Figure 5.14: Total ram air drag counts for the mid-term scenario and the mid-term (higher cell specific heat capacity) scenario.

Another effect of a higher cell specific heat capacity is that the battery sizing power can be reduced to lower the battery weight, while keeping the same electric power output as required. A direct effect is that less energy is present in the battery pack. For the same electric power usage, the final SOC is therefore slightly less as can be seen in Figure 5.15. The topic of battery sizing powers is discussed in Weight impact of Section 5.3. Furthermore, a maximum chain efficiency increase from 77.2 % to 79.5 % results at the diversion climb segment.

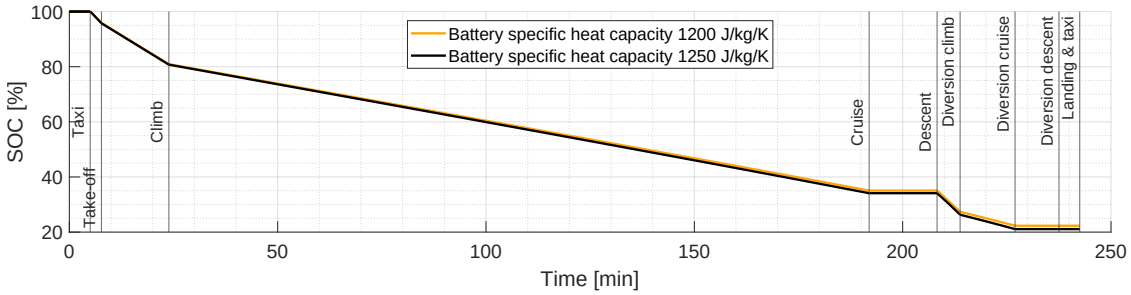

Figure 5.15: Battery state of charge comparison between the mid-term scenario and the mid-term (higher cell specific heat capacity) scenario.

5.2.3. ATMOSPHERIC TEMPERATURE IMPACT

The effect of different atmospheric temperature profiles on the performance of the mid-term scenario sized system (see, Figure 5.3) is discussed in this section. The temperature profiles considered are presented in Figure 3.9. The electric PPU power usage for the three temperature profile cases is the same, which is the mid-term scenario as presented in Figure 5.3. The highest temperature profile is given by the blue curves (hot day), the yellow curves represent a reduced temperature profile compared to the hot day (tropical day), and the standard ISA day profile features the lowest temperatures in green.

The battery pack voltage curves are given in Figure 5.16. The voltage differences grow with time, where the largest differences can be seen at the end of the flight mission. The corresponding voltages reached at the landing are 2721 V, 2736 V, and 2744 V for the hot day, tropical day, and standard ISA day respectively. The maximum end voltage difference between the hot day and ISA standard day is 23 V, which is 0.77 % of the full voltage of 3000 V.

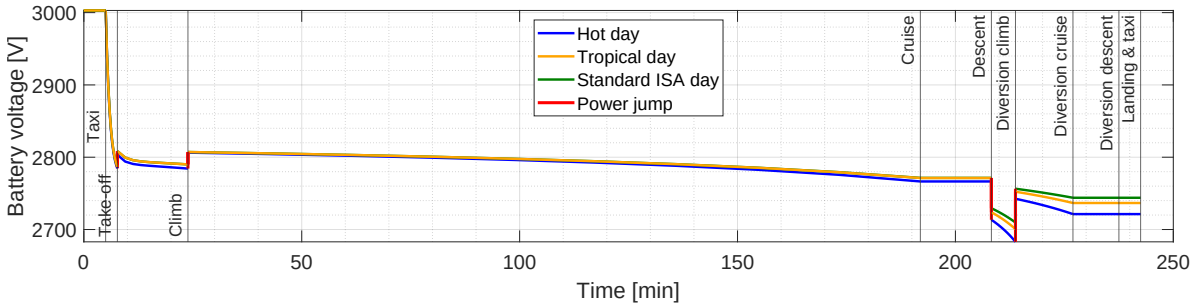

Figure 5.16: Comparison of battery discharge curves of the the mid-term scenario for three different atmospheric temperature profiles.

The impact on the SOC curves is shown in Figure 5.17. This implicitly shows that higher atmospheric temperatures require more cooling. This results in a lower SOC at the end of the flight mission, as more cooling power is required throughout the mission. The final SOC values are 22.3 %, 25.6 %, and 27.0 % for the hot day, tropical day, and standard ISA day respectively.

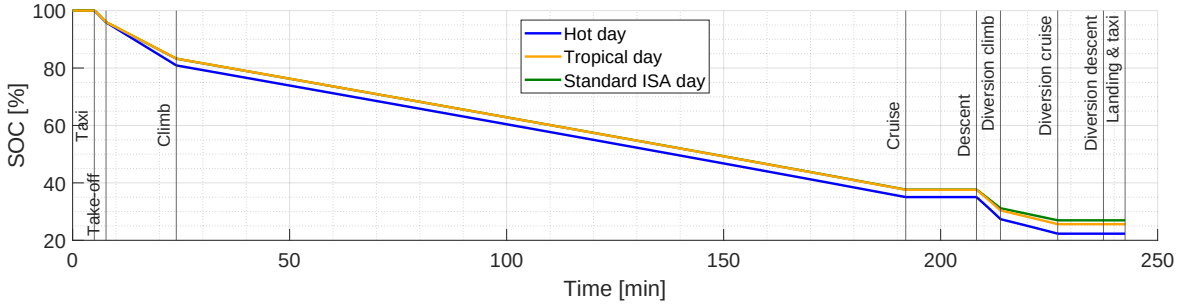

Figure 5.17: Battery state of charge comparison of the the mid-term scenario for three different atmospheric temperature profiles.

The total ram air drag count curves are given in Figure 5.18. It consistently shows that higher atmospheric

temperature profiles induce higher values for the total drag coefficient and therefore require more ram air cooling. The different curve shapes at the take-off condition are caused by the nonlinear behaviour of the coupled compressor and the ACS. During the first climb segment, the hot day case requires the usage of the compressor and the ACS, to pre-cool the air. This is not required for the other two cases, as the ambient temperature is sufficiently low. This explains the large difference in drag counts during climb. The same holds for the diversion climb, except that the tropical day case uses the coupled compressor and ACS as well.

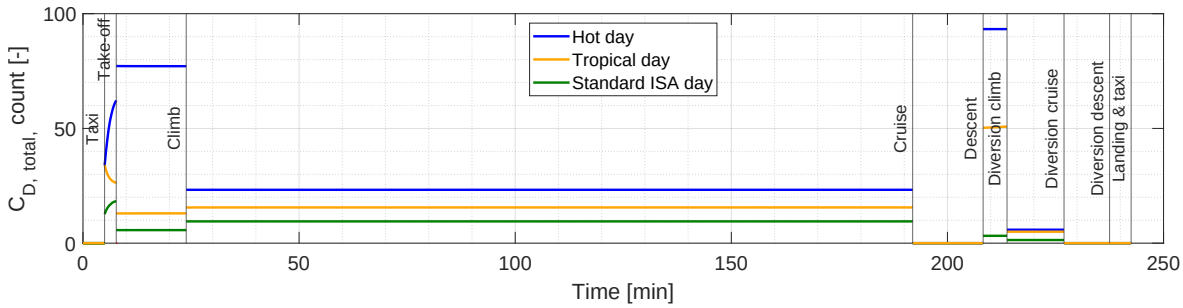

Figure 5.18: Total ram air drag counts of the mid-term scenario for three different atmospheric temperature profiles.

Still, a large difference can be noted between the hot day case and the tropical day case at the diversion climb. Overall, if the system can be cooled purely on ram air, then a higher chain efficiency results, as can be seen in Figure 5.19. The minor difference in chain efficiency if purely ram air is used, for example during cruise, is caused by a slightly higher electric power demand of the pneumatic pump for higher temperatures.

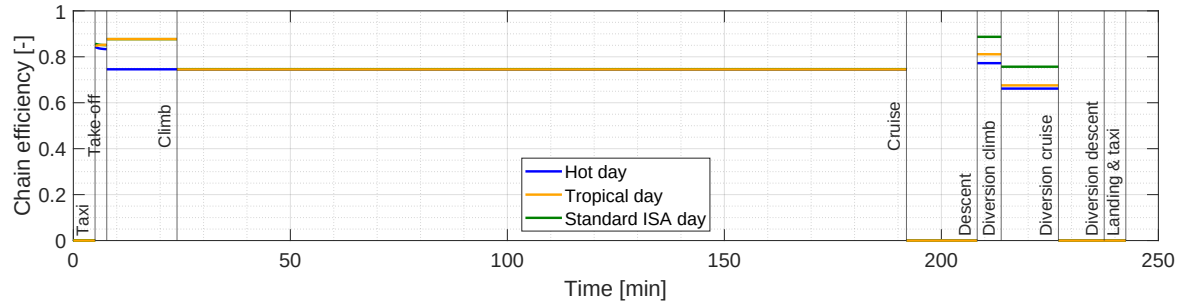

Figure 5.19: Chain efficiencies of the mid-term scenario for three different atmospheric temperature profiles.

5.3. WEIGHT AND VOLUME IMPACT

The weight and volume impact of the near-term, mid-term, and the mid-term (optimised) scenarios are discussed in Section 5.3.1 and in Section 5.3.2 respectively. The actual volumetric system impact inside the simplified ATR72-600 model is presented as well, for the mid-term (optimised) scenario in Figure 5.22. In the weight and volume pie charts of Figures 5.20 and 5.21, values of 0 % (zero) have actually a value lower than 0.5 % and are therefore rounded to 0 %. Values for pneumatic ducts and hydraulic pipes are omitted due to high uncertainty in their design and routing approach. The weight and volume of the control valves are not taken into account as they are assumed to have a very small contribution. However, the volumes of the control valves are displayed in the volumetric impact views to comply with the routing routine of SysArc. Furthermore, the system dry weight is considered, meaning that no liquid coolant weight is included.

5.3.1. WEIGHT IMPACT

The system weight distributions for the near-term, mid-term, and mid-term (optimised) scenarios are given in Figure 5.20. The near-term case has the highest system weight of 5640 kg. This corresponds to 75.2 % usage of the design payload of 7500 kg, presented in Table 4.3. For the mid-term case, the system weight of 3490 kg corresponds to a 46.5 % usage of the design payload. The mid-term (optimised) case has a slightly higher design payload usage of 46.9 %, due to a larger sized system as a result of the higher take-off power (see Figure 5.5). The electric cable weight results from a total length of 62.1 m for all scenarios.

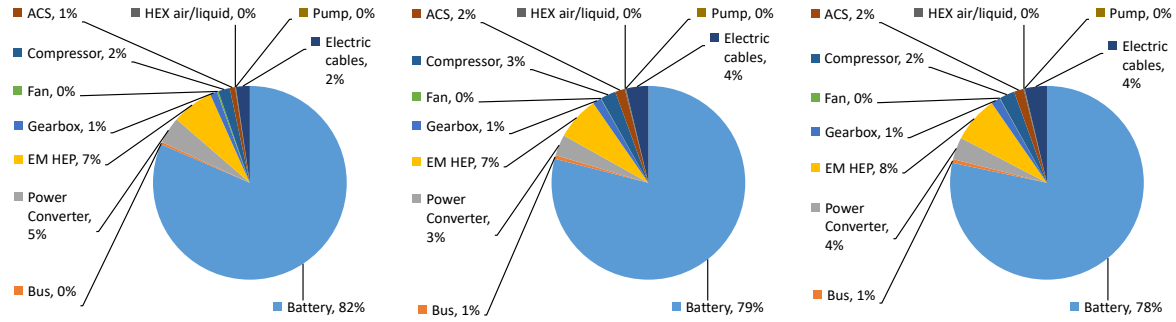

(a) Near-term system weight = 5640 kg. Payload usage = 75.2 %.

(b) Mid-term system weight = 3490 kg. Payload usage = 46.5 %.

(c) Mid-term (optimised) system weight = 3520 kg. Payload usage = 46.9 %.

Figure 5.20: System weight impact for the parallel HEA, with a MTOW = 25,600 kg and a design payload = 7500 kg.

As the battery weight is the same for the mid-term and mid-term (optimised) scenarios, the increase in system weight is mainly driven by the weight increase of the electric motors of 18.0 kg (from 253 kg to 271 kg) and the weight increase of the power converters of 8.0 kg (from 123 kg to 131 kg).

The additional battery pack weights and corresponding percentage changes for the three cases, to account for a liquid cooled TMS, are given in Table 5.4. The battery pack weight of 2049 kg is used as reference value from the parallel-hybrid case study of [20]. For the near-term scenario, a significant increase of 125 % is found. In combination with a design payload usage of 75.2 %, the near-term scenario is deemed to be not feasible. However, for both mid-term scenarios, an increase of battery weight of 34.5 % is found to compensate for the liquid cooled TMS, even with PPU power deficits at both climb segments (see Figure 5.5).

Table 5.4: Battery pack weight changes, reference battery pack weight = 2049 kg [20].

Parameter	Near-term	Mid-term scenarios
Battery weight [kg]	4600	2756
Δ_{weight} [kg]	+2551	+707
Weight change [%]	+125	+34.5

The battery pack characteristics are further discussed with the three aforementioned cases and with the mid-term (1250 J/kg/K) scenario from Figure 5.14, that has a higher cell specific heat capacity. The identified apparent oversizing of the battery pack, along with the total number of cells is presented in Table 5.5.

Table 5.5: Battery pack sizing characteristics.

Parameter	Near-term	Mid-term	Mid-term (optimised)	Mid-term (1250 J/kg/K)
Total cells [-]	155,155	139,425	139,425	134,420
Cells in parallel [-]	217	195	195	188
Cells in series [-]	715	715	715	715
P_{sizing} [kW]	2165	2030	2030	1955
P_{sizing} / $P_{\text{produced, max}}$ [-]	1.16	1.23	1.17	1.19
P_{sizing} / $P_{\text{required, max}}$ [-]	1.38	1.38	1.32	1.33

This oversizing is presented by two ratios. The first one is given by the battery sizing power P_{sizing} over the maximum produced power $P_{\text{produced, max}}$, which includes its own produced heat loss power. The second one is the battery sizing power over the maximum required electric output power $P_{\text{required, max}}$. If the ratios are greater than unity, it means that the battery is oversized in terms of power requirement. The ratio values for all scenarios are greater than unity, as can be seen in Table 5.5. As the battery pack is also used as a heat sink, the resulting battery weight and therefore number of cells should have a sufficient thermal capacity to be able to cope with a certain battery temperature increase. It can be seen that the mid-term (optimised) scenario has the lowest ratio values of the mid-term scenarios. Due to nonconvergence of the mathematical system in

the software, a lower battery sizing power for the mid-term (optimised) could not be achieved. Therefore, a correction factor of 1.32 (P_{sizing} / $P_{\text{required, max}}$) results for the mid-term (optimised) scenario, to account for additional thermal capacity and inefficiencies of the battery pack.

Overall, the battery pack contributes the most to the system weight for all three cases, as can be seen in Figure 5.20. The second most contributing components are the electric motors. It should be noted that first order weight and volume estimations are used. Weight and volume estimations for the fan, ACM, pump, power converter, and cold plate are based on non-aeronautical data. Due to higher safety margins in non-aeronautical applications, a weight and volume reduction could be achieved if purely aeronautical data is used.

5.3.2. VOLUME IMPACT

The system volume distributions for the near-term, mid-term, and mid-term (optimised) scenarios are given in Figure 5.21. The near-term case has the highest system volume of 4.00 m^3, compared to 3.48 m^3 and 3.51 m^3 for the mid-term and mid-term (optimised) cases respectively. The battery pack contributes the most in all cases, while the electric motors come second. This relation has also been found in the weight distributions of Figure 5.20.

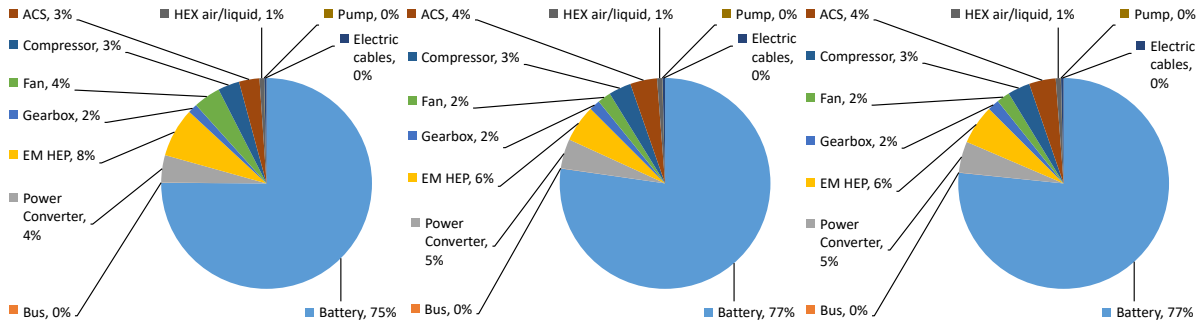

(a) Near-term system volume = 4.00 m^3. Baggage volume usage = 40.9 %.

(b) Mid-term system volume = 3.48 m^3. Baggage volume usage = 35.6 %.

(c) Mid-term (optimised) system volume = 3.51 m^3. Baggage volume usage = 35.9 %.

Figure 5.21: System volume impact for the parallel HEA, with a total baggage volume = 9.78 m^3.

The overall reduction in weight and volume for two the mid-term cases results from two causes. First, it is due to the direct effect of higher specific powers and power density. Second, it is due to the cascade effect caused by higher efficiencies. This allows for lower upstream sizing powers, which results in lower heat power losses and in lower component weight and volume.

By taking the ratio of the weight percentage contribution ($m_{\%}$) over the volume percentage contribution ($m_{\%}$), it can be shown whether a component has a higher system weight impact ($m_{\%}/v_{\%} > 1$) or a higher volume impact ($m_{\%}/v_{\%} < 1$) respectively. The resulting component $m_{\%}/v_{\%}$ values are presented in Table 5.6. Components with a $m_{\%}/v_{\%} < 1$ are marked in bold. For the mid-term (optimised) case, the three components with the highest relative impact on the system volume are the fan, HEX, and the ACS. Similarly, the three components with the highest relative impact on the system weight are the electric bus, electric cables, and the electric motor. Furthermore, the resulting battery pack density for the mid-term (optimised) case is 1030 kg/m^3, presented in Table 5.6. The overall system density is 1000 kg/m^3. Comparing the system weight relative to the MTOW results in a value of 0.138.

Table 5.6: System weight and volume comparison characteristics.

Component level		Near-term	Mid-term	Mid-term (optimised)
Battery pack m/v	[kg/m^3]	1530	1030	1030
Battery pack $m_{\%}/v_{\%}$	[-]	1.09	1.03	1.01
Electric bus $m_{\%}/v_{\%}$	[-]	12.7	17.9	17.9
Power converter $m_{\%}/v_{\%}$	[-]	1.25	**0.600**	**0.800**
Electric motor HEP $m_{\%}/v_{\%}$	[-]	**0.875**	1.17	1.33
Gearbox $m_{\%}/v_{\%}$	[-]	**0.500**	**0.500**	**0.500**
Fan $m_{\%}/v_{\%}$	[-]	**0.063**	**0.028**	**0.028**
Compressor $m_{\%}/v_{\%}$	[-]	**0.667**	1.00	**0.667**
ACS $m_{\%}/v_{\%}$	[-]	**0.333**	**0.500**	**0.500**
HEX (air-to-liquid) $m_{\%}/v_{\%}$	[-]	**0.127**	**0.179**	**0.179**
Pump $m_{\%}/v_{\%}$	[-]	**0.850**	1.19	1.19
Electric cables $m_{\%}/v_{\%}$	[-]	5.89	9.56	9.56
System level		Near-term	Mid-term	Mid-term (optimised)
$m_{\text{system}}/v_{\text{system}}$	[kg/m^3]	1410	1000	1000
m_{system}/MTOW	[-]	0.220	0.136	0.138

As the parallel HEP makes use of two energy sources, more components need to be placed inside the aircraft. For a given volume, this implies less available payload space. Moreover, a maintenance approach should be developed in order to prevent leakage and to consider replacement possibilities for all components. Installation penalties, such as a construction framework, are inevitable. This further increases the system weight. The number of maintenance doors at the fuselage for example could potentially increase the structural weight even more. Additionally, the placement of the components should also consider the static stability of the aircraft. A visual impression of the volumetric component impact of the mid-term (optimised) scenario is presented in Figure 5.22, with a cabin floor thickness of 0.13 m [163].

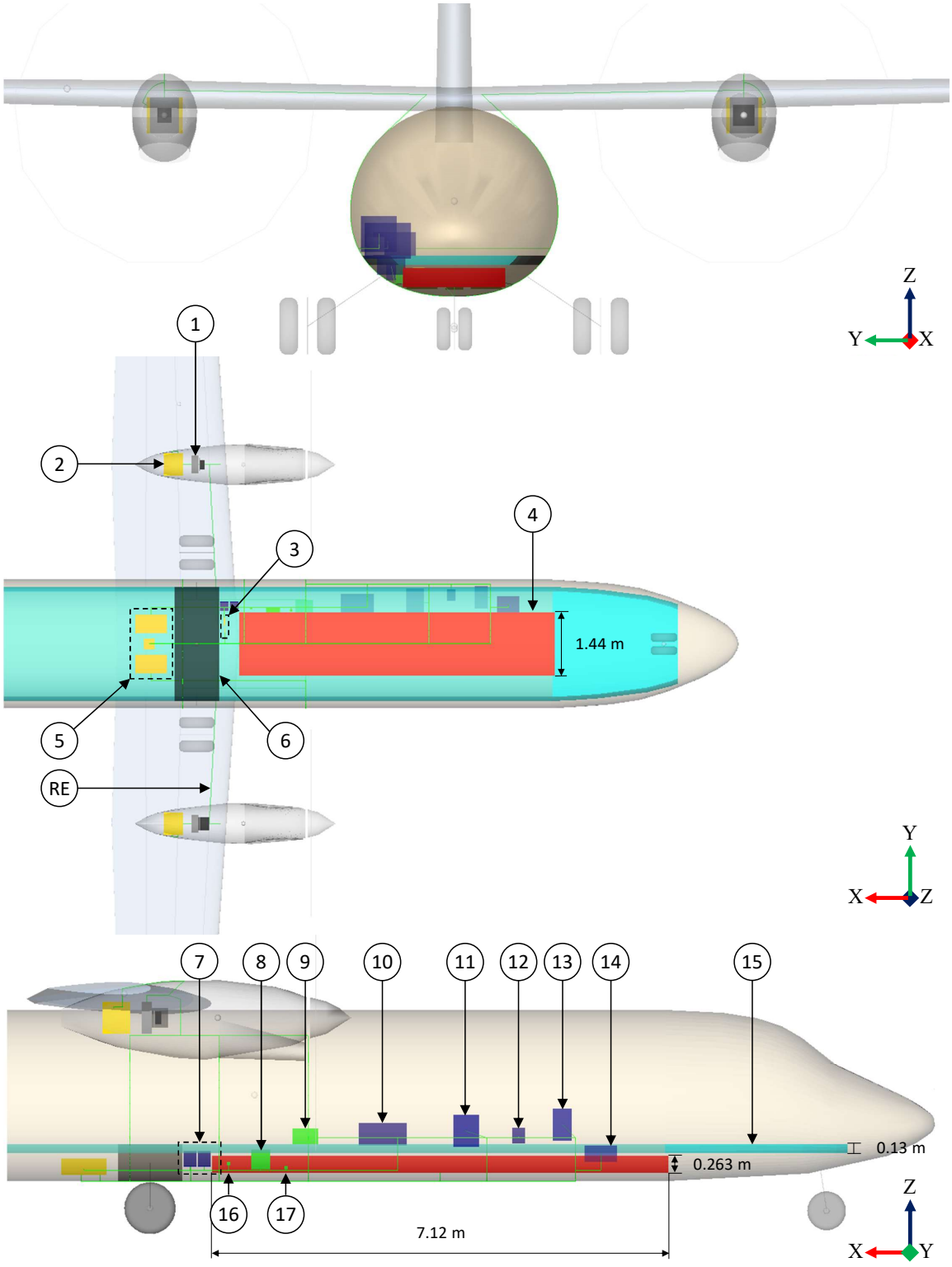

1	Gearbox	5	Power converter	9	HEX	13	Fan	17	Reservoir
2	Electric motor	6	Landing gear bay	10	ACS	14	Ram air inlet	RE	Routing element
3	Electric bus	7	Ram air outlet	11	Compressor	15	Cabin floor		
4	Battery pack	8	Hydraulic pump	12	Control valve	16	Control valve		

Figure 5.22: Volumetric component impact of the mid-term (optimised) scenario. Component colour blue: pneumatic, yellow: electric, green: hydraulic, and red: the battery pack.

6

CONCLUSIONS & RECOMMENDATIONS

6.1. CONCLUSIONS

The objective of this thesis is to identify the impact of a thermal management system on the power, weight, and volume usage, for a given reference case of a parallel-hybrid electric ATR72-600 regional aircraft, that excluded the sizing of a cooling system. For this purpose, a sizing methodology was developed in this thesis that couples the sizing of the electric part of the parallel-hybrid electric powertrain with the sizing of a closed-loop liquid cooled thermal management system. An air cycle system is used as part of the thermal management system to pre-cool ambient air if required. Furthermore, both the electric part of the powertrain and the cooling system use electric power from the same battery. The term "system" is used to define the electric part of the parallel-hybrid electric powertrain and the thermal management system components together. The system is sized for hot day conditions. Gas turbine sizing is not included.

It can be concluded that for the reference parallel-hybrid electric regional aircraft, with a MTOW of 25,600 kg, it is not feasible to fly the reference hybrid electric flight mission with a design that uses near-term component technology level assumptions for the year 2025. This assumes a constant flight mission range of 1713 km and a system design payload of 7500 kg, taken from the reference case study. The concluded infeasibility is based on a required payload usage of 75.2 %, to integrate the thermally-controlled electric propulsion system. A battery weight of 4600 kg results, which is an increase of 125 %. The derived system weight over MTOW is 22 %. Furthermore, the system volume impact of this scenario is 4 m^3, which is equivalent to 40.9 % usage of the available baggage volume of 9.78 m^3. On top of this, electric propulsion power deficits are present at take-off of 6.37 %, at climb of 50.7 %, and at the diversion climb of 26.2 % compared to the reference case. The power deficits result from reaching imposed sizing constraints.

However, if instead mid-term component technology level assumptions are used for the year 2035, the feasibility potential increases. A payload usage of 46.9 % results for this scenario. The battery weight of 2760 kg implies an increase of 34.5 % compared to the reference case. The corresponding system weight over MTOW is 13.8 %. The resulting system volume of 3.51 m^3 uses 35.9 % of the baggage volume. Nevertheless, electric propulsion power deficits are still present at the take-off of 0.375 %, at climb of 31.1 %, and at the diversion climb of 14.2 % relative to the reference case. As the mid-term technology scenario offers a higher feasibility potential than the near-term scenario, the mid-term scenario is assessed in more depth.

The battery is identified to be the most critical component for both the near-term and mid-term scenarios. For the mid-term scenario, the battery accounts for 78 % of the system weight of 3520 kg, compared to a 77 % contribution to the system volume. The second most critical component in terms of weight and volume is the electric motor in the powertrain, with a contribution of 8 % and 6 % respectively. The significant impact of the battery on the system weight and volume is due to the fact that the battery supplies electric power to both the propulsion and the thermal management system. This design initiates a sizing loop, which is driven by three main mechanisms. First, if more electric propulsion power is required, the battery size has to increase to comply with that power demand. Second, inefficiencies at the powertrain components cause excessive heat losses that have to be dissipated by the thermal management system. Additional electric power is re-

quired from the battery, which causes the battery size to increase again. Moreover, the inefficiencies at the battery itself grow with higher power demands, which further increases the total heat loss that needs to be dissipated. This second mechanism causes the battery to be larger than expected, when only considering the propulsion power requirements. The third and more implicit mechanism that causes the battery size to grow is identified to be the thermal capacity of the battery. Part of the battery heat loss can be absorbed by the battery itself to steadily increase its temperature. This lowers the burden on the thermal management system. The battery thermal capacity should be sufficient enough to comply with a feasible battery temperature change rate when electric power is required. An equilibrium must be found between the total extracted battery power and the allowed temperature change as a function of the thermal capacity. If no convergence can be acquired, the battery size is again increased in the attempt to make the system converge. This further increases the attainable maximum output power and the thermal capacity at the cost of increased weight and volume. If still no convergence can be found, taking into account the sizing constraints, the reference electric propulsion power is reduced to reach convergence. This explains the discussed power deficits. For a fixed total shaft power, the gas turbine should provide more power to compensate it. This reduces the potential to mitigate in-flight emissions.

Although the highest electric propulsion power usage occurs at take-off, the maximum required cooling power of 156 kW occurs at the diversion climb for the mid-term scenario. This is due to the high usage of the battery as a heat sink at take-off. The electric propulsion power at the diversion climb is 914 kW. The required maximum cooling power over the maximum total take-off shaft power (4460 kW) is 3.5 %. If only the maximum electric take-off shaft power (1330 kW) is used, 11.7 % results. The ram air electric compressor, which operates in combination with the air cycle system, uses 96 % of the maximum cooling power and is therefore concluded to be the most critical thermal management system component in terms of power usage. The ram air fan and the liquid coolant pump use less than 1 % of the maximum cooling power. Therefore, the compressor offers highest the potential to reduce the cooling power consumption.

The actual power that is used to size the battery is higher, due to the discussed three mechanisms, than the maximum required battery output power. A ratio of required battery sizing power over the maximum required battery output power is defined, that accounts for the propulsion power, cooling power, a sufficient battery thermal capacity, and all inefficiencies. The ratio found for the mid-term scenario is 1.32.

A possibility to reduce the required cooling power is to opt for a battery design that has a higher heat capacity for the same performance. It allows the battery to absorb more heat and it can therefore also lower the required ram air flow. Furthermore, it is found that this allows for a lower battery sizing power for the same the same electric power output.

For a sized system, it is found that a lower maximum battery temperature at take-off, i.e. a lower battery temperature change rate, forces the system to converge at a lower electric propulsion power at take-off. At the same time, the ram air required reduces. However, the air cycle system ratio of coolant air flow over precooled air flow does not remain constant, which indicates a nonlinear response of the interacting thermal management system components.

As the system is sized for a hot day atmospheric temperature profile, lower atmospheric temperatures should lower the required power consumption of the thermal management system. This is due to the fact that ram air is used as the heat sink for the liquid cooling system. Lower ambient temperatures imply lower required ram air flows to dissipate the same heat. This relation is found by the presence of higher battery state of charge values if lower atmospheric temperature profiles are used, which implies less battery power usage.

The system components are visualised inside a simplified aircraft model to see its volumetric impact. This reveals the limited space available to place the components, not even considering the impact on the static stability of the aircraft due to the system weight. Furthermore, it amplifies the need for construction frameworks to allow maintenance to prevent e.g. leakage, which increases the structural weight of the aircraft.

In conclusion, the significant impact of a thermal management system on power, weight, and volume usage can not be neglected nor underestimated in the conceptual design phase of future hybrid electric regional aircraft studies.

6.2. LIMITATIONS AND RECOMMENDATIONS

In this study, several assumptions and simplifications have been made to limit the scope of this thesis. The corresponding limitations result in the following recommendations that can be used to improve the assessment of hybrid electric aircraft studies:

- **Model the ram air system more adequately to perform more reliable drag coefficient estimations in order to estimate additional fuel consumption.** It is found that the ram air required to dissipate the heat away from the aircraft is a limiting factor in the sizing process. This indicates that for a given electric propulsion power supply, the impact of ram air drag is likely to increase the fuel consumption, which is not included in this study. The coupling of a more reliable ram drag estimation model with corresponding fuel consumption calculations contributes to a broader understanding of what the actual impact of a TMS will be.

- **Integrate heat capture ratio methods for critical components, e.g. the electric motor, to more accurately predict the required heat load that needs to be dissipated.** In this study, only a dedicated heat capture ratio method is implemented for the battery pack, where constant heat capture ratio values are imposed for the other components to capture a first order estimation.

- **Model the component volumetric representation and placement inside the aircraft with more detail to reveal bottlenecks.** By applying more constraints on where components can be placed and taking into account installation regulations, a more realistic volumetric impact can be obtained. In this study, a centralised TMS is used. To improve redundancy, a second TMS should be present, one for each powertrain. This doubles the number of TMS components and makes it more critical to fit these components inside the aircraft. By taking into account the one engine inoperative condition, the system size grows even more. This requires to model components with more detail than just a box shape. Furthermore, no routing elements are present in the volumetric impression. This should also be taken into account to sketch an improved volumetric impact. As the battery pack takes up the most weight and volume, distributing battery modules over different places in the aircraft could prevent instability and available space related issues.

- **Implement a computational optimisation strategy to find an improved control strategy for a given point performance condition.** As the results are generated by manually changing the control parameters, it is assumed that conservative results have been found. Due to the non-linear behaviour of the TMS, an assisting optimiser could contribute to a lower TMS impact by changing the control parameters of the TMS components for a given objective.

- **Develop a closed-loop feedback sizing approach to close the gap between the sizing at aircraft performance level and at system level.** This study only takes a reference case as input that did not include the sizing of a TMS. The computed impact, i.e. the output of this study is not again processed. These output results can be used to re-evaluate the used input to improve reliability of the overall aircraft sizing approach. An improved estimation of the gas turbine and the battery size can be made due to the possibility of re-evaluation of the initial hybridisation strategy.

- **Integrate other aircraft subsystems into the analysis that can use generated waste heat as input to improve the overall efficiency.** By using a holistic design approach, generated waste heat can e.g., be used as input for the de-icing system, as input for the environmental control system to heat up the cabin if required or to be used in galley systems. This will lower the required ram air flow by taking advantage of the possible synergy between systems.

- **Conduct a comparison study to see the impact of using a vapour cycle system cooling approach.** As the vapour cycle system cooling approach offers higher efficiencies compared to a liquid cooling approach, an interesting comparison study can be performed.

- **Explore in-flight battery charging possibilities to recover part of the aircraft potential energy.** By making use of the so-called windmilling effect, a potential increase in hybridisation rate or a reduction in terms of the turn around time at the airport, due to reduced charging time, can be assessed. In this study, only discharging is taken into account.

BIBLIOGRAPHY

[1] European Commission, *Flightpath 2050 Europe's Vision for Aviation*, Tech. Rep. (European Union, Luxembourg, 2011).

[2] Airbus, *Global Networks, Global Citizens 2018-2037,* (2018).

[3] EcoAct, *Carbon offsetting and reduction scheme for international aviation (CORSIA),* (2017).

[4] J. D. Scheelhaase, *How to regulate aviation's full climate impact as intended by the EU council from 2020 onwards,* Journal of Air Transport Management **75**, 68 (2020).

[5] ACARE, *Strategic Reseach & Innovation Agenda, 2017 Update, Volume 1*, Tech. Rep. (Advisory Council for Aviation Research and Innovation in Europe, Brussel, Belgium, 2017).

[6] K. L. Suder, *Overview of the NASA Environmentally Responsible Aviation Project's Propulsion Technology Portfolio,* in *48th AIAA/ASME/SAE/ASEE Joint Propulsion Conference*, July (American Institute of Aeronautics and Astronautics, Atlanta, Georgia, 2012) p. 23.

[7] S. Clarke, *Aircraft Electric Propulsion Systems: Applied Research at NASA,* (2015).

[8] J. Freeman, P. Osterkamp, M. Green, A. Gibson, and B. Schiltgen, *Challenges and opportunities for electric aircraft thermal management,* Aircraft Engineering and Aerospace Technology **86**, 519 (2014).

[9] S. Sahoo, X. Zhao, and K. Kyprianidis, *A review of concepts, benefits, and challenges for future electrical propulsion-based aircraft,* Aerospace **7**, 69 (2020).

[10] B. T. Schiltgen and J. Freeman, *Aeropropulsive Interaction and Thermal System Integration within the ECO-150: A Turboelectric Distributed Propulsion Airliner with Conventional Electric Machines,* , 1 (2016).

[11] M. Macdonald, J. Rheaume, Y. Khakpour, and C. Lents, *Transient Cooling Approach for a Mhr Class Hybrid Electric Propulsion System Battery Pack,* in *AIAA SciTech 2020 Forum*, January (Orlando, Florida, 2020) pp. 1–7.

[12] K. R. Antcliff, M. D. Guynn, T. V. Marien, D. P. Wells, S. J. Schneider, and M. T. Tong, *Mission analysis and aircraft sizing of a hybrid-electric regional aircraft,* 54th AIAA Aerospace Sciences Meeting **0**, 1 (2016).

[13] M. Voskuijl, J. van Bogaert, and A. G. Rao, *Analysis and design of hybrid electric regional turboprop aircraft,* CEAS Aeronautical Journal **9**, 15 (2017).

[14] C. Pornet and A. T. Isikveren, *Conceptual design of hybrid-electric transport aircraft,* Progress in Aerospace Sciences **79**, 114 (2015).

[15] J. Hoelzen, Y. Liu, B. Bensmann, C. Winnefeld, A. Elham, J. Friedrichs, and R. Hanke-rauschenbach, *Conceptual Design of Operation Strategies for Hybrid Electric Aircraft,* Energies **11**, 1 (2018).

[16] K. R. Antcliff and F. M. Capristan, *Conceptual Design of the Parallel Electric-Gas Architecture with Synergistic Utilization Scheme (PEGASUS) Concept,* in *18th AIAA/ISSMO Multidisciplinary Analysis and Optimization Conference, AIAA AVIATION Forum*, June (American Institute of Aeronautics and Astronautics, Denver, Colorado, 2017) p. 15.

[17] J. Zamboni, R. Vos, M. Emeneth, and A. Schneegans, *A Method for the Conceptual Design of Hybrid Electric Aircraft,* in *AIAA Scitech 2019 Forum*, January (American Institute of Aeronautics and Astronautics, San Diego, California, 2019) p. 24.

[18] M. Strack, G. P. Chiozzotto, M. Iwanizki, M. Plohr, and M. Kuhn, *Conceptual Design Assessment of Advanced Hybrid Electric Turboprop Aircraft Configurations,* in *17th AIAA Aviation Technology, Integration, and Operations Conference*, June (American Institute of Aeronautics and Astronautics, Denver, Colorado, 2017) p. 20.

[19] G. Cinar, D. N. Mavris, M. Emeneth, A. Schneegans, C. Riediger, Y. Fefermann, and A. Isikveren, *Sizing, Integration and Performance Evaluation of Hybrid Electric Propulsion Subsystem Architectures,* in *55th AIAA Aerospace Sciences Meeting*, January (American Institute of Aeronautics and Astronautics, Grapevine, Texas, 2017) p. 21.

[20] J. Zamboni, *A Method for the Conceptual Design of Hybrid Electric Aircraft*, Tech. Rep. (TU Delft, Delft, 2018).

[21] X. Zhang, C. L. Bowman, T. C. O'Connell, and K. S. Haran, *Large electric machines for aircraft electric propulsion,* IET Electric Power Applications **12**, 767 (2018).

[22] J. L. Freeman and B. Schiltgen, *ECO-150-300 Design and Performance: A Tube-and-Wing Distributed Electric Propulsion Airliner,* in *AIAA Scitech 2019 Forum*, January (American Institute of Aeronautics and Astronautics, San Diego, California, 2019) p. 15.

[23] P. Wheeler, *Technology for the More and All Electric Aircraft of the Future,* in *2016 IEEE International Conference on Automatica (ICA-ACCA)* (Institute of Electrical and Electronics Engineers, Curico, 2016) p. 5.

[24] J. Felder, H. Kim, and G. Brown, *Turboelectric Distributed Propulsion Engine Cycle Analysis for Hybrid-Wing-Body Aircraft,* in *47th AIAA Aerospace Sciences Meeting including The New Horizons Forum and Aerospace Exposition*, January (American Institute of Aeronautics and Astronautics 092407, Orlando, Florida, 2009) p. 25.

[25] R. de Vries, M. T. Brown, and R. Vos, *A Preliminary Sizing Method for Hybrid-Electric Aircraft Including Aero-Propulsive Interaction Effects,* in *2018 Aviation Technology, Integration, and Operations Conference* (American Institute of Aeronautics and Astronautics, Atlanta, Georgia, 2018) p. 29.

[26] *Commercial Aircraft Propulsion and Energy Systems Research: Reducing Global Carbon Emissions.* (The National Academies Press, Washington, DC, 2016).

[27] L. Lorenz, A. Seitz, H. Kuhn, and A. Sizmann, *HYBRID POWER TRAINS FOR FUTURE MOBILITY,* in *Deutscher Luft- und Raumfahrtkongress 2013* (Deutsche Gesellschaft für Luft- und Raumfahrt, Stuttgart, 2013) p. 17.

[28] A. T. Isikveren, C. Pornet, P. C. Vratny, and M. Schmidt, *Conceptual Studies of Future Hybrid Electric Regional Aircraft,* in *22nd International Symposium on Air Breathing Engines*, October (American Institute of Aeronautics and Astronautics, Phoenix, Arizona, 2015) p. 20.

[29] A. T. Isikveren, S. Kaiser, C. Pornet, and P. Vratny, *Pre-design strategies and sizing techniques for dual-energy aircraft,* Aircraft Engineering and Aerospace Technology **86**, 525 (2014).

[30] C. T. Brooks and S. Salgueiro, *Design Space Investigation for a Small Electric General Aviation Airplane,* in *55th AIAA Aerospace Sciences Meeting, AIAA SciTech Forum*, January (American Institute of Aeronautics and Astronautics, Grapevine, Texas, 2017) p. 14.

[31] G. Zubi, R. Dufo-López, M. Carvalho, and G. Pasaoglu, *The lithium-ion battery: State of the art and future perspectives,* Renewable and Sustainable Energy Reviews **89**, 292 (2018).

[32] S. Stückl, J. van Toor, and H. Lobentanzer, *VOLTAIR - THE ALL ELECTRIC PROPULSION CONCEPT PLATFORM – A VISION FOR ATMOSPHERIC FRIENDLY FLIGHT,* in *28TH INTERNATIONAL CONGRESS OF THE AERONAUTICAL SCIENCEs* (Brisbane, 2012) p. 11.

[33] Air BP, *Handbook of Products Air BP HANDBOOK OF PRODUCTS,* (2000).

[34] X. Luo, J. Wang, M. Dooner, and J. Clarke, *Overview of current development in electrical energy storage technologies and the application potential in power system operation,* Applied Energy **137**, 511 (2015).

[35] O. Schmitz and M. Hornung, *Methods for simulation and analysis of hybrid electric propulsion systems,* CEAS Aeronautical Journal **6**, 245 (2015).

[36] J. Y. Hung and L. F. Gonzalez, *On parallel hybrid-electric propulsion system for unmanned aerial vehicles,* Progress in Aerospace Sciences **51**, 1 (2012).

[37] C. C. Chan, A. Bouscayrol, and K. Chen, *Electric, hybrid, and fuel-cell vehicles: Architectures and modeling,* IEEE Transactions on Vehicular Technology **59**, 589 (2010).

[38] M. K. Bradley and C. K. Droney, *Subsonic Ultra Green Aircraft Research: Phase II – Volume II – Hybrid Electric Design Exploration*, Tech. Rep. (Boeing Research and Technology, Huntington Beach, California, 2015).

[39] P. W. Douglas, *Cruise Speed Sensitivity Study for Transonic Truss Braced,* in *55th AIAA Aerospace Sciences Meeting, AIAA SciTech Forum*, January (American Institute of Aeronautics and Astronautics, Grapevine, Texas, 2017) p. 11.

[40] J. L. Felder, *Overview of Electrified Aircraft Propulsion at NASA,* (2019).

[41] M. Severson, *Liquid cooled system for aircraft power electroncis cooling,* in *2017 16th IEEE Intersociety Conference on Thermal and Thermomechanical Phenomena in Electronic Systems* (IEEE, Orlando, Florida, 2017) p. 6.

[42] R. Annapragada, A. Sur, R. Mahmoudi, M. Macdonald, and C. E. Lents, *Hybrid Electric Aircraft Battery Heat Acquisition System,* in *2018 AIAA/IEEE Electric Aircraft Technologies Symposium* (American Institute of Aeronautics and Astronautics, Cincinnati, Ohio, 2018) pp. 1–13.

[43] J. Rheaume and C. E. Lents, *Design and Simulation of a Commercial Hybrid Electric Aircraft Thermal Management System,* in *2018 AIAA/IEEE Electric Aircraft Technologies Symposium* (American Institute of Aeronautics and Astronautics, Cincinnati, Ohio, 2018) pp. 1–9.

[44] J. Kim, K. Kwon, S. Roy, E. Garcia, and D. N. Mavris, *Megawatt-class Turboelectric Distributed Propulsion, Power, and Thermal Systems for Aircraft,* in *2018 AIAA Aerospace Sciences Meeting*, January (American Institute of Aeronautics and Astronautics, Kissimmee, Florida, 2018) pp. 1–23.

[45] N. Morioka, H. Oyori, N. Seki, T. Fukuda, and F. Suzuki, *Thermal Management System for the MEE and Engine Embedded Electric Machine,* in *ASME Turbo Expo 2018: Turbomachinery Technical Conference and Exposition* (ASME, Oslo, Norway, 2018) pp. 1–7.

[46] A. A. Pesaran, *Battery thermal models for hybrid vehicle simulations,* Journal of Power Sources **110**, 377 (2002).

[47] Y. Deng, C. Feng, J. E, H. Zhu, J. Chen, M. Wen, and H. Yin, *Effects of different coolants and cooling strategies on the cooling performance of the power lithium ion battery system: A review,* Applied Thermal Engineering **142**, 10 (2018).

[48] J. Huang, S. Shoai Naini, R. Miller, D. Rizzo, K. Sebeck, S. Shurin, and J. Wagner, *A Hybrid Electric Vehicle Motor Cooling System-Design, Model, and Control,* IEEE Transactions on Vehicular Technology **68**, 4467 (2019).

[49] M. Merzvinskas, C. Bringhenti, J. T. Tomita, and C. R. De Andrade, *Air conditioning systems for aeronautical applications: A review,* Aeronautical Journal **124**, 499 (2020).

[50] H. Liu, Z. Wei, W. He, and J. Zhao, *Thermal issues about Li-ion batteries and recent progress in battery thermal management systems: A review,* Energy Conversion and Management **150**, 304 (2017).

[51] T. Wang, K. J. Tseng, J. Zhao, and Z. Wei, *Thermal investigation of lithium-ion battery module with different cell arrangement structures and forced air-cooling strategies,* Applied Energy **134**, 229 (2014).

[52] J. P. Holman, *Heat Transer*, 10th ed. (McGraw-Hill Companies, Inc., New York, 2010) p. 758.

[53] A. Cavallini, A. Mannini, P. Asinari, and C. Zilio, *Carbon Dioxide as a Working Fluid in Aircraft Air – Conditioning: an Experimental Assessment,* in *Proc IIR Conference 2005* (Vicenza, 2005) p. 9.

[54] I. Pérez-Grande and T. J. Leo, *Optimization of a commercial aircraft environmental control system,* Applied Thermal Engineering **22**, 1885 (2002).

[55] R. Kabir, K. Kaddoura, F. McCluckey, and J. Kizito, *Investigation of a Cooling System for A Hybrid Airplane,* in *2018 AIAA/IEEE Electric Aircraft Technologies Symposium* (American Institute of Aeronautics and Astronautics, Cincinnati, Ohio, 2018) p. 18.

[56] Z. Hongli, H. Yu, and C. Liang, *Experimental study on a small Brayton air refrigerator under -120 °C,* Applied Thermal Engineering **29**, 1702 (2009).

[57] N. Morioka and H. Oyori, *All Electric System Architecture for Aircraft and Propulsion,* in *52nd Aerospace Sciences Meeting*, January (American Institute of Aeronautics and Astronautics, National Harbor, Maryland, 2014) pp. 1–7.

[58] M. J. Bracey, *Dynamic Modeling of Thermal Management System with Exergy Based Optimization*, Tech. Rep. (Wright State University, Dayton, Ohio, 2016).

[59] D.M.N. Milewski, *Effect of Electric Environmental Control System Retrofit on Fuel Burn of a Medium-Range Aircraft*, Tech. Rep. (TU Delft, Delft, 2019).

[60] A. Biglia, L. Comba, E. Fabrizio, P. Gay, A. Mannini, A. Mussinatto, and D. R. Ricauda, *Reversed Brayton cycle for food freezing at very low temperatures : Energy performance and optimisation,* International Journal of Refrigeration **81**, 82 (2017).

[61] D. Chen, J. Jiang, G. H. Kim, C. Yang, and A. Pesaran, *Comparison of different cooling methods for lithium ion battery cells,* Applied Thermal Engineering **94**, 846 (2016).

[62] X. Du, W. Zhang, L. Yang, and Y. Yang, *Thermal and Hydraulic Performance of Water/Glycol Mixture and the Application on Power electronics Cooling,* Environmental and Earth Sciences Research Journal **3**, 1 (2016).

[63] D. C. Deisenroth and M. Ohadi, *Thermal management of high-power density electric motors for electrification of aviation and beyond,* Energies **12**, 1 (2019).

[64] R. Kodesová, M. Vlasáková, M. Fér, D. Teplá, O. Jakšík, P. Neuberger, and R. Adamovsky, *Thermal properties of representative soils of the Czech Republic,* Soil and Water Research **8**, 141 (2013).

[65] A. H. Epstein and S. M. Larity, *Considerations for Reducing Aviation's CO2 with Aircraft Electric Propulsion,* JOURNAL OF PROPULSION AND POWER **35**, 572 (2019).

[66] M. Croegaert, *Optimizing the Design of Liquid Cooled Avionics System through the Use of Characterized 3D CFD Simulations in a 1D System Simulation,* (2017).

[67] S. S. Borges, C. A. Cezario, and T. T. Kunz, *Design of Water Cooled Electric Motors Using CFD and Thermography Techniques,* in *2008 International Conference on Electrical Machines* (IEEE, Vilamoura, 2008) p. 6.

[68] K. Mccarthy, E. Walters, A. Heltzel, P. C. Krause, and J. Dalton, *Dynamic Thermal Management System Modeling of a More Electric Aircraft,* SAE TECHNICAL PAPER SERIES **November**, 9 (2008).

[69] M. Wolff, *Integrated Thermal/Power/Propulsion/Vehicle Modeling Issues Related to a More Electric Aircraft Architecture,* (2010).

[70] B. T. Schiltgen and J. Freeman, *Aeropropulsive Interaction and Thermal System Integration within the ECO-150: A Turboelectric Distributed Propulsion Airliner with Conventional Electric Machines,* in *16th AIAA Aviation Technology, Integration, and Operations Conference*, June (American Institute of Aeronautics and Astronautics, Washington, D.C., 2016) pp. 1–18.

[71] L. Byrd, A. Cole, S. Emo, J. Ervin, T. E. Michalak, and V. Tsao, *In-situ Charge Determination for Vapor Cycle Systems in Aircraft,* (2012).

[72] I. Moir and A. Seabridge, *Aircraft Systems*, 3rd ed. ((John Wiley & Sons, 2008) p. 550.

[73] A. Puntel, S. Emo, T. E. Michalak, J. Ervin, L. Byrd, V. Tsao, and T. Reitz, *Refrigerant Charge Management and Control for Next-Generation Aircraft Vapor Compression Systems,* (2013).

[74] J. Mcgovern, *Applied Energy Systems - Rudimentary Thermodynamics* (Dublin Institute of Technology, Dublin, 2014) p. 262.

[75] M. A. Susner and T. J. Haugan, *A Review of the State-of-the-Art Superconductor Technology for High Power Applications,* in *2018 AIAA/IEEE Electric Aircraft Technologies Symposium* (2018) p. 17.

[76] L. R, *Journal of English and Education*, Tech. Rep. 2 (2016).

[77] L. Lusuardi and A. Cavallini, *The Problem of Altitude When Qualifying the Insulating System of Actuators for More Electrical Aircraft,* in *2018 IEEE International Conference on Electrical Systems for Aircraft, Railway, Ship Propulsion and Road Vehicles & International Transportation Electrification Conference (ESARS-ITEC)* (IEEE, Nottingham, 2018) p. 4.

[78] J. P. Cambronne, *Pressure and Temperature effects on the Paschen curve,* in *2011 Annual Report Conference on Electrical Insulation and Dielectric Phenomena* (IEEE, Cancun, 2011) pp. 464–467.

[79] B. J. Brelje and J. R. R. A. Martins, *Electric , hybrid , and turboelectric fixed-wing aircraft : A review of concepts , models , and design approaches,* Progress in Aerospace Sciences **104**, 1 (2019).

[80] T. P. Dever, K. P. Duffy, A. J. Provenza, P. L. Loyselle, B. B. Choi, C. R. Morrison, and A. M. Lowe, *Assessment of Technologies for Noncryogenic Hybrid Electric Propulsion*, Tech. Rep. (NASA, Cleveland, Ohio, 2015).

[81] S. Stückl, *Methods for the Design and Evaluation of Future Aircraft Concepts Utilizing Electric Propulsion Systems*, Ph.D. thesis, Technische Universität München (2016).

[82] M. P. Oomen, *AC LOSS IN SUPERCONDUCTING TAPES AND CABLES*, Ph.D. thesis, University of Twente (2000).

[83] Y. Zhang, W. Liu, X. Zhu, H. Zhao, Z. Hu, C. He, and H. H. Wen, *Unprecedented high irreversibility line in the nontoxic cuprate superconductor (Cu,C)Ba2Ca3Cu4O11+δ ,* Science Advances **4**, 1 (2018).

[84] Z. Wang, J. Qiu, S. Wang, W. Gong, H. Hong, and B. Tian, *Design of cold dielectric HTS power cable,* in *2009 International Conference on Applied Superconductivity and Electromagnetic Devices* (IEEE, Chengdu, 2009) pp. 64–67.

[85] R. Schiferl, C. W. Pkwy, R. Heights, A. Flory, C. Drive, S. D. Umans, C. W. Pkwy, R. Heights, and W. C. Livoti, *HIGH TEMPERATURE SUPERCONDUCTING SYNCHRONOUS MOTORS: ECONOMIC ISSUES FOR INDUSTRIAL APPLICATIONS,* in *IEEE Industry Applications Society 53rd Annual Petroleum and Chemical Industry Conference* (IEEE, Philadelphia, Pennsylvania, 2006) pp. 1–9.

[86] F. Schmidt and A. Allais, *Superconducting cables for power transmission applications - a review,* in *Workshop on Accelerator Magnet Superconductors* (CERN, Hanover, 2004) p. 352.

[87] Nexans, *High Temperature Superconducting Cable for Power Transmission Applications,* (2004).

[88] J. Yuan, J. Maguire, D. Folts, N. Henderson, D. Knoll, M. Gouge, R. Duckworth, J. Demko, and Z. Wolff, *Development and Demonstration of a Fault Current Limiting HTS Cable to be Installed in the Con Edison Grid,* IEEE Transactions on Applied Superconductivity **19**, 1740 (2009).

[89] J. Palmer and E. Shehab, *Modelling of cryogenic cooling system design concepts for superconducting aircraft propulsion,* IET Electrical Systems in Transportation **6**, 170 (2016).

[90] J. L. Felder, G. V. Brown, H. D. Kim, and J. Chu, *Turboelectric Distributed Propulsion in a Hybrid Wing Body Aircraft,* in *20th International Society for Airbreathing Engines (ISABE 2011); September 12, 2011 - September 16, 2011; Gothenburg; Sweden* (NASA, Gothenburg, 2011) p. 20.

[91] R. W. Dyson, *Novel Thermal Energy Conversion Technologies for Advanced Electric Air Vehicles,* in *2018 AIAA/IEEE Electric Aircraft Technologies Symposium* (NASA Glenn Research Center, Cincinnati, Ohio, 2018) p. 14.

[92] G. Meyer, *Advanced Microsystems for Automotive Applications 2012* (Springer, Berlin, 2012) p. 366.

[93] G. Cinar, D. N. Mavris, M. Emeneth, A. Schneegans, and Y. Fefermann, *Development of Parametric Power Generation and Distribution Subsystem Models at the Conceptual Aircraft Design Stage,* in *55th AIAA Aerospace Sciences Meeting*, January (American Institute of Aeronautics and Astronautics, Grapevine, Texas, 2017) p. 18.

[94] W. M. Seong, K. Y. Park, M. H. Lee, S. Moon, K. Oh, H. Park, S. Lee, and K. Kang, *Abnormal self-discharge in lithium-ion batteries,* Energy and Environmental Science **11**, 970 (2018).

[95] R. Chen, R. Luo, Y. Huang, F. Wu, and L. Li, *Advanced High Energy Density Secondary Batteries with Multi-Electron Reaction Materials,* Advanced Science **3**, 1 (2016).

[96] A. Grenier, *Development of solid-state Fluoride-ion Batteries: cell design, electrolyte characterization and electrochemical mechanisms*, Tech. Rep. (Université Pierre et Marie Curie, Paris, France, 2016).

[97] M. M. Thackeray, C. Wolverton, and E. D. Isaacs, *Electrical energy storage for transportation - Approaching the limits of, and going beyond, lithium-ion batteries,* Energy and Environmental Science **5**, 7854 (2012).

[98] J. McGrory, M. Rosen, M. Fowler, M. Malik, M. Mathew, and I. Dincer, *Experimental investigation and thermal modelling of a series connected LiFePO 4 battery pack,* International Journal of Thermal Sciences **132**, 466 (2018).

[99] P. Ramadass, B. Haran, R. White, and B. N. Popov, *Capacity fade of Sony 18650 cells cycled at elevated temperatures,* Journal of Power Sources **112**, 606 (2002).

[100] M. Parhizi, M. B. Ahmed, and A. Jain, *Determination of the core temperature of a Li-ion cell during thermal runaway,* Journal of Power Sources **370**, 27 (2017).

[101] P. G. Balakrishnan, R. Ramesh, and T. Prem Kumar, *Safety mechanisms in lithium-ion batteries,* Journal of Power Sources **155**, 401 (2006).

[102] D. H. Jeon and S. M. Baek, *Thermal modeling of cylindrical lithium ion battery during discharge cycle,* Energy Conversion and Management **52**, 2973 (2011).

[103] A. Senyshyn, M. J. Mühlbauer, O. Dolotko, and H. Ehrenberg, *Low-temperature performance of Li-ion batteries: The behavior of lithiated graphite,* Journal of Power Sources **282**, 235 (2015).

[104] X. Fan, W. Sun, F. Meng, A. Xing, and J. Liu, *Advanced chemical strategies for lithium–sulfur batteries: A review,* Green Energy and Environment **3**, 2 (2018).

[105] Y. Yang, G. Zheng, and Y. Cui, *Nanostructured sulfur cathodes,* Chemical Society Reviews **42**, 3018 (2013).

[106] J. Zhu, P. Zhu, C. Yan, X. Dong, and X. Zhang, *Recent progress in polymer materials for advanced lithium-sulfur batteries,* Progress in Polymer Science **90**, 118 (2019).

[107] S. Gerssen-Gondelach and A. P. C. Faaij, *Performance of batteries for electric vehicles on short and longer term,* Journal of Power Sources **212**, 111 (2012).

[108] Z. Ma, X. Yuan, L. Li, Z. F. Ma, D. P. Wilkinson, L. Zhang, and J. Zhang, *A review of cathode materials and structures for rechargeable lithium-air batteries,* Energy and Environmental Science **8**, 2144 (2015).

[109] A. Manthiram, Y. Fu, and Y. S. Su, *Challenges and prospects of lithium-sulfur batteries,* Accounts of Chemical Research **46**, 1125 (2013).

[110] F. Chen, Z. Jiao, B. Zhao, Z. Chen, Y. Jiang, S. Wang, Y. Gao, Q. Gao, and Y. Wang, *Inhibiting the shuttle effect of Li–S battery with a graphene oxide coating separator: Performance improvement and mechanism study,* Journal of Power Sources **342**, 929 (2017).

[111] F. Wu and Y. Yu, *Toward True Lithium-Air Batteries,* Joule **2**, 815 (2018).

[112] U. R. Farooqui, A. L. Ahmad, and N. A. Hamid, *Challenges and potential advantages of membranes in lithium air batteries: A review,* Renewable and Sustainable Energy Reviews **77**, 1114 (2017).

[113] K. G. Gallagher, S. Goebel, T. Greszler, M. Mathias, W. Oelerich, D. Eroglu, and V. Srinivasan, *Quantifying the promise of lithium-air batteries for electric vehicles,* Energy and Environmental Science **7**, 1555 (2014).

[114] K. X. Wang, Q. C. Zhu, and J. S. Chen, *Strategies toward High-Performance Cathode Materials for Lithium–Oxygen Batteries,* Small **14**, 1 (2018).

[115] G. Girishkumar, B. McCloskey, A. C. Luntz, S. Swanson, and W. Wilcke, *Lithium-air battery: Promise and challenges,* Journal of Physical Chemistry Letters **1**, 2193 (2010), arXiv:_cambardella Formation and Decomposition .

[116] T. Yu, J. Fu, R. Cai, A. Yu, and Z. Chen, *Nonprecious Electrocatalysts for Li-Air and Zn-Air Batteries: Fundamentals and recent advances.* IEEE Nanotechnology Magazine **11**, 29 (2017).

[117] A. Rahman, X. Wang, and C. Wen, *A review of high energy density lithium-air battery technology,* Journal of Applied Electrochemistry **44**, 5 (2014).

[118] L. Wang, J. Pan, Y. Zhang, X. Cheng, L. Liu, and H. Peng, *A Li-Air Battery with Ultralong Cycle Life in Ambient Air,* Advanced Materials **30**, 1 (2017).

[119] K. Yoo, S. Banerjee, and P. Dutta, *Modeling of volume change phenomena in a Li-air battery,* Journal of Power Sources **258**, 340 (2014).

[120] J. P. Zheng, R. Y. Liang, M. Hendrickson, and E. J. Plichta, *Theoretical Energy Density of Li–Air Batteries,* Journal of The Electrochemical Society **155**, A432 (2008).

[121] J. O. Park, M. Kim, J. H. Kim, K. H. Choi, H. C. Lee, W. Choi, S. B. Ma, and D. Im, *A 1000 Wh kg-1 Li–Air battery: Cell design and performance,* Journal of Power Sources **419**, 112 (2019).

[122] H. C. Lee, J. O. Park, M. Kim, H. J. Kwon, J. H. Kim, K. H. Choi, K. Kim, and D. Im, *High-Energy-Density Li-O2 Battery at Cell Scale with Folded Cell Structure,* Joule **3**, 1 (2018).

[123] M. Asadi, B. Sayahpour, P. Abbasi, A. T. Ngo, K. Karis, J. R. Jokisaari, C. Liu, B. Narayanan, M. Gerard, P. Yasaei, X. Hu, A. Mukherjee, K. C. Lau, R. S. Assary, F. Khalili-Araghi, R. F. Klie, L. A. Curtiss, and A. Salehi-Khojin, *A lithium-oxygen battery with a long cycle life in an air-like atmosphere,* Nature **555**, 502 (2018).

[124] C. Pornet, *Electric Drives for Propulsion System of Transport Aircraft,* in *New Applications of Electric Drives*, December, edited by C. Miroslav (InTech, 2015) Chap. 5.

[125] V. K. Davis, C. M. Bates, K. Omichi, B. M. Savoie, N. Momčilović, Q. Xu, W. J. Wolf, M. A. Webb, K. J. Billings, N. H. Chou, S. Alayoglu, R. K. McKenney, I. M. Darolles, N. G. Nair, A. Hightower, D. Rosenberg, M. Ahmed, C. J. Brooks, T. F. Miller, R. H. Grubbs, and S. C. Jones, *Room-temperature cycling of metal fluoride electrodes: Liquid electrolytes for high-energy fluoride ion cells,* Science **362**, 1144 (2018).

[126] C. Rongeat, M. A. Reddy, R. Witter, and M. Fichtner, *Nanostructured fluorite-type fluorides as electrolytes for fluoride ion batteries,* Journal of Physical Chemistry C **117**, 4943 (2013).

[127] A. Gross, D. Sandbeck, M. Weil, N. Hörmann, M. Fichtner, G. Rodriguez-Garcia, and F. Gschwind, *Fluoride ion batteries: Theoretical performance, safety, toxicity, and a combinatorial screening of new electrodes,* Journal of Fluorine Chemistry **182**, 76 (2016).

[128] S. Walus, T. Cleaver, A. Fotouhi, L. O'Neill, and D. Auger, *Lithium-Sulfur Battery Technology Readiness and Applications—A Review,* Energies **10**, 15 (2017).

[129] P. G. Bruce, S. A. Freunberger, L. J. Hardwick, and J. M. Tarascon, *Li-O2 and Li-S batteries with high energy storage,* Nature Materials **11**, 19 (2012), arXiv:_cambardella Formation and Decomposition .

[130] A. Seitz, O. Schmitz, C. Pornet, C. Gologan, A. T. Isikveren, M. Hornung, and P. C. Vratny, *Methodology for Sizing and Performance Assessment of Hybrid Energy Aircraft,* Journal of Aircraft **52**, 341 (2015).

[131] G. E. Blomgren, *The Development and Future of Lithium Ion Batteries,* Journal of The Electrochemical Society **164**, A5019 (2016).

[132] B. Scrosati, J. Hassoun, and Y. K. Sun, *Lithium-ion batteries. A look into the future,* Energy and Environmental Science **4**, 3287 (2011).

[133] R. de Vries, M. F. M. Hoogreef, and R. Vos, *Aeropropulsive Efficiency Requirements for Turboelectric Transport Aircraft,* in *Aeropropulsive Efficiency Requirements for Turboelectric Transport Aircraft* (American Institute of Aeronautics and Astronautics, Orlando, Florida, 2020) p. 16.

[134] G. V. Brown, A. F. Kascak, B. Ebihara, D. Johnson, B. B. Choi, M. Siebert, and C. Buccieri, *NASA Glenn Research Center Program in High Power Density Motors for Aeropropulsion*, Tech. Rep. December (NASA, Cleveland, Ohio Albert, 2005).

[135] N. E. Anderson, S. H. Loewenthal, and J. D. Black, *An Analytical Method To Predict Efficiency of Aircraft Gearboxes,* Journal of Mechanisms, Transmissions, and Automation in Design **108**, 424 (1986).

[136] M. C. Cameretti, A. Del Pizzo, L. P. Di Noia, M. Ferrara, and C. Pascarella, *Modeling and investigation of a turboprop hybrid electric propulsion system,* Aerospace **5** (2018), 10.3390/aerospace5040123.

[137] S. J. Rind, Y. Ren, Y. Hu, J. Wang, and L. Jiang, *Configurations and Control of Traction Motors for Electric Vehicles : A Review,* **3**, 13 (2017).

[138] J. Larminie and J. Lowry, *Electric Vehicle Technology Explained* (John Wiley & Sons Ltd, Chichester, 2003) arXiv:arXiv:1011.1669v3 .

[139] R. A. McDonald, *Electric propulsion modeling for conceptual aircraft design,* in *52nd Aerospace Sciences Meeting*, January (American Institute of Aeronautics and Astronautics, National Harbor, Maryland, 2014) p. 19.

[140] D. Trawick, K. Milios, J. C. Gladin, and D. N. Mavris, *A Method for Determining Optimal Power Management Schedules for Hybrid Electric Airplanes,* in *AIAA Propulsion and Energy 2019 Forum*, August (AIAA, Indianapolis, 2019) p. 21.

[141] T. S. Bryden, B. Dimitrov, G. Hilton, C. Ponce de León, P. Bugryniec, S. Brown, D. Cumming, and A. Cruden, *Methodology to determine the heat capacity of lithium-ion cells,* Journal of Power Sources **395**, 369 (2018).

[142] O. Tremblay and L. A. Dessaint, *Experimental validation of a battery dynamic model for EV applications,* World Electric Vehicle Journal **3**, 289 (2009).

[143] M. Skyllas-Kazacos, C. Menictas, and T. Lim, *Electricity Transmission, Distribution and Storage Systems* (Woodhead Publishing Limited, 2013) pp. 398–441.

[144] W. Tahil, *How Much Lithium does a LiIon EV battery really need ?* (2010).

[145] G. J. Rao and S. K. Shrivastava, *Modeling of Hybrid Solar - Wind Renewable Energy Systems with Battery Storage,* INTERNATIONAL JOURNAL OF INNOVATIVE RESEARCH IN ELECTRICAL, ELECTRONICS, INSTRUMENTATION AND CONTROL ENGINEERING **3**, 204 (2015).

[146] M. M. A., M. T. Iqbal, K. Pope, and L. Rolland, *Dynamic modeling and simulation of the MUN Explorer autonomous underwater vehicle with a fuel cell system,* AIMS Electronics and Electrical Engineering **4**, 114 (2020).

[147] M. L. M. Tasuni, Z. A. Latiff, H. Nasution, M. M. Perang, H. M. Jamil, and M. N. Misseri, *Performance of a water pump in an automotive engine cooling system,* Jurnal Teknologi **78**, 47 (2016).

[148] ITT, *Goulds Pumps - Technical Data - Residential Water Systems,* (2008).

[149] N. Chaurasia and S. P. Rajput, *Optimization of friction factor for aerospace duct of equipment cooling system of aircraft,* International Journal of Mechanical Engineering and Technology **10**, 1162 (2019).

[150] B. Zohuri, *Compact heat exchangers*, January (2017) p. 570.

[151] J. E. Hesselgreaves, R. Law, and D. A. Reay, *Thermal Design,* in *Compact Heat Exchangers* (Elsevier Ltd., 2017) 2nd ed., pp. 275–360.

[152] J. E. Hesselgreaves, R. Law, and D. A. Reay, *Surface Comparisons, Size, Shape and Weight Relationships,* in *Compact Heat Exchangers* (Elsevier Ltd., 2017) 2nd ed., pp. 129–155.

[153] P. Gullberg, R. Sengupta, and K. Horrigan, *Transient fan modelling and effects of blade deformation in a truck cooling fan installation,* in *Institution of Mechanical Engineers - VTMS 2011, Vehicle Thermal Management Systems Conference Proceedings* (Woodhead Publishing Limited, 2013) pp. 219–227.

[154] I. Chakraborty, D. Trawick, D. N. Mavris, M. Emeneth, and A. Schneegans, *A requirements-driven methodology for integrating subsystem architecture sizing and analysis into the conceptual aircraft design phase,* in *AIAA AVIATION 2014 -14th AIAA Aviation Technology, Integration, and Operations Conference*, June (American Institute of Aeronautics and Astronautics, Atlanta, GA, 2014) p. 24.

[155] S. W. Spence, W. J. Doran, and D. W. Artt, *Design, construction and testing of an air-cycle refrigeration system for road transport,* International Journal of Refrigeration **27**, 503 (2004).

[156] ATR, *ATR Family,* (2014).

[157] P. D. Vecchia, *Development of Methodologies for the Aerodynamic Design and Optimization of New Regional Turboprop Aircraft*, Ph.D. thesis, University of Naples Federico II (2013).

[158] R. H. Jansen, C. Bowman, A. Jankovsky, R. Dyson, and J. Felder, *Overview of NASA electrified aircraft propulsion research for large subsonic transports,* in *53rd AIAA/SAE/ASEE Joint Propulsion Conference, 2017* (2017) pp. 1–20.

[159] A. T. Isikveren, A. Seitz, P. C. Vratny, C. Pornet, K. Plötner, and M. Hornung, *Conceptual studies of universally-electric systems architectures suitable for transport aircraft,* in *Deutscher Luft- und Raumfahrtkongress 2012*, June 2016 (Bauhaus Luftfahrt, Berlin, 2012) p. 16.

[160] P. Stephan, S. Kabelac, M. Kind, H. Martin, D. Mewes, and K. Schaber, *VDI Heat Atlas*, 2nd ed., edited by V.-G. V. und Chemieingenieurwesen (Springer, Düsseldorf, 2010) pp. 1226–1239.

[161] A. Kolli, A. Gaillard, A. De Bernardinis, O. Bethoux, D. Hissel, and Z. Khatir, *A review on DC/DC converter architectures for power fuel cell applications,* Energy Conversion and Management **105**, 716 (2015).

[162] C. Lents, L. Hardin, J. Rheaume, and L. Kohlman, *Parallel hybrid gas-electric geared turbofan engine conceptual design and benefits analysis,* 52nd AIAA/SAE/ASEE Joint Propulsion Conference, 2016 , 1 (2016).

[163] K. Seeckt, D. Scholz, and B. Tor, *Application of the Aircraft Preliminary Sizing Tool Presto To Kerosene and Liquid Hydrogen Fueled Regional Freighter Aircraft,* (2010).

[164] BorgWarner, *Performance Turbochargers - 2017 catalog,* (2016).

[165] MaxQ, *Liquid Cooled Coldplate - 007-MXQ-01,* .

[166] A. S. Novikov, A. G. Paikin, V. L. Dorofeyev, V. M. Ananiev, and A. L. Kapelevich, *Application of gears with asymmetric teeth in turboprop engine gearbox,* in *International Design Engineering Technical Conferences and Computers and Information in Engineering Conference*, Vol. 48086 (ASME, Las Vegas, 2007) pp. 327–334.

[167] A. Plesca, *Thermal analysis of busbars from a high current power supply system,* Energies **12**, 15 (2019).

[168] Legrand, *Solutions for the electrical distribution,* (2016).

[169] Mersen, *Laminated bus bar solutions,* (2000).

[170] J. K. Mueller, A. Bensmann, B. Bensmann, T. Fischer, T. Kadyk, G. Narjes, F. Kauth, B. Ponick, J. R. Seume, U. Krewer, R. Hanke-Rauschenbach, and A. Mertens, *Design considerations for the electrical power supply of future civil aircraft with active high-lift systems,* Energies **11** (2018), 10.3390/en11010179.

[171] E. Abbasi and V. Garousi, *An MILP-based formulation for minimizing pumping energy costs of oil pipelines: Beneficial to both the environment and pipeline companies,* Energy Systems **1**, 393 (2010).

[172] B. M. Patel, A. J. Modi, and P. P. Rathod, *Analysis of engine cooling waterpump of car & significance of its geometry,* International Journal of Mechanical Engineering and Technology **4**, 100 (2013).

[173] I. Martinez, *Aicraft Environmental Control System*, Tech. Rep.

[174] P. Feliot, Y. L. Guennec, J. Bect, and E. Vazquez, *Design of a commercial aircraft environment control system using Bayesian optimization techniques,* in *EngOpt 2016 - 5th International Conference on Engineering Optimization*, October (Iguassu Falls„ 2016) p. 10, arXiv:1610.02271 .

[175] R. Slingerland, S. Zandstra, D. Scholz, and K. Seeckt, *Green freighter systems,* in *46th AIAA Aerospace Sciences Meeting and Exhibit* (AIAA, 2008) pp. 1–14.

[176] J. Large and A. Pesyridis, *Investigation of micro gas turbine systems for high speed long loiter tactical unmanned air systems,* Aerospace **6**, 1 (2019).

A

EMPIRICAL REGRESSION CURVES

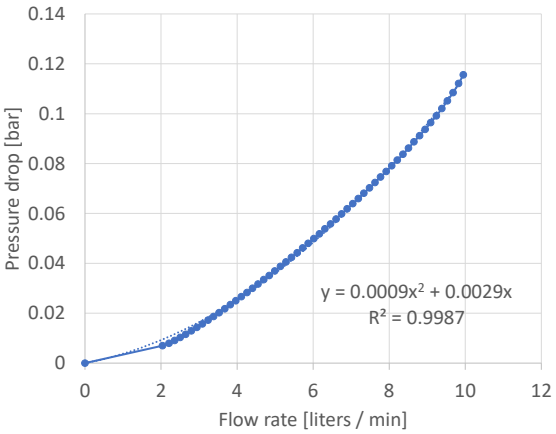

Figure A.1: Cold plate regression curve to estimate pressure drop [1].

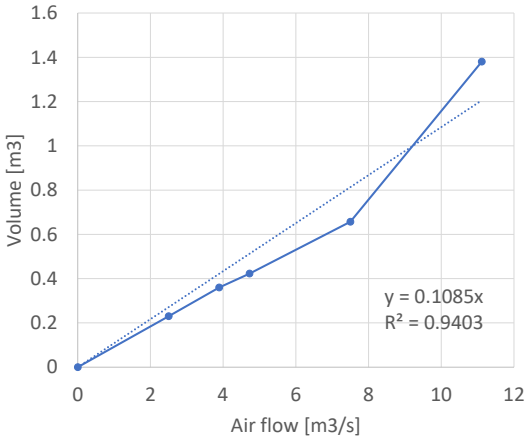

Figure A.2: Fan regression curve to estimate volume.
Models used: HD710/2xD5, HD560/D5, HD500/D2.5, HE560/D2.5, and HE500/D2 [2]

[1] MaxQ. 007-MXQ-01. URL: https://maxqtechnology.com/wp-content/uploads/2019/01/007-MXQ-01-new1-1.9.19.pdf. Accessed on: 26/05/2020

[2] Fischbach. High efficiency fans. URL: https://www.fischbach-luft.de/en/centrifugal-fans/high-efficiency-fans/. Accessed on: 26/05/2020

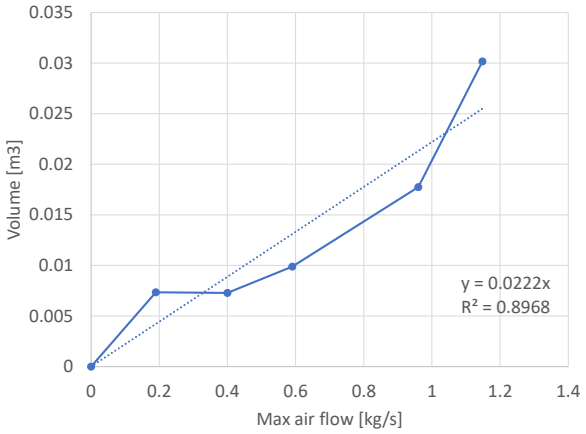

(a) ACM regression curve to estimate volume.
Models used: S1BG, S200SX, S300SX3, S400SX, and S500X [164].

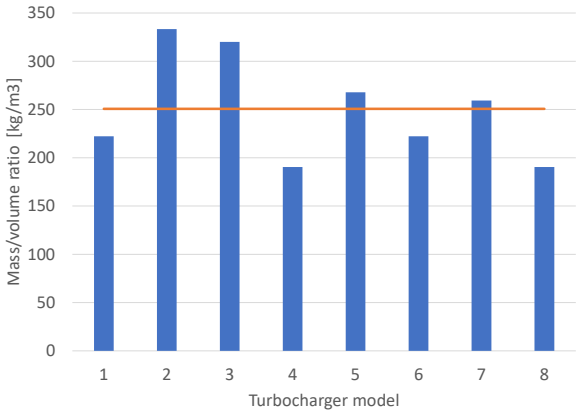

(b) ACM empirical data to estimate weight.
Models used: Turbocharger 452058-5002S, Turbocharger 465288-5004S, Turbocharger 49173-07508, Turbocharger 5333-988-6709, Turbocharger 5327-988-6534-R, Turbocharger 711017-5004S, Turbocharger 712541-5007S, and Turbocharger 769040-5001S [3].

Figure A.3: ACM volume and weight estimation [3] [164].

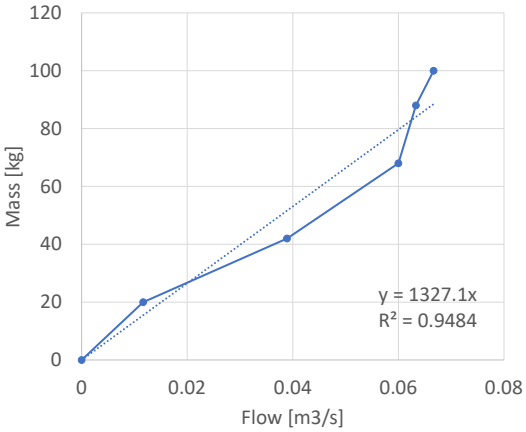

(a) Pump regression curve to estimate weight.
Models used: 40-160/4, 65-160/15, 80-200/22, 80-250/45, and 80-250/55.

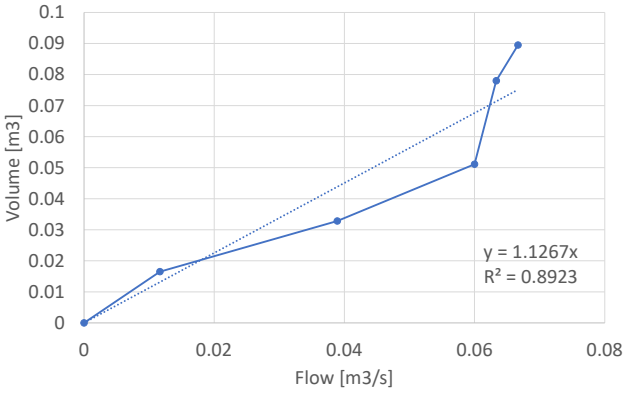

(b) Pump regression curve to estimate volume.
Models used: 40-160/4, 65-160/15, 80-200/22, 80-250/45, and 80-250/55.

Figure A.4: Pump volume and weight estimation [4].

[3] Turbo Direct. Turbocharger. URL: https://turbodirectparts.nl/product-categorie/turbocharger/. Accessed on: 26/05/2020

[4] Ebara. Centrifugal pumps - 3 series F version. URL: https://media.ebaraeurope.com/assets/161222-082631-DataBook_3SERIESFVERSION_50_H_IE2_3.pdf. Accessed on: 26/05/2020

B

REFERENCE CASE STUDY

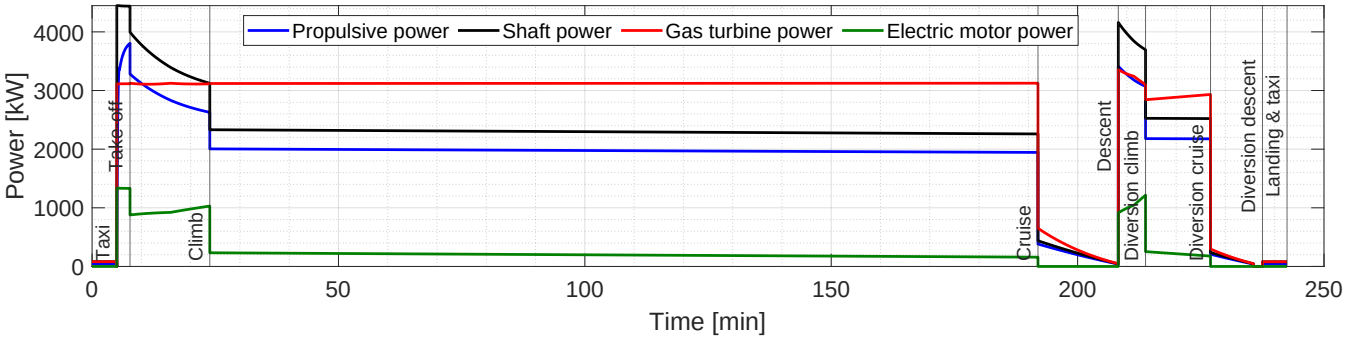

Figure B.1: Power usage during the reference flight mission [20].

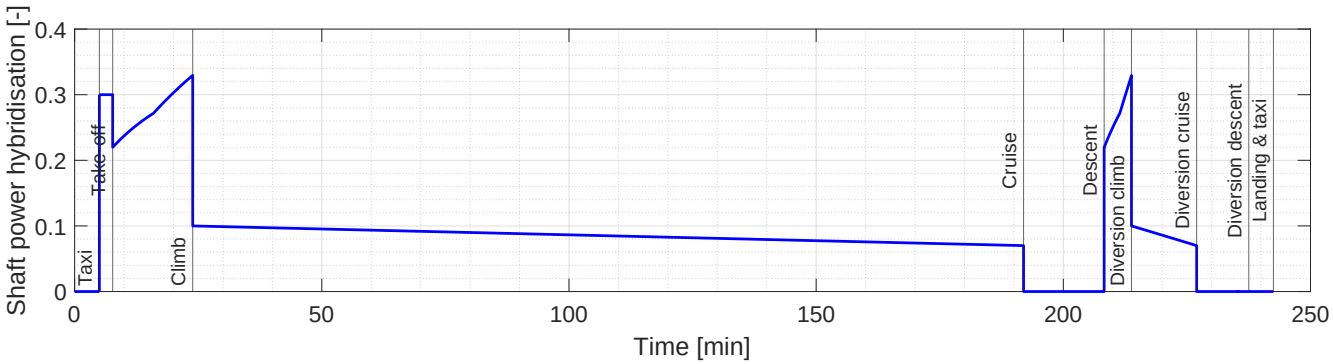

Figure B.2: Hybridisation strategy for the reference flight mission [20].

C

COMPONENT CHARACTERISTICS

Table C.1: Battery pack characteristics used for the near-term and mid-term scenarios, based on [20, 93].

Parameter	Values
Cell capacity [Ah]	3.0
Cell full voltage [V]	4.2
Cell exponential zone charge [Ah]	0.1277
Cell exponential zone voltage [V]	3.889
Cell nominal current [A]	4.0
Cell nominal zone charge [Ah]	2.351
Cell nominal zone voltage [V]	3.6
Cell resistance [Ω]	0.01385
Cell specific heat capacity [J/kg/K]	1200
Cell diameter [mm]	18.0
Cell height [mm]	49.51
Stack factor y-axis	75
Stack factor z-axis	5
Battery pack burden [%]	15

Table C.2: Electric motor parametric model values, set constant for all used for all scenarios, based on [20].

Parameter	$EM_{power\ train}$	$EM_{compressor}$
Rated power [kW]	670	116
ω_{max} [rpm]	40,400	30,000
k_0 [-]	0.5	0.5
k_P [-]	0.8921	0.8921
k_Q [-]	1.3	1.3
k_ω [-]	1.3	1.3

Table C.3: Parameter assumptions for electric, pneumatic, and hydraulic routing elements, set constant for all scenarios [149].

Parameter	Electric routing	Pneumatic routing	Hydraulic routing
Material	Copper	Aluminium	PVC
Inner diameter [mm]	11.68	280	20
Wall thickness [mm]	5	5	5
Resistance [Ω/m]	0.0001706	-	-
Relative roughness [-]	-	0.001	0.01
Density [kg/m] / [kg/m^3] / [kg/m^3]	1.0477	2700	1390

Table C.4: System component constant performance parameters based on provided references.

Component	Parameter	Symbol	Value
Cold plate [165]	Volume single plate [m^3]	$v_{CP,\,single}$	0.0005252
	Specific power [kW/kg]	SP_{CP}	2.50
	Power density [kW/m^3]	$\hat{v}_{CP}$	5712
	Pressure drop constant 1 [bar/(liter/min)]	$k_{CP,1}$	0.0029
	Pressure drop constant 2 [bar/(liter/min)^2]	$k_{CP,2}$	0.0009
Gearbox [1] [20, 166]	Power density [kW/m^3]	$\hat{v}_{GB}$	21901
	Operating temperature [°C]	T_{GB}	60
	Gearbox speed ratio in/out [-]	-	20.78
Electric motor [2]	Operating temperature [°C]	T_{EM}	80
Electric motor controller [3]	Specific power [kW/kg]	SP_{EMC}	9.375
	Power density [kW/m^3]	$\hat{v}_{EMC}$	9563
Electric bus [167–169]	Specific power [kW/kg]	SP_{bus}	158
	Power density [kW/m^3]	$\hat{v}_{bus}$	1420000
	Internal resistance [mΩ]	R_{bus}	0.288
	Operating temperature [°C]	T_{bus}	35
	Weight isolation constant [-]	$k_{isolation}$	2
Electric power converter [161, 170]	Power density [kW/m^3]	$\hat{v}_{PC}$	10000
	Operating temperature [°C]	T_{PC}	90
Hydraulic pump [171, 172]	Specific flow rate [kg/(m^3/s)]	$k_{HP,\,m}$	1327.1
	Flow rate density [m^3/(m^3/s)]	$k_{HP,\,v}$	1.1267
	Maximum efficiency [%]	η_{HP}	83.5
	System pressure target [bar]	p_{system}	1.5
	Impeller diameter [cm]	$D_{HP,\,impeller}$	11.2
Heat exchanger (air/liquid) [150, 152, 173]	Surface compactness [m^2/m^3]	$k_{HEX,\,compactness\ ratio}$	1100
	Heat transfer area [m^2]	$A_{HEX,\,heat}$	30
	Combined material density [kg/m^3]	$\rho_{HEX,\,total}$	300
	Porosity factor [-]	$k_{HEX,\,porosity}$	0.4
	Overall heat transfer coefficient [W/m^2/K]	U_{HEX}	550
	Relative pressure drop, hydraulic [%]	-	1
	Relative pressure drop, pneumatic [%]	-	8
Air cycle system [150, 152, 174, 175]	Surface compactness [m^2/m^3]	$k_{ACS,\,HEX,\,compactness\ ratio}$	1100
	Heat transfer area [m^2]	$A_{ACS,\,HEX,\,heat}$	65
	Combined material density [kg/m^3]	$\rho_{ACS,\,HEX,\,total}$	300
	Porosity factor [-]	$k_{ACS,\,HEX,\,porosity}$	0.4
	Overall heat transfer coefficient [W/m^2/K]	$U_{ACS,\,HEX}$	180
	Relative pressure drop, pneumatic [%]	-	8
	Compressor efficiency [%]	$\eta_{ACS,\,compressor}$	80
	Turbine efficiency [%]	$\eta_{ACS,\,turbine}$	92
	Additional weight scaling factor [-]	k_{ACS}	1.8
	Weight scaling factor [kg/m^3]	$k_{ACS,\,m}$	250
	Volume scaling factor [m^3/(kg/s)]	$k_{ACS,\,v}$	0.0222
Pneumatic compressor [154, 176]	Specific power [kW/kg]	SP_{PCO}	2.5
	Operating temperature [°C]	T_{PCO}	80
	Maximum efficiency [%]	η_{PCO}	81
	Impeller diameter [cm]	$D_{PCO,\,impeller}$	23
Pneumatic fan [4] [5]	Specific power [kW/kg]	SP_{PF}	0.55
	Operating temperature [°C]	T_{PF}	80
	Maximum efficiency [%]	η_{PF}	60
	Impeller diameter [cm]	$D_{PF,\,impeller}$	30
	Volume scaling factor [m^3/(m^3/s)]	$k_{PF,\,v}$	0.1085
Ram air inlet [54, 174]	Entry cross-section [dm^2]	$A_{ram,\,in}$	10
	Efficiency [%]	$\eta_{ram,\,in}$	90
Ram air outlet [54, 174]	Exit cross-section [dm^2]	$A_{ram,\,out}$	4.8
	Efficiency [%]	$\eta_{ram,\,out}$	95

[1] Flight Safety Australia. Robinson telatemps. URL: https://www.flightsafetyaustralia.com/2017/11/stickers-for-accuracy-robinson-telatemps/. Accessed on: 20/09/2020

[2] Plant Engineering. Motor construction. URL: https://www.plantengineering.com/articles/when-it-comes-to-motors-how-hot-is-

hot/. Accessed on: 20/09/2020

[3]UQM. Powerphase HD 250. URL: https://wiki.neweagle.net/ProductDocumentation/EV_Software_and_Hardware/Electric_Motors/UQM/PowerPhase%20HD%20250%20web.pdf. Accessed on: 21/09/2020

[4]Fan Performance Characteristics. Fan Engineering of Centrifugal Fans. URL: https://www.tcf.com/wp-content/uploads/2018/06/Fan-Performance-Characteristics-of-Centrifugal-Fans-FE-2400.pdf. Accessed on: 19/09/2020

[5]United Technologies Research Center - Public data